UNIVERSITY OF OKLAHOMA

GRADUATE COLLEGE

STRUCTURAL AND MUTAGENESIS STUDIES OF THE YEAST PHOSPHORELAY SIGNALING PROTEINS YPD1 AND SSK1

A DISSERTATION

SUBMITTED TO THE GRADUATE FACULTY

in partial fulfillment of the requirements for the

Degree of

DOCTOR OF PHILOSOPHY

By

KATIE MARIE BRANSCUM
Norman, Oklahoma
2015

Downloaded from SHAREOK. Persistent Handle URL: https://hdl.handle.net/11244/23300

STRUCTURAL AND MUTAGENESIS STUDIES OF THE YEAST PHOSPHORELAY SIGNALING PROTEINS YPD1 AND SSK1

A DISSERTATION APPROVED FOR THE
DEPARTMENT OF CHEMISTRY AND BIOCHEMISTRY

BY

_____
Dr. Ann H. West, Chair

_____
Dr. Susan Schroeder

_____
Dr. Wai Tak Yip

_____
Dr. Elena Zgurskaya

_____
Dr. Elizabeth A. Karr

© Copyright by KATIE MARIE BRANSCUM 2015
All Rights Reserved.

Acknowledgements

This dissertation could not have been written without the collaboration and hard work of Dr. Smita Menon, who solved the Ssk1-R2^{W638A}/Ypd1 crystal structure. Dr. Len Thomas of the Macromolecular Crystallography Laboratory, Dr. Susan Nimmo of the NMR facility and Dr. Steven Foster of the Mass Spectrometry Facility at the University of Oklahoma greatly assisted with data collection. Dr. Paul Cook, Dr. Paul Sims, Clay Foster and Dr. Eliza Ruben were consulted for their intellectual input on a range of topics. Dr. Fabiola Janiak-Spens began the initial development of the fluorescence binding assay. Clay Foster, Emily Kennedy, Jamie Sykes, Skyler Hebdon, Krutik Soni, Maryum Shahzad, Sana Fazal, Dr. Jon Henrikson, Dr. Christine Theodore, Dr. Xiarou Wang, Alexandra Gerea and Serena Hageman were involved collaboratively in parts of various projects. Jarrod King and Dr. Jian Lan You performed bioactivity and anti-biofilm assays.

Of course, this dissertation would not exist without the dedicated mentorship of Dr. Ann West and Dr. Robert Cichewicz. I am deeply grateful to every one of these people for their time, effort and contribution to this dissertation. I would also like to thank the members of my committee who have done their best to ensure that my work is an acceptable addition to the greater body of scientific knowledge.

Table of Contents

Acknowledgements iv

Table of Contents v

List of Tables x

List of Figures xi

Abstract xv

CHAPTER 1: INTRODUCTION 1

Two-component signal transduction 1

Multi-step phosphorelay systems 2

Histidine kinase proteins 4

Histidine phosphotransfer proteins 7

Response regulator proteins 8

Phosphotransfer mechanism 11

S. cerevisiae Sln1 phosphorelay pathway 13

Differences between Ypd1 cognate receiver domains: Sln1-R1 and Ssk1-R2 14

Research Focus 19

References 20

CHAPTER 2: CO-CRYSTALLIZATION OF AN SSK1-R2 POINT MUTANT (W638A) IN COMPLEX WITH YPD1 31

Introduction 31

Expression and purification of Ssk1-R2-W638A 31

Co-crystallization of Ypd1 in complex with Ssk1-R2-W638A 32

Co-crystal structure of Ssk1-R2^{W638A}/Ypd1 34

Discussion 35

Experimental Section 36

Construction of mutants *36*

Protein Purification *36*

Crystallization and data collection *37*

Structure determination and refinement *38*

References 40

CHAPTER 3: BIOCHEMICAL CHARACTERIZATION OF SSK1 POINT MUTANTS 42

Introduction 42

Ssk1-R2-W638A retains wild type-like activity 43

Affinity for Ypd1 ..... *43*

Phosphotransfer activity with Ypd1 ..... *46*

Ssk1-R2 active site mutants and phosphotransfer with Ypd1 49

Protein purification *49*

Phosphotransfer activity with Ypd1 ..... *50*

Negative control mutants of Ssk1-R2 54

Protein purification *55*

Binding affinity and phosphotransfer activity with Ypd1 ..... *56*

Abolishment of salt bridge formation affects binding affinity 58

Protein purification *59*

Binding affinity between Ssk1-R2 salt bridge mutants and Ypd1 ..... *60*

Phosphotransfer activity with Ypd1 ..... *62*

Mutations that do not affect Ssk1-R2 activity 62

Discussion 64

Experimental Section 66

Construction of mutants *66*

Transformation *66*

Protein purification *67*

Phosphotransfer experiments *67*

Fluorescence binding affinity *69*

References 71

CHAPTER 4: INSIGHTS GAINED FROM THE CO-CRYSTAL STRUCTURE OF SSK1-R2^{W638A}/YPD1 73

Introduction 73

Comparison of Ssk1-R2^{W638A}/Ypd1 and Sln1-R1/Ypd1 complexes 74

Comparison of Ssk1-R2^{W638A}/Ypd1 and Sln1-R1/Ypd1 interfaces 76

Analysis of Ssk1-R2^{W638A}/Ypd1 and Sln1-R1/Ypd1 active sites 81

Discussion 84

References 86

CHAPTER 5: PLASMID EXPRESSION CONSTRUCTS FOR SSK1 FROM *CRYPTOCOCCUS NEOFORMANS* 88

Introduction 88

CnSsk1 homology modeling 93

CnR2-A *96*

CnR2-B *96*

CnR2-C *98*

CnR2-D *100*

CnR2-E *102*

CnR2-F *104*

CnR2-G *106*

CnR2-H *107*

CnR2-I *108*

CnR2-J *109*

CnR2-K *111*

CnR2-L *112*

CnR2-M *114*

Discussion 115

Experimental Section 116

Construction of vectors *116*

Transformation *117*

Expression and solubility *118*

Purification *118*

References 121

APPENDIX A: CO-CRYSTALLIZATION OF SSK1-R2^{W638A} AND YPD1^{G68Q} . 123

Introduction 123

Co-crystallization of Ssk1-R2^{W638A} and Ypd1^{G68Q} 124

Experimental Section 124

Protein Purification *124*

Crystallization and data collection *125*

Future Directions 126

References 127

APPENDIX B: TABLE OF WEST LAB PRIMERS, PLASMIDS AND CELL STRAINS 129

APPENDIX C: DISCOVERY OF ANTI-BIOFILM ISOCOUMARINS AND ISOBENZOFURANONES FROM A MICROBIAL MAT FUNGUS 132

List of Abbreviations 132

Introduction 132

Structural elucidation of clearanol C 135

Structural elucidation of clearanols D and E 142

Experimental Section 150

General Experimental Procedures 150

Fungal Materials 151

Extraction and Isolation 152

References 155

List of Tables

Table 1. DHp domain H-box residues 6

Table 2. Table of phosphorylated half-lives of Sln1-R1 and Ssk1-R2..... 18

Table 3. X-ray data collection and refinement statistics 39

Table 4. Dissociation constants of Ssk1-R2 salt bridge point mutants. 61

Table 5. K_d values of Ssk1-R2 point mutants that did not affect Ypd1 binding. 63

Table 6. Interface contacts in Sln1-R1/Ypd1 and Ssk1-R2^{W638A}/Ypd1. 77

Table 7. *C. neoformans* Ssk1-R2 construct oligonucleotides used in PCR..... 116

Table 8. PCR and plasmid construction details..... 117

Table 9. Summary of protein purification. 120

Table 10. Summary of NMR data for clearanol C. 135

Table 11. Summary of NMR data for clearanols D and E. 142

List of Figures

Figure 1. Illustration of TCS vs. multi-step phosphorelay. 2

Figure 2. Catalytic and DHp domains of dimeric histidine kinase $EnvZ^{chim}$. 5

Figure 3. Ribbon representation of *S. cerevisiae* HPt protein Ypd1. 8

Figure 4. Ribbon representation of RR protein CheY. 10

Figure 5. Continuum of phosphoryl transfer transition states. 12

Figure 6. Illustration of the *S. cerevisiae* Sln1 pathway. 14

Figure 7. Ribbon representations of the complexes between Ypd1 and Sln1-R1. 16

Figure 8. Ssk1-R2-WT vs. Ssk1-R2-W638A yield. 32

Figure 9. Initial co-crystals of Ypd1 and Ssk1-R2-W638A. 33

Figure 10. Photograph of Ssk1-$R2^{W638A}$/Ypd1 crystal. 33

Figure 11. Photograph of a Ypd1/Ssk1-$R2^{W638A}_{SeMet}$ crystal. 34

Figure 12. Ribbon representation of the complex between Ypd1 and Ssk1-$R2^{W638A}$. .. 35

Figure 13. Molecular surface of Ypd1 showing the location of the T12C mutation..... 44

Figure 14. Chemical structure of 5-iodoacetamidofluorescein (5-IAF). 44

Figure 15. Ssk1-R2-WT vs. Ssk1-R2-W638A fluorescence binding curves. 45

Figure 16. Modeled distance between Ypd1-T12C and W638 in Ssk1-$R2^{W638A}$. 46

Figure 17. Phosphotransfer from Ypd1~P to Ssk1-R2 variants. 47

Figure 18. Phosphorylated half-lives of Ssk1-R2 and Ssk1-R2-W638A. 48

Figure 19. Phosphorimage of Ssk1-R2-W638A~P reverse phosphotransfer to Ypd1.. 49

Figure 20. Ssk1-R2-Q556A Sephadex®-G75purification. 49

Figure 21. Illustration of the location of Ssk1-R2 active site point mutants. 50

Figure 22. Phosphorimage of Ssk1-R2-Q556A~P reverse phosphotransfer to Ypd1... 51

Figure 23. Phosphorimages of Ssk1-R2-S612A and WT Ssk1-R2. 51

Figure 24. Dephosphorylation and half-life of Ssk1-R2-Q556A~P. 52

Figure 25. Half-lives of Ssk1-R2-Q556A~P and Ssk1-W638A~P with Ypd1-H64Q compared to WT Ssk1-R2. 53

Figure 26. Illustration of the location of Ssk1-R2 negative control point mutants. 54

Figure 27. Chitin column purification of Ssk1-R2-D554N. 55

Figure 28. Chitin column purification of Ssk1-R2 and Ssk1-R2-I518S. 55

Figure 29. Purification of Ssk1-R2-V634S. 56

Figure 30. Initial portion of fluorescence binding curves. 57

Figure 31. Phosphorimage of Ypd1~P phosphotransfer to Ssk1-R2 variants. 57

Figure 32. Ssk1-R2-I518S is able to accept a phosphoryl group from GST-HK~P. 58

Figure 33. Molecular surfaces illustrating salt bridge locations of Sln1-R1 and Ssk1-R2^{W638A} and Ypd1. 59

Figure 34. Chitin column purification gels of Ssk1-R2-R524A, Ssk1-R2-K525A and Ssk1-R2-H637A. 60

Figure 35. Fluorescence binding assay of Ssk1-R2 mutants with Ypd1-T12C~F. 61

Figure 36. Ypd1~P phosphotransfer to Ssk1-R2 variants vs. WT Skn7-R3. 62

Figure 37. Illustration of Ssk1-R2 mutants that did not affect Ypd1 binding. 63

Figure 38. Ribbon and stick illustration of salt bridge interactions. 65

Figure 39. Structural comparison of Sln1-R1 and Ssk1-R2^{W638A} with Ypd1. 75

Figure 40. Electrostatic molecular surface representation of the interface view of Sln1-R1 and Ssk1-R2^{W638A} with Ypd1. 80

Figure 41. Distances from Ypd1-H64 to the phosphorylatable aspartate. 81

Figure 42. Illustration of HOG1 pathway in *C. neoformans*. 92

Figure 43. Sequence alignment of *Sc* and *Cn* Ssk1 receiver domains..... 93

Figure 44. Homology models of 3 putative domains of CnSsk1. 94

Figure 45. Schematic representation of all fusion proteins created from CnSsk1. 96

Figure 46. Plasmid map of construct CnR2-B..... 97

Figure 47. SDS-PAGE gel showing the absence of fusion protein CnR2-B..... 97

Figure 48. Plasmid map of construct CnR2-C..... 99

Figure 49. SDS-PAGE gels showing fusion protein CnR2-C. 99

Figure 50. Plasmid map of construct CnR2-D. 101

Figure 51. SDS-PAGE gels showing fusion protein CnR2-D..... 101

Figure 52. Plasmid map of construct CnR2-E. 103

Figure 53. SDS-PAGE gels showing fusion protein CnR2-E. 103

Figure 54. SDS-PAGE gels showing fusion protein CnR2-E-W1147A. 104

Figure 55. Plasmid map of construct CnR2-F. 105

Figure 56. SDS-PAGE gels showing fusion protein CnR2-F. 105

Figure 57. Plasmid map of construct CnR2-G. 106

Figure 58. SDS-PAGE gel showing Ni-NTA purification attempt of CnR2-G. 107

Figure 59. Plasmid map of construct CnR2-H. 108

Figure 60. Plasmid map of construct CnR2-I. 109

Figure 61. SDS-PAGE gel showing fusion protein CnR2-I. 109

Figure 62. Plasmid map of construct CnR2-J. 110

Figure 63. SDS-PAGE gels showing fusion protein CnR2-J. 111

Figure 64. Plasmid map of construct CnR2-K. 112

Figure 65. SDS-PAGE gel showing fusion protein CnR2-K. 112

Figure 66. Plasmid map of construct CnR2-L. 113

Figure 67. SDS-PAGE gel showing fusion protein CnR2-L. 113

Figure 68. Plasmid map of construct CnR2-M. 114

Figure 69. SDS-PAGE gel showing fusion protein CnR2-M. 115

Figure 70. Ssk1-R2^{W638A}/Ypd1^{G68Q} crystal. 124

Figure 71. Diffraction to ~3-4 Å of the co-crystal of Ssk1-R2^{W638A}/Ypd1^{G68Q}. 126

Figure 72. Structures of compounds 1-4. 134

Figure 73. ^{1}H NMR spectrum (400 MHz, methanol-d4) of clearanol C. 137

Figure 74. ^{13}C NMR spectrum (100 MHz, methanol-d4) of clearanol C. 138

Figure 75. gCOSY NMR spectrum (400 MHz, methanol-d4) of clearanol C. 139

Figure 76. HSQC NMR spectrum (400, 100 MHz, methanol-d4) of clearanol C. 140

Figure 77. gHMBC NMR spectrum (400, 100 MHz, methanol-d4) of clearanol C. .. 141

Figure 78. ^{1}H NMR spectrum (400 MHz, methanol-d4) of clearanol D/E. 144

Figure 79. ^{13}C NMR spectrum (100 MHz, methanol-d4) of clearanol D/E. 145

Figure 80. gCOSY NMR spectrum (400 MHz, methanol-d4) of clearanol D/E. 146

Figure 81. HSQC NMR spectrum (400, 100 MHz, methanol-d4) of clearanol D/E... 147

Figure 82. gHMBC NMR spectrum (400, 100 MHz, methanol-d4) clearanol D/E.... 148

Figure 83. ^{1}H NMR variable temperature experiments for clearanol D/E. 149

Abstract

His-Asp signaling systems are ubiquitous in bacteria, archaea, and certain plants and fungi. Little structural information is known about the protein-protein interactions within these signaling pathways, leaving an incomplete picture of how these essential systems operate. In this dissertation, the focus of my work in the West laboratory was the receiver domain of the fungal response regulator protein Ssk1, and its interaction with the histidine phosphotransfer protein Ypd1. In *Saccharomyces cerevisiae* (Sc), Ypd1 interacts with receiver domains from upstream Sln1 and downstream Ssk1 on a common hydrophobic docking site. The main portion of this thesis presents the co-crystal complex of Ypd1 and Ssk1-R2^{W638A} and the accompanying analysis to explain key differences in the physiological functions of Ssk1-R2 and Sln1-R1. Protein-protein interactions were characterized using a newly developed fluorescence binding assay and *in vitro* ^{32}P-phosphotransfer experiments. In addition, the co-crystallization of Ssk1-R2^{W638A} and a point mutant of Ypd1 (Ypd1-G68Q) is described. Ssk1 protein constructs from the human pathogen *Cryptococcus neoformans* (Cn) were designed in order to biochemically characterize interactions with *C. neoformans* Ypd1, but these proteins were either insoluble or inactive. Lastly, my work in the Cichewicz laboratory describes the discovery of three new secondary metabolites from a previously uncharacterized microbial mat fungus (clearanols C, D and E).

Chapter 1: Introduction

Two-component signal transduction

Two-component signal transduction is a form of intracellular communication used by bacteria, archaea, and certain plants and fungi. Basic two-component systems are comprised of two signaling proteins: an upstream sensor histidine kinase (HK) that responds to an extracellular signal by binding ATP and autophosphorylating a histidine residue, and a downstream response regulator (RR) protein that controls the output response of an attached effector domain. RR proteins contain receiver (rec) domains that have conserved aspartate residues as phosphoryl group acceptors from the histidine of the HK. The RR is responsible for transmitting a signal to a downstream effector to elicit an appropriate cellular response (Figure 1, panel A (pg. 2)) (reviewed in[1, 2]).

Basic two-component signaling (TCS) systems are found in bacteria, and they are the primary strategy by which these organisms interact with and respond to their environments. Bacteria use TCS systems for stress response, cell growth and propagation, as well as cell cycle transitions (reviewed in[1, 3-5 6]). Most bacteria contain as many as 20-30 HK-RR pairs, with some possessing hundreds, each responding to different environmental signals, stressors and changes[7-10]. For example, the CheY/CheA chemotaxis system in *Escherichia coli* is one of the most highly studied two component systems in the field[11]. Other well-characterized systems include the oxygen-sensing nitrogen-fixation FixJ/FixL system of *Sinorhizobium meliloti*[12], the osmosensing EnvZ/OmpR system of *E. coli*[13, 14], and the intracellular Mg^{2+} detection system PhoQ/PhoP (reviewed in[15]).

The molecular mechanisms for regulating these large pools of signaling proteins and preventing cross-talk between pathways are not fully understood. Current studies suggest that organisms use a combination of molecular recognition as well as co-localization and concentration-based methods in order to ensure molecular specificity and prevent heterologous cross-talk[8, 16-19]. These same mechanisms would be necessary to maintain the integrity of a single pathway, especially if such a system was expanded to have multiple points of regulation.

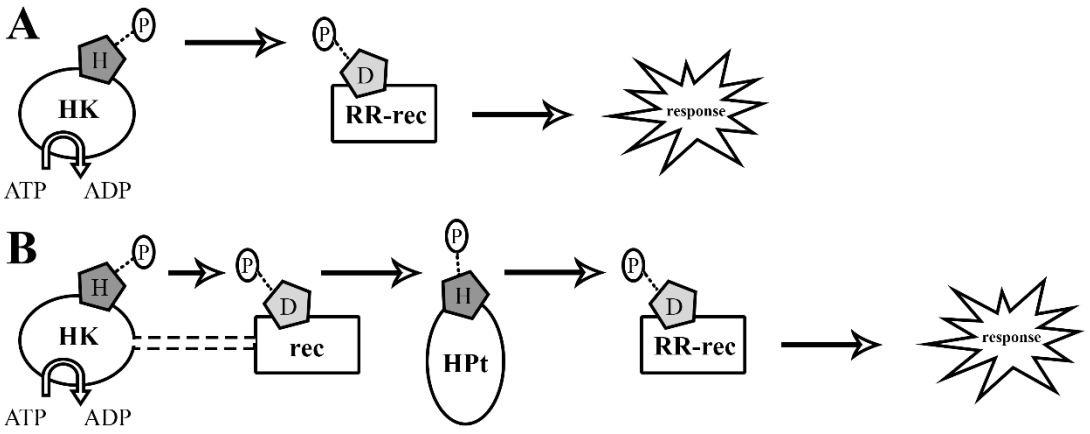

Figure 1. Illustration of TCS vs. multi-step phosphorelay.
Panel A shows a two-component system (HK + RR). Panel B shows an expanded phosphorelay system (hybrid HK + HPt + RR). Non-phospho-accepting domains are not shown for simplicity.

Multi-step phosphorelay systems

A multi-step phosphorelay system is an expanded version of the simple two component system (reviewed in[1, 20-22]). These signaling pathways also use histidine to aspartate phosphotransfer to transmit messages and respond to the external environment. These pathways begin with a hybrid sensor HK, which is similar in structure and function to a basic HK, but contains an attached receiver domain in addition to its HK domain, usually at the C-terminus. The HK responds to an external

stimulus, autophosphorylates on a histidine residue using the γ-phosphate from ATP, and then passes the phosphoryl group intramolecularly to an aspartate residue located in its receiver domain. The receiver domain then interacts with a histidine phosphotransfer protein (HPt), which acts as an intermediate in the signaling pathway. The HPt receives the phosphoryl on a histidine residue and then interacts with the receiver domain located on a downstream RR protein. The RR protein completes the signaling response, either through direct alterations in cellular behavior, or through further activation of downstream pathways (Figure 1, panel B (pg. 2)) (reviewed in[1]). Multi-step phosphorelay pathways and HPt domains are most commonly found in certain eukaryotic organisms like plants and fungi, but they can also be found in bacteria, such as the *E. coli* proteins ArcB and BarA[9, 23]. It has been suggested that hybrid histidine kinases make up approximately 30% of all known bacterial kinase proteins, though not all are necessarily involved in expanded phosphorelays[22, 24].

Use of a multi-step phosphorelay provides an organism with several possible advantages when compared to simple TCS systems. The increased number of signaling components provides additional points of regulation for the cell[25]. Mathematical modeling of phosphorelays suggests that the increased length of a phosphorelay can result in a more ultrasensitive character[26, 27]. This ultra-sensitivity imparts a switch-like quality to the intermediate components, leading to very low responses for inputs below a determined threshold, and very high and rapid responses once the threshold has been reached[26]. This results in a sigmoidal signal-response curve that can be fine-tuned as needed by the organism. The presence of a signal threshold will also reduce pathway activation through promiscuous cross-talk and filter out input noise[26-28].

Histidine kinase proteins

In TCS pathways, HK proteins are responsible for sensing, internalizing and propagating external stimuli to the cellular machinery required for an appropriate cellular response. There are different classes of HKs: proteins with extracellular, transmembrane or intracellular sensor domains (reviewed in[1, 21, 29]). In general, the canonical HK is a multi-domain homodimer with an extracellular sensor domain. The architecture of an HK monomer begins with an N-terminal transmembrane helix that leads to the extracellular sensory domain (reviewed in[30]). The extracellular sensory domain is linked to another antiparallel transmembrane helix which bundles with the first helix. This is followed by a variable cytoplasmic signal transducing domain (e.g. PAS, HAMP or GAF domain), followed by the dimerization and histidine phosphotransfer (DHp) domain which is composed of two antiparallel helices. A flexible loop connects the DHp and ATP-binding catalytic domain at the C-terminus. Two monomers form a homodimer resulting in the DHp domains forming a highly conserved 4-helix bundle. Once the signal is transduced through the protein assembly, the HK switches from an inactive to an active state[31], and the autophosphorylation reaction begins on the catalytic domain. A conserved histidine residue is phosphorylated on helix 1 of the DHp domain. After the histidine is phosphorylated, the phosphoryl is passed to an aspartate residue of a receiver domain. If the protein has phosphatase activity, the DHp domain is also the site of this reaction (reviewed in[30]).

On a homodimeric HK, the autophosphorylation mechanism was thought to occur only in *trans* with regard to the dimeric subunits[32-36]. Recent studies suggest that this is not the case, with *Staphylococcus aureus* PhoR[37] and *E. coli* ArcB[38] behaving in

a *cis* manner exclusively. Recent studies have shown that either mechanism is possible, and that the handedness of the hairpin loop connecting the two DHp helices determines which method is used[39, 40]. If the loop turns right, the autophosphorylation proceeds in *trans* with the catalytic domain in closer proximity to its partner's phosphorylatable histidine. If the loop turns left, the autophosphorylation reaction occurs in *cis* with the catalytic domain in closer proximity to its own phosphorylatable histidine[41]. As an example, an engineered catalytic domain bound with ATP is poised to autophosphorylate the histidine residue in *cis* (Figure 2), adapted from Casino et al.[39]



Figure 2. Catalytic and DHp domains of dimeric histidine kinase EnvZ^{chim}.
Bound ATP is poised to autophosphorylate in *cis* (PDB ID: 4KP4). Monomer A (green) is shown with bound Mg^{2+} (magenta) and ATP in position to phosphorylate the active site histidine residue (red). Monomer B (cyan) does not contain bound ATP.

HK sensor domains are typically extracellular, asymmetrical and have many different modes of ligand binding, both in location and in method of binding[2, 29, 42, 43]. Additional classes of sensor domains do exist, such as transmembrane and intracellular

receptors. Some examples of HK ligands are aspartate, triethylamine *N*-oxide, nitrate, magnesium, citrate, malonate and other ligand-bound proteins[44-47]. Regardless of how the signal is received, ligand-binding causes a structural rearrangement from an inactive conformation to an active conformation, initiating autophosphorylation by the kinase domain (reviewed in[30]).

The catalytic domain is a highly conserved α/β sandwich composed of three α-helices packed against five antiparallel β-strands. ATP binds between two helices and is held in place by a loop called the "ATP lid." ATP associates with conserved sequence motifs called N, G1, G2 and F that comprise the nucleotide binding sites[48]. A hydrophobic "gripper" helix associates with the DHp domain in different orientations during the transition from the inactive to active conformation (reviewed in[30]). Once the active conformation is achieved, the CA and DHp domain are interfacing through specific residue contacts. A string of seven highly conserved residues on helix 1 of the DHp domain (H box) participates in catalysis (Table 1). Residues 5-6 participate in helix bending; basic residue 4 stabilizes the negatively charged phosphate groups on ATP, acidic residue 2 acts as a hydrogen bond acceptor or general acid/base while histidine 1 is phosphorylated using the γ-phosphate of ATP to form a high energy Nε-P bond[30].

Table 1. DHp domain H-box residues

1	**2**	**3**	**4**	**5**	**6**	**7**
H	D/E	L/I	K/R	T/N	P	L

Histidine phosphotransfer proteins

Histidine phosphotransfer proteins are proteins that appear in multi-step phosphorelays (reviewed in[49]). Their function is to accept a phosphoryl group from an aspartate on an upstream receiver domain of a hybrid histidine kinase and shuttle it to an aspartate on a downstream RR (reviewed in[1]). HPt proteins contain a conserved 4-helix bundle core, reminiscent of the HK 4-helix bundle. The structure of Ypd1, an HPt protein from *S. cerevisiae*, was solved in 1999[50, 51] (Figure 3 (pg. 8)), revealing the conservation of structure and function of HPt domains. There are several highly conserved residues that contribute to HPt protein activity. A residue four positions away (n+4) from the phosphorylatable histidine is a highly conserved glycine that potentially allows access to the histidine during phosphotransfer. A structurally significant glycine located between the C and D helices is also highly conserved, and is likely essential to the hydrophobic reverse turn between the C and D helices. Two conserved basic residues are proposed to participate in the proper antiparallel orientation of the C and D helices. In addition, a polar residue (glutamine or glutamate) hydrogen bonds with the phosphorylatable histidine and with the assistance of a water molecule, positions the histidine in the proper orientation for phosphotransfer[52].

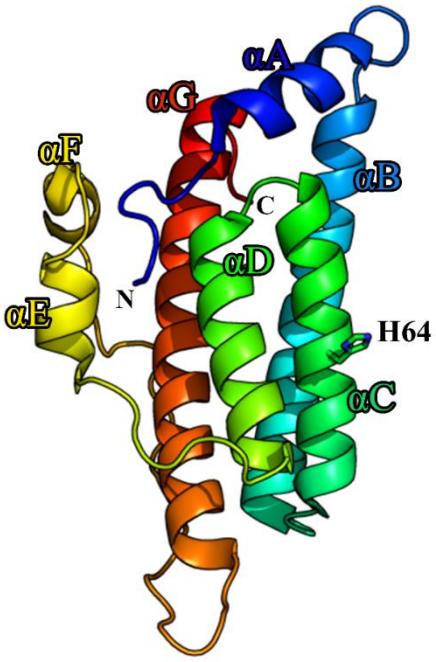

Figure 3. Ribbon representation of *S. cerevisiae* HPt protein Ypd1.
The Ypd1 structure was solved in 1999[50] (PDB ID: 1QSP). Alpha helices (A-G) are labeled and the phospho-accepting histidine residue (H64) is shown in stick.

Response regulator proteins

Response regulators are signaling proteins that control output responses in all TCS and phosphorelay pathways. A defining feature of an RR is the presence of a receiver domain. Receiver domains have highly conserved tertiary structures and contain a phosphorylatable active site aspartate residue (reviewed in[1, 53]). Although structurally conserved, sequence identity is relatively low, ranging from 25-30% within the large superfamily of RR protein receiver domains (>300,000 in the National Center for Biotechnology Information (NCBI) database: http://pfam.xfam.org/family/response_reg, accessed 2015). RR proteins can be either single or multi-domain proteins[1, 54]. For example, CheY is a bacterial chemotaxis RR that is comprised of only a single receiver domain[55]. Bacterial RR proteins typically

contain an N-terminal receiver domain and a C-terminal effector domain. In eukaryotes, many receiver domains are found at the C-terminal end of the RR protein. The purpose of all receiver domains is to accept a phosphoryl group from a phospho-histidine. Aspartate phosphorylation stabilizes a universally conserved allosteric rearrangement of the receiver domain along the β4α4 and β5α5 surface of the protein (Figure 4 (pg. 10)). Post-activation protein function can vary widely between signaling pathways.

Functions of RR proteins are extremely diverse and depend greatly on the identity of the effector domain. In addition to being involved in many different types of signaling pathways (oxidative stress response[56], hyperosmotic stress response[57], cell wall stress[58], chemotaxis[59], biofilm formation[60], etc.), they perform many different functions on various cellular levels. Depending on the effector domain, an RR protein can affect the cell at the transcriptional, post-transcriptional or post-translational level. The majority of effector domains function as transcription factors, grouped into three major subfamilies based on the homology of their DNA-binding domains[1, 53, 61]. Other known effector domain functions include RNA-binding, ligand-binding, protein-binding, and enzymatic activity (reviewed in[53]). In addition to this diversity, the functions of many effector domains remain unknown[62].

Receiver domains almost invariably adopt a $(\beta\alpha)_5$ topology (reviewed in[53]). Alternating beta strands and alpha helices form a parallel beta-sheet flanked on both sides by 5 amphipathic alpha helices (Figure 4 (pg. 10)). Conserved residues that contribute to phosphotransfer are primarily located at the C-terminal ends of the beta strands. The phosphorylatable aspartate residue is located at the end of the β3 strand

and is one of three conserved acidic residues that participate in binding a divalent metal cation essential for phosphotransfer activity[63]. The other two acidic residues are located at the tip of the β1 strand. Other active site residues include a lysine (β5)[64] and a conserved "switch" residue, a threonine/serine (β4)[65], that participate in the phospho-induced conformational change. A structurally essential proline is located on the loop between β3 and α3 followed by a glycine four residues away. A moderately conserved aromatic residue (Phe/Tyr) on the α5 helix is also referred to as a "switch residue" along with the conserved threonine/serine that interacts with the phosphoryl group. There is evidence that RRs sometimes act in concert with other proteins for activation[66] and atypical RRs have been found that do not rely on phosphorylation for activation[67].

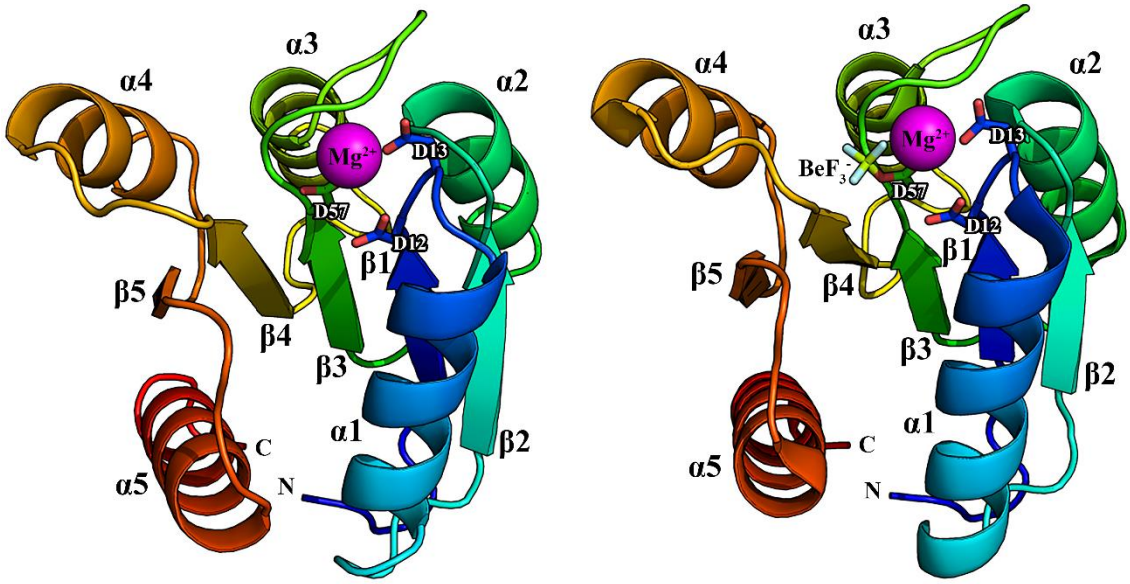

Figure 4. Ribbon representation of RR protein CheY.
Beta strands (1-5) and alpha helices (1-5) are labeled; the phospho-accepting aspartate residue (D57) and the Mg^{2+}-coordinating aspartates (D12 and D13) are shown in stick. Mg^{2+} is shown as a magenta sphere. The left panel shows the inactive structure of CheY from *Salmonella enterica*[68] (PDB ID: 2CHE). The right panel shows the BeF^{3-}-activated structure of CheY from *E. coli*[69] (PDB ID: 1FQW). This figure illustrates that upon activation, an allosteric movement occurs from α4 through α5.

Although receiver domains accept phosphoryl groups from phospho-histidine, they play a catalytic role in phosphotransfer chemistry and are not passive "receivers." Many receiver domains have the ability to autophosphorylate using small molecule phospho-donors[70, 71]. The reaction is believed to involve a nucleophilic attack on the phosphate group by the aspartate carboxylate oxygen not bound to the divalent metal cation[72]. Protein-protein phosphotransfer likely occurs in the same fashion. Receiver domains also have autodephosphorylation activity that is believed to occur by the reverse mechanism, involving an activated water molecule executing an in-line nucleophilic attack on the phosphorus atom[73] as the negatively charged oxygens are stabilized by the active site residues and metal ion[1, 63].

Phosphotransfer mechanism

The mechanism of His-Asp protein phosphotransfer in TCSs cannot be directly visualized because the static nature of crystal structures can only show the inactive and activate conformations. However, research has been done on other signaling enzymes (reviewed in[74]) and a recent review of the current understanding of biological phosphoryl transfer mechanisms is an excellent resource that can add to our understanding of RR activity[75]. Response regulators are believed to exist in an equilibrium of "inactive" and "active" conformations, and the active states are stabilized by phosphorylation[76].

In general, a histidine or aspartate acts as a nucleophile and attacks the positively charged phosphorus of the phosphoryl group covalently bound to the donor atom. A divalent metal cation in the active site of RRs is essential for this reaction to occur in either direction. This metal is likely responsible for neutralizing charges on the

pentavalent transition state and it is hypothesized that this stabilization allows for the mechanism to occur[77]. Factors that affect the character of a phosphotransfer mechanism are the strength of the attacking nucleophile and the stability of the leaving group. In proteins, these variables are strongly influenced by amino acid side chain or backbone contributions that can donate or withdraw electrons from the donor or acceptor.

Mechanisms for phosphoryl transfer are believed to occur with partial associative character[78], including Sln1-R1 to Ypd1[79]. Known cell signaling enzymes range from ≤8% – 50% associative character[74]. In the case of protein phosphotransfer, mechanisms are not described as associative or dissociative, but defined along a continuum, depending on the tightness of the hypothesized transition state (Figure 5). Assumptions about the mechanistic pathway have been inferred from co-crystal structures by measuring donor-acceptor atom distances and active site geometries[39, 78].

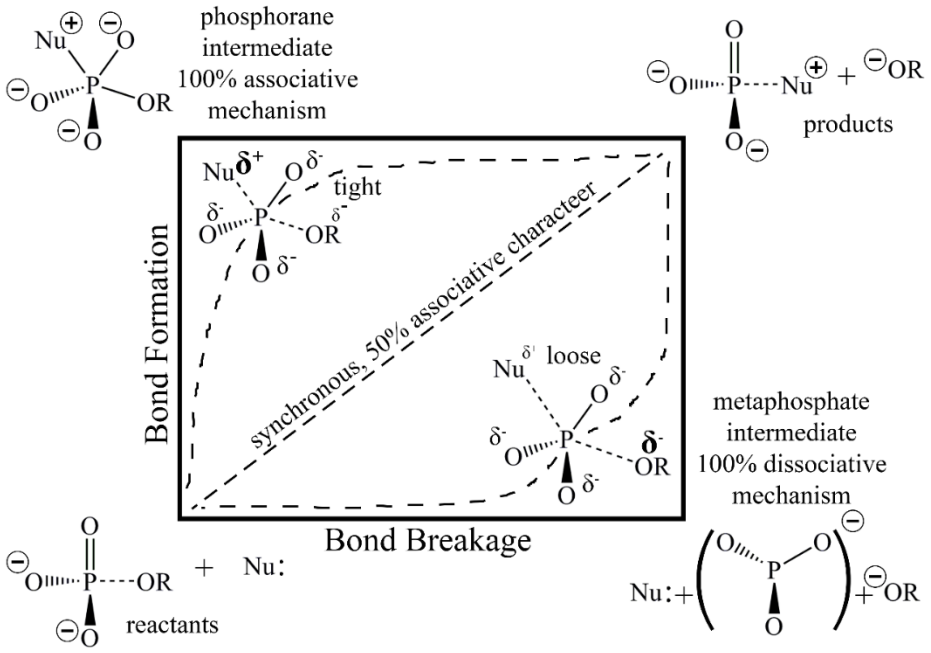

Figure 5. Continuum of phosphoryl transfer transition states.
Adapted from[75].

S. cerevisiae Sln1 phosphorelay pathway

The yeast *S. cerevisiae* has been used extensively as a model organism[80]. This is because of its genetic tractability and the presence of only a single multi-step phosphorelay system. Pathogenic fungi contain homologous pathways that are not found in mammals, making these systems valuable putative drug targets. The highly nonspecific nature of current antifungal treatments has greatly increased the urgency to understand these signaling pathways[81].

The Sln1 pathway was first identified in the early 1990s[82, 83] and has been studied extensively as an archetypal phosphorelay system. The main function of the pathway in *S. cerevisiae* is to trigger downstream stress reactions such as the HOG1 pathway in response to hyperosmotic stress or the Skn7 transcription factor to maintain cell wall integrity[84] or respond to oxidative stress[85].

Sln1 is a homodimeric transmembrane hybrid histidine kinase that contains 1220 residues[86]. It is catalytically active under normal environmental conditions; it autophosphorylates on a histidine residue, passes this phosphoryl to an aspartate on its C-terminal receiver domain (R1) which passes the phosphoryl to Ypd1, the 167- residue intermediate HPt protein. Ypd1 was identified as playing a role in the Sln1 pathway in 1996[86] and it is dispersed throughout the cytoplasm and nucleus[87]. Under normal conditions, Ypd1 constitutively phosphorylates Ssk1, a downstream response regulator, suppressing its ability to activate the HOG1 pathway[86]. Under hyperosmotic stress, Sln1 responds to changes in turgor pressure and membrane fluidity (reviewed in[88]), and unphosphorylated Ssk1 accumulates in the cell and interacts with Ssk2 or Ssk22, MAPKKKs that initiate the HOG1 pathway glycerol production response[86]. Under cell

wall or oxidative stress, Ypd1 phosphorylates the response regulator, Skn7, which is located in the nucleus. Skn7 is a transcription factor and upregulates the appropriate genes in response to stress[89, 90] (Figure 6).

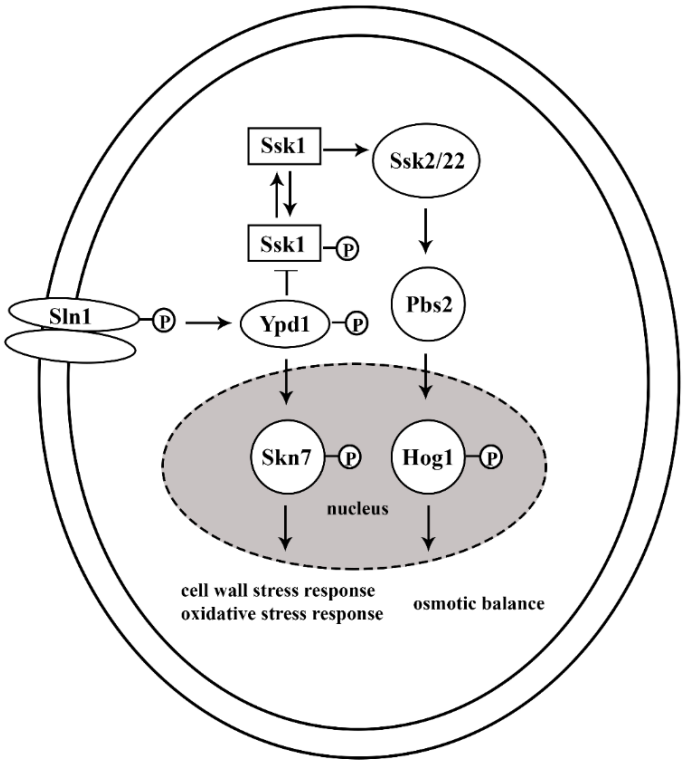

Figure 6. Illustration of the *S. cerevisiae* Sln1 pathway.
Under normal conditions, Ypd1~P negatively regulates the HOG1 pathway via Ssk1. Under hyperosmotic stress, dephosphorylated Ssk1 activates the HOG1 pathway.

Differences between Ypd1 cognate receiver domains: Sln1-R1 and Ssk1-R2

One of the main points of interest about the *S. cerevisiae* model Sln1 pathway is the ability of Ypd1 to interact with multiple receiver domains that are highly structurally similar yet result in distinctly different physiological outcomes. Ypd1 interacts with an upstream receiver domain (Sln1-R1) and two downstream receiver domains (Ssk1-R2 and Skn7-R3) on the same hydrophobic docking site[91]. The forward

movement of the phosphorelay (Sln1-R1→Ypd1→Ssk1-R2) despite the similarity of Ypd1-interactions with its receiver domains, raises the fascinating question of how small changes in the receiver domains such as amino acid sequence or structural position can induce dissimilar biological behaviors. Following is a short review of the documented differences in biochemical behavior between Sln1-R1 and Ssk1-R2 *in vitro* and *in vivo*.

In vitro rapid-quench phosphotransfer experiments show that the maximum rate of phosphotransfer from Sln1-R1 to Ypd1 is 29 ± 3 s^{-1}[1,92]. The maximum rates of phosphotransfer from Ypd1 to each receiver domain are 230 ± 130 s^{-1} (Sln1-R1, reverse transfer) and 160 ± 70 s^{-1} (Ssk1-R2, forward transfer)[92]. With respect to the phosphotransfer reaction, a phosphoryl group passing from phosphohistidine to a receiver domain aspartate is kinetically and energetically favored[93, 94]. In the case of the Sln1 pathway, however, the phosphorelay must progress in the forward direction (Sln1-R1 → Ypd1 → Ssk1-R2), so there must be important differences between the encounter complexes. The rate of complex dissociation between Ypd1 and Sln1-R1 is approximately 30-fold faster than the rate of reverse phosphotransfer, allowing 97% of Ypd1 to remain phosphorylated and proceed in the forward direction. When Ypd1 encounters Ssk1-R2, the forward reaction is strongly favored and no reverse reaction from Ssk1-R2 to Ypd1 was detected under the conditions tested[92].

In addition to phosphotransfer kinetics, key residues on Ypd1 were found to play an important role in phosphotransfer from Sln1-R1 to Ypd1 but have no effect in the phosphorelay from Ypd1 to Ssk1-R2. Ypd1 K67 and R90 were found to play an important role in positioning of the C and D helices and the electrostatic stabilization of

phosphorylated H64[92]. From the Sln1-R1/Ypd1 crystal structures (Figure 7), Q86 formed an intramolecular hydrogen bond to the imidazole ring of H64, likely orienting the residue for correct phosphoryl transfer from Sln1-R1[79, 95]. This evidence indicates that the electrostatic stabilization and orientation of Ypd1-H64 plays an essential role for the reception of a phosphoryl group from an upstream donor, but not necessarily for the forward phosphotransfer to Ssk1-R2.

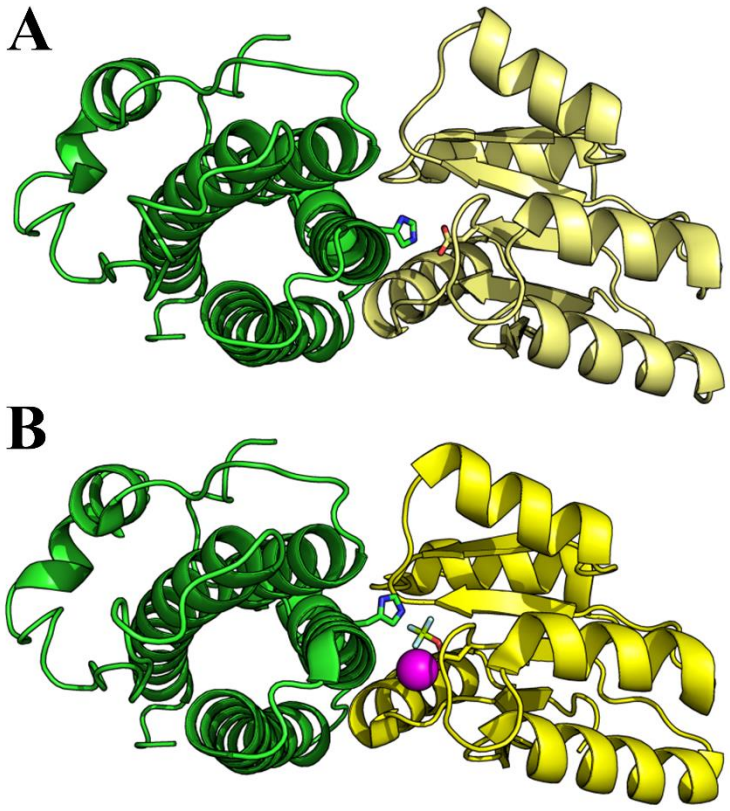

Figure 7. Ribbon representations of the complexes between Ypd1 and Sln1-R1.
The apo co-crystal structure of *S. cerevisiae* Sln1-R1/Ypd1 (A) was solved in 2003[96] (PDB ID: 1OXB) and the BeF^{3-} -activated complex (B) was solved in 2008[79] (PDB ID: 2R25).

One residue was found to be essential for adequate phosphoryl transfer between Ypd1 and both cognate receiver domains: G68. This glycine, located four residues from the phosphorylatable histidine, is almost completely conserved throughout HPt and HK domains (West lab, unpublished data). In the case of Sln1-R1 to Ypd1 transfer, mutating G68 to glutamine decreased the rate of phosphotransfer by approximately 9700-fold. Between Ypd1 and Ssk1-R2, the decrease in phosphoryl transfer was approximately 670-fold[92]. In conclusion, disruption of the Ypd1 n+4 glycine is approximately 15-fold more kinetically disruptive for accepting a phosphoryl from Sln1-R1 than transferring a phosphoryl to Ssk1-R2.

In addition to structural and *in vitro* data, *in vivo* experiments indicate that unphosphorylated Ssk1 exists as a dimer *in vivo*, which activates Ssk2 resulting in HOG1 activation[97]. The *S. cerevisiae* cell can turn off the HOG1 glycerol response by two known mechanisms: phosphorylated Ssk1 can dimerize with unphosphorylated Ssk1 and inhibit its activity[97]; unphosphorylated Ssk1 is quickly degraded by the ubiquitin-proteasome system[98].

In vitro, receiver domains of Sln1 and Ssk1 show dramatically different phosphorylated lifetimes in the presence of Ypd1. Ypd1 stabilizes the presence of Ssk1-R2~P and has no measureable effect on Sln1-R1~P[99]. This suggests the presence of a stable Ypd1/Ssk1-R2 complex[99, 100]. These data support the physiological roles of Sln1-R1 and Ssk1-R2. Sln1 must phosphorylate Ypd1 and quickly dissociate so that the phosphoryl can be passed to Ssk1. Since phospho-Ssk1 is the inactive form of the protein, a stable complex between phospho-Ssk1 and Ypd1 would prevent the active unphosphorylated dimer of Ssk1 from accumulating and activating the HOG1 pathway.

Table 2. Table of phosphorylated half-lives of Sln1-R1 and Ssk1-R2.
Adapted from[99] . H64Q is an unphosphorylatable mutant.

Receiver domain	buffer	+Ypd1	+Ypd1-H64Q
Sln1-R1	$t_{½}$ ~13 minutes	$t_{½}$ ~17 min	$t_{½}$ ~18 min
Ssk1-R2	$t_{½}$ ~13 minutes	$t_{½}$ ~ 40 hours	$t_{½}$ ~ 2.5 hours

In an attempt to understand the mechanism of Ssk1-R2~P/Ypd1 dissociation, the half-life of Ssk1-R2~P was tested in the presence of osmolytes. It was found that low concentrations of NaCl and glycerol decreased the half-life of Ssk1-R2~P in the presence of Ypd1 2-fold, but higher concentrations (up to 1 M) favored the stabilization of Ssk1-R2~P[101]. These data corroborate the cell's physiological response to hyperosmotic stress. Initially, in the presence of high salt, water will be drawn out of the cell, temporarily increasing the intracellular osmolyte concentrations. Under these circumstances, accumulation of unphosphorylated Ssk1-R2 would be favorable to turn on the HOG1 pathway. Upon glycerol production and return to homeostasis, the stabilization of Ssk1-R2~P would be beneficial once again.

Kinetic data support a significantly different interaction between Ypd1 and its cognate receiver domains (Sln1-R1 and Ssk1-R2), and there is strong data to support that Ypd1 and Ssk1-R2 form a stable phosphorylated complex[99, 100] while Ypd1 and Sln1-R1 rapidly dissociate. However, yeast two-hybrid data show that the binding interface of Ypd1 is nearly identical for all of its cognate receiver domains. Ypd1 contains a hydrophobic patch surrounding the phosphorylatable histidine that acts as the binding interface for Sln1-R1, Ssk1-R2 and Skn7-R3[91, 102]. This indicates that there

must be minor but significant differences between the receiver domains and their interactions with Ypd1 that result in distinct physiological activities.

Research Focus

Since the 1990's, structural and biochemical data have been accumulating to shed light on the differences between Ypd1's physiological interactions with Sln1-R1 and Ssk1-R2. To date, there has been no structural information about Ssk1 to help elucidate the mechanisms behind these key differences. In this dissertation, I present the 2.80 Å co-crystal structure of a complex between *S. cerevisiae* Ypd1 and the receiver domain of $Ssk1^{W638A}$. The crystal structure illustrates differences from Sln1-R1/Ypd1 in electrostatic interactions and active site encounter distances that may provide insight into the phosphorelay pathway regulation. These data are supported by *in vitro* binding affinity and phosphotransfer assays that compare and contrast wild type (WT) protein interactions with Ssk1 point mutants. Together, these data show structurally-based electrostatic potential interactions and key amino acids that are likely involved in the stable formation of an Ssk1~P/Ypd1 complex. The electrostatic contributions to complex formation can help explain the constitutive phosphorylation of Ssk1 in the Sln1 pathway of *S. cerevisiae*.

In order to elucidate more detailed information about the phosphorelay protein-protein interactions of human pathogens, protein constructs of *Cryptococcus neoformans* Ssk1-R2 were designed. These proteins were created to characterize binding interactions with *C. neoformans* Ypd1, but these constructs were either insoluble or inactive.

References

[1] West, A. H., and Stock, A. M. (2001) Histidine kinases and response regulator proteins in two-component signaling systems, *Trends Biochem. Sci. 26*, 369-376.

[2] Stock, A. M., Robinson, V. L., and Goudreau, P. N. (2000) Two-component signal transduction, *Annu Rev Biochem 69*, 183-215.

[3] MacRitchie, D. M., Buelow, D. R., Price, N. L., and Raivio, T. L. (2008) Two-component signaling and gram negative envelope stress response systems, *Adv Exp Med Biol 631*, 80-110.

[4] Whistler, C. A., Corbell, N. A., Sarniguet, A., Ream, W., and Loper, J. E. (1998) The two-component regulators GacS and GacA influence accumulation of the stationary-phase sigma factor ς(S) and the stress response in *Pseudomonas fluorescens* Pf-5, *J. Bacteriol. 180*, 6635-6641.

[5] Martinez-Wilson, H. F., Tamayo, R., Tischler, A. D., Lazinski, D. W., and Camilli, A. (2008) The *Vibrio cholerae* hybrid sensor kinase VieS contributes to motility and biofilm regulation by altering the cyclic diguanylate level, *J. Bacteriol. 190*, 6439-6447.

[6] Cotter, P. A., and Stibitz, S. (2007) c-di-GMP-mediated regulation of virulence and biofilm formation, *Curr Opin Microbiol 10*, 17-23.

[7] Laub, M. T., Biondi, E. G., and Skerker, J. M. (2007) Phosphotransfer profiling: systematic mapping of two-component signal transduction pathways and phosphorelays, *Meth. Enzymol. 423*, 531-548.

[8] Laub, M. T., and Goulian, M. (2007) Specificity in two-component signal transduction pathways, *Annu. Rev. Genet. 41*, 121-145.

[9] Mizuno, T. (1997) Compilation of all genes encoding two-component phosphotransfer signal transducers in the genome of *Escherichia coli*, *DNA Research 4*, 161-168.

[10] Gooderham, W. J., and Hancock, R. E. W. (2009) Regulation of virulence and antibiotic resistance by two-component regulatory systems in *Pseudomonas aeruginosa*, *FEMS Microbiol Rev 33*, 279-294.

[11] Hazelbauer, G. L. (2012) Bacterial chemotaxis: the early years of molecular studies, *Annu. Rev. Microbiol. 66*, 285-303.

[12] Reyrat, J. M., David, M., Blonski, C., Boistard, P., and Batut, J. (1993) Oxygen-regulated in vitro transcription of *Rhizobium meliloti* nifA and fixK genes, *J. Bacteriol. 175*, 6867-6872.

[13] Russo, F. D., and Silhavy, T. J. (1991) EnvZ controls the concentration of phosphorylated OmpR to mediate osmoregulation of the porin genes, *J Mol Biol 222*, 567-580.

[14] Cai, S. J., and Inouye, M. (2002) EnvZ-OmpR interaction and osmoregulation in *Escherichia coli*, *J Biol Chem 277*, 24155-24161.

[15] Groisman, E. A. (2001) The pleiotropic two-component regulatory system PhoP-PhoQ, *J. Bacteriol. 183*, 1835-1842.

[16] Schwartz, M. A., and Madhani, H. D. (2004) Principles of MAP kinase signaling specificity in *Saccharomyces cerevisiae*, *Annu Rev Genet 38*, 725-748.

[17] Ubersax, J. A., and Ferrell, J. E., Jr. (2007) Mechanisms of specificity in protein phosphorylation, *Nat Rev Mol Cell Biol 8*, 530-541.

[18] Skerker, J. M., Prasol, M. S., Perchuk, B. S., Biondi, E. G., and Laub, M. T. (2005) Two-Component signal transduction pathways regulating growth and cell cycle progression in a bacterium: a system-level analysis, *PLoS Biology 3*, e334.

[19] Newman, J. R., and Keating, A. E. (2003) Comprehensive identification of human bZIP interactions with coiled-coil arrays, *Science 300*, 2097-2101.

[20] Stock, A. M., and West, A. H. (2002) Response regulator proteins and their interactions with histidine protein kinases, In *Histidine kinases in signal transduction* (Inouye, M., and Dutta, R., Eds.), pp 237-271, Academic Press, New York.

[21] Stock, A. M., Robinson, V. L., and Goudreau, P. N. (2000) Two-component signal transduction, *Annu. Rev. Biochem. 69*, 183-215.

[22] Appleby, J. L., Parkinson, J. S., and Bourret, R. B. (1996) Signal transduction via the multi-step phosphorelay: Not necessarily a road less traveled, *Cell 86*, 845-848.

[23] Tsuzuki, M., Ishige, K., and Mizuno, T. (1995) Phosphotransfer circuitry of the putative multi-signal transducer, ArcB, of *Escherichia coli*: in vitro studies with mutants, *Mol. Microbiol. 18*, 953-962.

[24] Chang, C. H., Zhu, J., and Winans, S. C. (1996) Pleiotropic phenotypes caused by genetic ablation of the receiver module of the *Agrobacterium tumefaciens* VirA protein, *J. Bacteriol. 178*, 4710-4716.

[25] Burbulys, D., Trach, K. A., and Hoch, J. A. (1991) Initiation of sporulation in *B. subtilis* is controlled by a multicomponent phosphorelay, *Cell 64*, 545-552.

[26] Csikász-Nagy, A., Cardelli, L., and Soyer, O. S. (2010) Response dynamics of phosphorelays suggest their potential utility in cell signalling, *J R Soc Interface* 10.1098/rsif.2010.0336.

[27] Kothamachu, V. B., Feliu, E., Wiuf, C., Cardelli, L., and Soyer, O. S. (2013) Phosphorelays provide tunable signal processing capabilities for the cell, *PLoS Comput Biol 9*, e1003322.

[28] Kim, J. R., and Cho, K. H. (2006) The multi-step phosphorelay mechanism of unorthodox two-component systems in *E. coli* realizes ultrasensitivity to stimuli while maintaining robustness to noises, *Comput Biol Chem 30*, 438-444.

[29] Jung, K., Fried, L., Behr, S., and Heermann, R. (2012) Histidine kinases and response regulators in networks, *Curr Opin Microbiol 15*, 118-124.

[30] Bhate, M. P., Molnar, K. S., Goulian, M., and DeGrado, W. F. (2015) Signal transduction in histidine kinases: insights from new structures, *Structure 23*, 981-994.

[31] Dago, A. E., Schug, A., Procaccini, A., Hoch, J. A., Weigt, M., and Szurmant, H. (2012) Structural basis of histidine kinase autophosphorylation deduced by

integrating genomics, molecular dynamics, and mutagenesis, *PNAS 109*, E1733-E1742.

[32] Ninfa, E. G., Atkinson, M. R., Kamberov, E. S., and Ninfa, A. J. (1993) Mechanism of autophosphorylation of *Escherichia coli* nitrogen regulator II (NRII or NtrB): trans-phosphorylation between subunits, *J. Bacteriol. 175*, 7024-7032.

[33] Yang, Y., and Masayori, I. (1991) Intermolecular complementation between two defective mutant signal- transducing receptors of *Escherichia coli*, *PNAS 88*, 11057-11061.

[34] Swanson, R. V., Bourret, R. B., and Simon, M. I. (1993) Intermolecular complementation of the kinase activity of CheA, *Mol. Microbiol. 8*, 435-441.

[35] George Cisar, E. A., Geisinger, E., Muir, T. W., and Novick, R. P. (2009) Symmetric signalling within asymmetric dimers of the *Staphylococcus aureus* receptor histidine kinase AgrC, *Mol Microbiol 74*, 44-57.

[36] Brencic, A., Xia, Q., and Winans, S. C. (2004) VirA of *Agrobacterium tumefaciens* is an intradimer transphosphorylase and can actively block vir gene expression in the absence of phenolic signals, *Mol. Microbiol. 52*, 1349-1362.

[37] Casino, P., Rubio, V., and Marina, A. (2009) Structural insight into partner specificity and phosphoryl transfer in two-component signal transduction, *Cell 139*, 325-356.

[38] Pena-Sandoval, G. R., and Georgellis, D. (2010) The ArcB sensor kinase of *Escherichia coli* autophosphorylates by an intramolecular reaction, *J. Bacteriol. 192*, 1735-1739.

[39] Casino, P., Miguel-Romero, L., and Marina, A. (2014) Visualizing autophosphorylation in histidine kinases, *Nat Commun 5*.

[40] Casino, P., Rubio, V., and Marina, A. (2009) Structural insight into partner specificity and phosphoryl transfer in two-component signal transduction, *Cell 139*, 325-336.

[41] Ashenberg, O., Keating, A. E., and Laub, M. T. (2013) Helix bundle loops determine whether histidine kinases autophosphorylate in *cis* or in *trans*, *J. Mol. Biol. 425*, 1198-1209.

[42] Capra, E. J., and Laub, M. T. (2012) Evolution of two-component signal transduction systems, *Annu Rev Microbiol 66*, 325-347.

[43] Gao, R., and Stock, A. M. (2009) Biological insights from structures of two-component proteins, *Annu Rev Microbiol 63*, 133-154.

[44] Cheung, J., and Hendrickson, W. A. (2009) Structural analysis of ligand stimulation of the histidine kinase NarX, *Structure (London, England : 1993) 17*, 190-201.

[45] Chervitz, S. A., and Falke, J. J. (1996) Molecular mechanism of transmembrane signaling by the aspartate receptor: a model, *PNAS 93*, 2545-2550.

[46] Moore, Jason O., and Hendrickson, Wayne A. (2012) An asymmetry-to-symmetry switch in signal transmission by the histidine kinase receptor for TMAO, *Structure 20*, 729-741.

[47] Yu, E. W., and Koshland, D. E. (2001) Propagating conformational changes over long (and short) distances in proteins, *PNAS 98*, 9517-9520.

[48] Kim, D.-J., and Forst, S. (2001) Genomic analysis of the histidine kinase family in bacteria and archaea, *Microbiology 147*, 1197-1212.

[49] Fassler, J. S., and West, A. H. (2013) Histidine phosphotransfer proteins in fungal two-component signal transduction pathways, *Eukaryot Cell 12*, 1052-1060.

[50] Xu, Q., Nguyen, V., and West, A. H. (1999) Purification, crystallization, and preliminary X-ray diffraction analysis of the yeast phosphorelay protein YPD1, *Acta Cryst. D55*, 291-293.

[51] Xu, Q., and West, A. H. (1999) Conservation of structure and function among histidine-containing phosphotransfer (HPt) domains as revealed by the crystal structure of YPD1, *J. Mol. Biol. 292*, 1039-1050.

[52] Janiak-Spens, F., and West, A. H. (2000) Functional roles of conserved amino acid residues surrounding the phosphorylatable histidine of the yeast phosphorelay protein YPD1, *Mol. Microbiol. 37*, 136-144.

[53] Bourret, R. B. (2010) Receiver domain structure and function in response regulator proteins, *Curr. Opin. Microbiol. 13*, 142-149.

[54] Gao, R., and Stock, A. M. (2010) Molecular strategies for phosphorylation-mediated regulation of response regulator activity, *Curr. Opin. Microbiol. 13*, 160-167.

[55] Stock, A. M., Mottonen, J. M., Stock, J. B., and Schutt, C. E. (1989) Three-dimensional structure of CheY, the response regulator of bacterial chemotaxis, *Nature 337*, 745-749.

[56] Morgan, B. A., Banks, G. R., Toone, W. M., Raitt, D., Kuge, S., and Johnston, L. H. (1997) The Skn7 response regulator controls gene expression in the oxidative stress response of the budding yeast *Saccharomyces cerevisiae*, *EMBO J. 16*, 1035-1044.

[57] Van Wuytswinkel, O., Reiser, V., Siderius, M., Kelders, M. C., Ammerer, G., Ruis, H., and Mager, W. H. (2000) Response of *Saccharomyces cerevisiae* to severe osmotic stress: evidence for a novel activation mechanism of the HOG MAP kinase pathway, *Mol. Microbiol. 37*, 382-397.

[58] Shang, Y., Chen, P., Lu, Y., and Wang, C. (2015) MrSkn7 controls sporulation, cell wall integrity, autolysis, and virulence in *Metarhizium robertsii*, *Euk. Cell 14*, 396-405.

[59] Stock, A., Koshland, D. E., Jr., and Stock, J. (1985) Homologies between the *Salmonella typhimurium* CheY protein and proteins involved in the regulation of chemotaxis, membrane protein synthesis, and sporulation, *PNAS 82*, 7989-7993.

[60] Sun, Y.-C., Koumoutsi, A., and Darby, C. (2009) The response regulator PhoP negatively regulates *Yersinia pseudotuberculosis* and *Yersinia pestis* biofilms, *FEMS Microbiol. Lett. 290*, 85-90.

[61] Aravind, L., Anantharaman, V., Balaji, S., Babu, M. M., and Iyer, L. M. (2005) The many faces of the helix-turn-helix domain: transcription regulation and beyond, *FEMS Microbiol Rev 29*, 231-262.

[62] Galperin, M. Y. (2010) Diversity of structure and function of response regulator output domains, *Curr Opin Microbiol 13*, 150-159.

[63] Lukat, G. S., Stock, A. M., and Stock, J. B. (1990) Divalent metal ion binding to the CheY protein and its significance to phosphotransfer in bacterial chemotaxis, *Biochemistry 29*, 5436-5442.

[64] Lukat, G. S., Lee, B. H., Mottonen, J. M., Stock, A. M., and Stock, J. B. (1991) Roles of the highly conserved aspartate and lysine residues in the response regulator of bacterial chemotaxis, *J. Biol. Chem. 266*, 8348-8354.

[65] Appleby, J. L., and Bourret, R. B. (1998) Proposed signal transduction role for conserved CheY residue Thr87, a member of the response regulator active-site quintet, *J. Bacteriol. 180*, 3563-3569.

[66] Trajtenberg, F., Albanesi, D., Ruetalo, N., Botti, H., Mechaly, A. E., Nieves, M., Aguilar, P. S., Cybulski, L., Larrieux, N., de Mendoza, D., and Buschiazzo, A. (2014) Allosteric activation of bacterial response regulators: the role of the cognate histidine kinase beyond phosphorylation, *mBio 5*, e01205.

[67] O'Connor, T. J., and Nodwell, J. R. (2005) Pivotal roles for the receiver domain in the mechanism of action of the response regulator RamR of *Streptomyces coelicolor*, *J. Mol. Biol. 351*, 1030-1047.

[68] Stock, A. M., Martinez-Hackert, E., Rasmussen, B. F., West, A. H., Stock, J. B., Ringe, D., and Petsko, G. A. (1993) Structure of the Mg^{2+}-bound form of CheY and mechanism of phosphoryl transfer in bacterial chemotaxis, *Biochemistry 32*, 13375-13380.

[69] Lee, S.-Y., Cho, H. S., Pelton, J. G., Yan, D., Berry, E. A., and Wemmer, D. E. (2001) Crystal structure of activated CheY, *J. Biol. Chem. 276*, 16425-16431.

[70] McCleary, W. R. a. S., J.B. (1994) Acetyl phosphate and the activation of two-component response regulators, *J. Biol. Chem. 269*, 31567-31572.

[71] Da Re, S. S., Deville-Bonne, D., Tolstykh, T., Véron, M., and Stock, J. B. (1999) Kinetics of CheY phosphorylation by small molecule phosphodonors, *FEBS Lett. 457*, 323-326.

[72] Herschlag, D., and Jencks, W. P. (1990) The effects of Mg^{2+}, hydrogen bonding, and steric factors on rate and equilibrium constants for phosphoryl transfer between carboxylate ions and pyridines, *J. Am. Chem. Soc. 112*, 1942-1950.

[73] Pazy, Y., Wollish, A. C., Thomas, S. A., Miller, P. J., Collins, E. J., Bourret, R. B., and Silversmith, R. E. (2009) Matching biochemical reaction kinetics to the timescales of life: structural determinants that influence the autodephosphorylation rate of response regulator proteins, *J Mol Biol 392*, 1205-1220.

[74] Mildvan, A. S. (1997) Mechanisms of signaling and related enzymes, *Proteins: Struct., Funct., Bioinf. 29*, 401-416.

[75] Lassila, J. K., Zalatan, J. G., and Herschlag, D. (2011) Biological phosphoryl-transfer reactions: Understanding mechanism and catalysis, *Annu. Rev. Biochem. 80*, 669-702.

[76] Stock, A. M., and Guhaniyogi, J. (2006) A new perspective on response regulator activation, *J. Bacteriol. 188*, 7328-7330.

[77] Silversmith, R. E., Appleby, J. L., and Bourret, R. B. (1997) Catalytic mechanism of phosphorylation and dephosphorylation of CheY: Kinetic characterization of imidazole phosphates as phosphodonors and the role of acid catalysis, *Biochemistry 36*, 14965-14974.

[78] Varughese, K. I., Tsigelny, I., and Zhao, H. (2006) The crystal structure of beryllofluoride Spo0F in complex with the phosphotransferase Spo0B represents a phosphotransfer pretransition state, *J. Bacteriol. 188*, 4970-4977.

[79] Zhao, X., Copeland, D. M., Soares, A. S., and West, A. H. (2008) Crystal structure of a complex between the phosphorelay protein YPD1 and the response regulator domain of SLN1 bound to a phosphoryl analog, *J. Mol. Biol. 375*, 1141-1151.

[80] Hinnebusch, A. G., and Johnston, M. (2011) YeastBook: An Encyclopedia of the Reference Eukaryotic Cell, *Genetics 189*, 683-684.

[81] Shor, E., and Chauhan, N. (2015) A case for two-component signaling systems as antifungal drug targets, *PLOS Pathog. 11*, e1004632.

[82] Maeda, T., Wurgler-Murphy, S. M., and Saito, H. (1994) A two-component system that regulates an osmosensing MAP kinase cascade in yeast, *Nature 369*, 242-245.

[83] Ota, I. M., and Varshavsky, A. (1993) A yeast protein similar to bacterial two-component regulators, *Science 262*, 566-569.

[84] Levin, D. E. (2011) Regulation of cell wall biogenesis in *Saccharomyces cerevisiae*: the cell wall integrity signaling pathway, *Genetics 189*, 1145-1175.

[85] He, X.-J., Mulford, K. E., and Fassler, J. S. (2009) Oxidative stress function of the *Saccharomyces cerevisiae* Skn7 receiver domain, *Euk. Cell 8*, 768-778.

[86] Posas, F., Wurgler-Murphy, S. M., Maeda, T., Witten, E. A., Thai, T. C., and Saito, H. (1996) Yeast HOG1 MAP kinase cascade is regulated by a multistep phosphorelay mechanism in the SLN1-YPD1-SSK1 "two-component" osmosensor, *Cell 86*, 865-875.

[87] Lu, J. M.-Y., Deschenes, R. J., and Fassler, J. S. (2003) *Saccharomyces cerevisiae* histidine phosphotransferase Ypd1p shuttles between the nucleus and cytoplasm for *SLN1*-dependent phosphorylation of Ssk1p and Skn7p, *Euk. Cell 2*, 1304-1314.

[88] Saito, H., and Posas, F. (2012) Response to hyperosmotic stress, *Genetics 192*, 289-318.

[89] Li, S., Ault, A., Malone, C. L., Raitt, D., Dean, S., Johnston, L. H., Deschenes, R. J., and Fassler, J. S. (1998) The yeast histidine protein kinase, Sln1p, mediates phosphotransfer to two response regulators, Ssk1p and Skn7p, *EMBO J. 17*, 6952-6962.

[90] Ketela, T., Brown, J. L., Stewart, R. C., and Bussey, H. (1998) Yeast Skn7p activity is modulated by the Sln1p-Ypd1p osmosensor and contributes to regulation of the HOG1 pathway, *Mol. Gen. Genet. 259*, 372-378.

[91] Porter, S. W., and West, A. H. (2005) A common docking site for response regulators on the yeast phosphorelay protein YPD1, *Biochim. Biophys. Acta 1748*, 138-145.

[92] Janiak-Spens, F., Cook, P. F., and West, A. H. (2005) Kinetic analysis of YPD1-dependent phosphotransfer reactions in the yeast osmoregulatory phosphorelay system, *Biochemistry 44*, 377-386.

[93] Attwood, P. V., Piggott, M. J., Zu, X. L., and Besant, P. G. (2007) Focus on phosphohistidine, *Amino Acids 32*, 145-156.

[94] Attwood, P. V., Besant, P. G., and Piggott, M. (2011) Focus on phosphoaspartate and phosphoglutamate, *Amino Acids 40*, 1035-1051.

[95] Xu, Q., Porter, S. W., and West, A. H. (2003) The yeast YPD1/SLN1 complex: Insights into molecular recognition in two-component systems, *Structure 11*, 1569-1581.

[96] Chooback, L., and West, A. H. (2003) Co-crystallization of the yeast phosphorelay protein YPD1 with the SLN1 response regulator domain and preliminary X-ray diffraction analysis, *Acta Cryst. D59*, 927-929.

[97] Horie, T., Tatebayashi, K., Yamada, R., and Saito, H. (2008) Phosphorylated Ssk1 prevents unphosphorylated Ssk1 from activating the Ssk2 MAP kinase kinase kinase in the yeast HOG osmoregulatory pathway, *Mol. Cell. Biol. 28*, 5172-5183.

[98] Sato, N., Kawahara, H., Toh-e, A., and Maeda, T. (2003) Phosphorelay-regulated degradation of the yeast Ssk1p response regulator by the ubiquitin-proteosome system, *Mol. Cell. Biol. 23*, 6662-6671.

[99] Janiak-Spens, F., Sparling, D. P., and West, A. H. (2000) Novel role for an HPt domain in stabilizing the phosphorylated state of a response regulator domain, *J. Bacteriol. 182*, 6673-6678.

[100] Janiak-Spens, F., Sparling, J. M., Gurfinkel, M., and West, A. H. (1999) Differential stabilities of phosphorylated response regulator domains reflect functional roles of the yeast osmoregulatory SLN1 and SSK1 proteins, *J. Bacteriol. 181*, 411-417.

[101] Kaserer, A. O., Andi, B., Cook, P. F., and West, A. H. (2009) Effects of osmolytes on the SLN1-YPD1-SSK1 phosphorelay system from *Saccharomyces cerevisiae*, *Biochemistry 48*, 8044-8050.

[102] Porter, S. W., Xu, Q., and West, A. H. (2003) Ssk1p response regulator binding surface on histidine-containing phosphotransfer protein Ypd1p, *Euk. Cell 2*, 27-33.

Chapter 2: Co-crystallization of an Ssk1-R2 point mutant (W638A) in complex with Ypd1

Introduction

Structural information for Ypd1 and a complex with its upstream phospho-donor, Sln1-R1, has significantly contributed to the knowledge of expanded phosphorelay systems and how they function in eukaryotic systems[1-4]. Structural characterization of Ypd1 interfacing with its other cognate partners has been sought for many years. This chapter details the methods that were used to obtain a co-crystal structure between Ypd1 and the receiver domain of its downstream cognate partner, Ssk1-R2^{W638A}.

Expression and purification of Ssk1-R2-W638A

Before structural information was available, the functional significance of Ssk1 amino acid residues was inferred using predicted structural homology models. Non-conservative mutations were introduced at sites in Ssk1-R2 that were predicted to interact with Ypd1 in order to gain insight into their biological functions. The discovery of a beneficial point mutation in the receiver domain of Ssk1 led to notable purification improvements over the WT protein. Mutating tryptophan 638 to alanine (W638A) resulted in a 15-fold increase in protein yield per gram of wet cell mass (Figure 8 (pg. 32)). This point mutation also greatly increased the solubility of the Ssk1 receiver domain. In previous attempts, Ssk1-R2 could only be concentrated to ~2 mg/mL before precipitating. The W638A mutation allowed the protein to be concentrated up to >16 mg/mL, greatly increasing the likelihood of producing protein crystals.

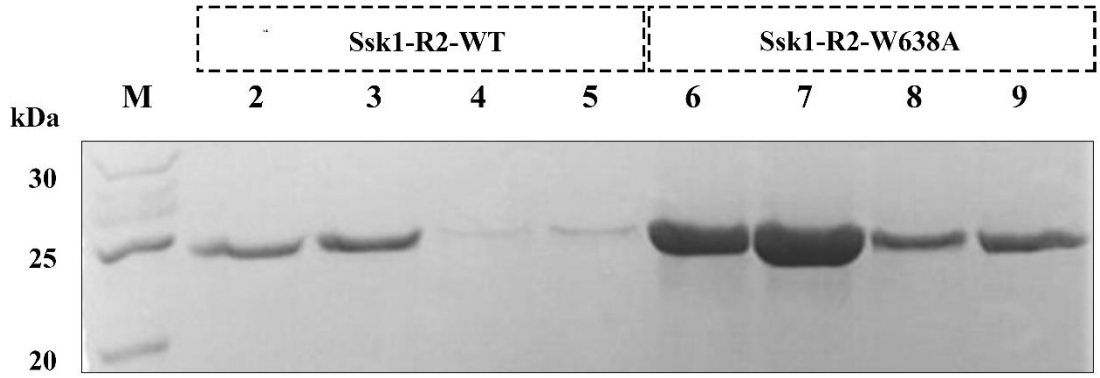

Figure 8. Ssk1-R2-WT vs. Ssk1-R2-W638A yield.
15% Coomassie-stained SDS PAGE gel showing the increase in protein yield afforded by the W638A mutation from 2 L cultures. Lane M: marker, lanes 2-4: 1 mL elutions from chitin columns of Ssk1-R2-WT, lanes 6-9: 1 mL elutions from chitin columns of Ssk1-R2-W638A.

Co-crystallization of Ypd1 in complex with Ssk1-R2-W638A

The increase in yield and solubility of Ssk1-R2-W638A led to the successful co-crystallization of Ypd1 and Ssk1-R2-W638A. Ypd1 and Ssk1-R2-W638A were expressed and purified from *E. coli*, mixed in equimolar amounts and co-concentrated in 20 mM HEPES pH 7.0, 100 mM NaCl, 50 mM $MgCl_2$ and 1 mM β-mercaptoethanol (βME). The initial promising crystal lead came from well A5 of the MCSG-II 96-well screen at the University of Oklahoma Macromolecular Crystallography Laboratory (MCL). The proteins were set up in 24-well vapor diffusion hanging-drop trays around the neutral phosphate conditions of well A5 (MCSG-II). The wells were clearly overnucleated and the crystals were very small (Figure 9 (pg. 33)).

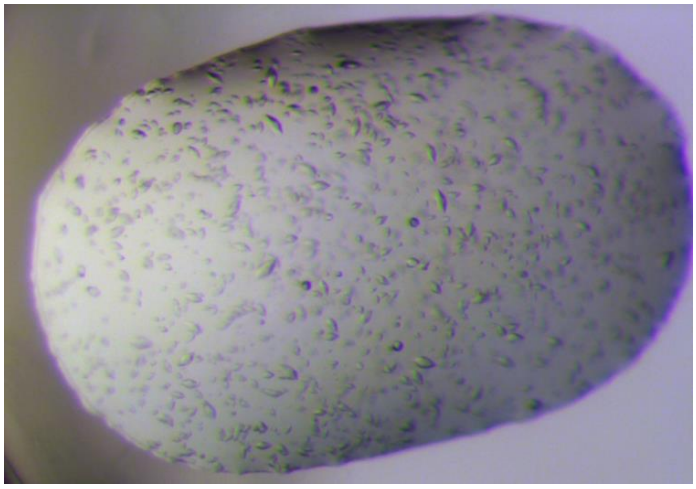

Figure 9. Initial co-crystals of Ypd1 and Ssk1-R2-W638A.
The crystals were overnucleated and very small, indicating the need for optimization.

Next, the proteins were mixed in equimolar amounts and co-concentrated in 50 mM Tris pH 8.0, 100 mM NaCl and 1% glycerol. This buffer change, determined by Dr. Smita Menon, resulted in crystals that reached 100-200 μm in diameter. A single crystal was rinsed, dissolved in 1X Laemmli buffer and applied to sodium dodecyl sulfate polyacrylamide gel electrophoresis (SDS-PAGE) to verify the presence of both proteins in the crystal (Figure 10).

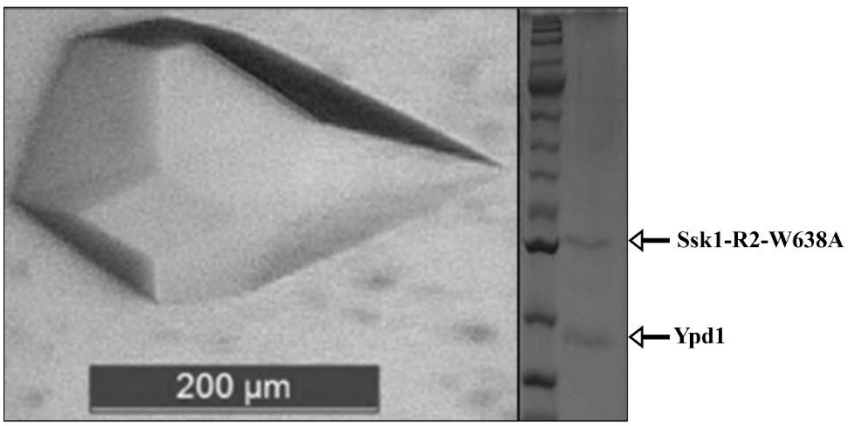

Figure 10. Photograph of Ssk1-R2^{W638A}/Ypd1 crystal.
Photograph of Ssk1-R2^{W638A}/Ypd1 crystal (left panel) and Coomassie-stained 15% SDS-PAGE gel of a dissolved crystal, verifying that the crystals were composed of both proteins (right panel, optimized crystal and gel courtesy of Dr. Smita Menon).

In order to obtain independent phasing information, a selenomethionine derivative of Ssk1-R2-W638A (Ssk1-R2$^{W638A}_{SeMet}$) was co-crystallized with Ypd1 under similar conditions (Figure 11). Data from these crystals were used to solve the final crystal structure.

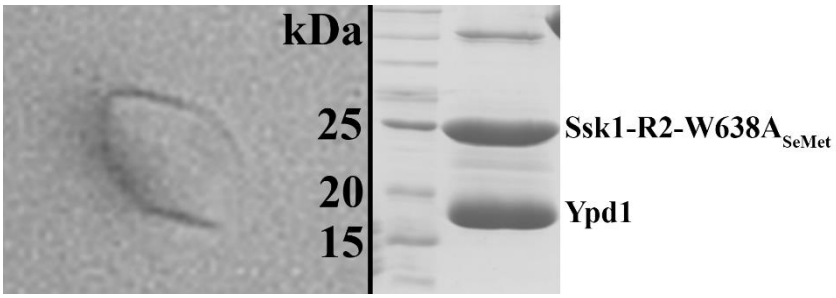

Figure 11. Photograph of a Ypd1/Ssk1-R2$^{W638A}_{SeMet}$ crystal.
Photograph of Ssk1-R2$^{W638A}_{SeMet}$/Ypd1 crystal (left panel) and Coomassie-stained 15% SDS-PAGE gel of the co-concentrated proteins that were used to set up 24-well crystal trays (right panel).

Co-crystal structure of Ssk1-R2^{W638A}/Ypd1

The Ssk1-R2 ^{W638A}/Ypd1 complex is the first structure of a eukaryotic HPt protein in complex with a downstream response regulator receiver domain (Figure 12 (pg. 35)). The crystal structure reveals that Ssk1-R2 adopts the canonical response regulator domain $(\beta\alpha)_5$ topology[5]. The conserved site of phosphorylation on Ssk1 (D554) is located on the C-terminal end of β3, positioned 6.3 Å away from H64, the site of phosphorylation on Ypd1. This co-crystal structure represents the unphosphorylated "inactive" state. The orientations of switch residues T610 from β4 and Y629 from β5 are consistent with previously determined inactive structures; both are oriented "away" from the active site[3, 6-9].

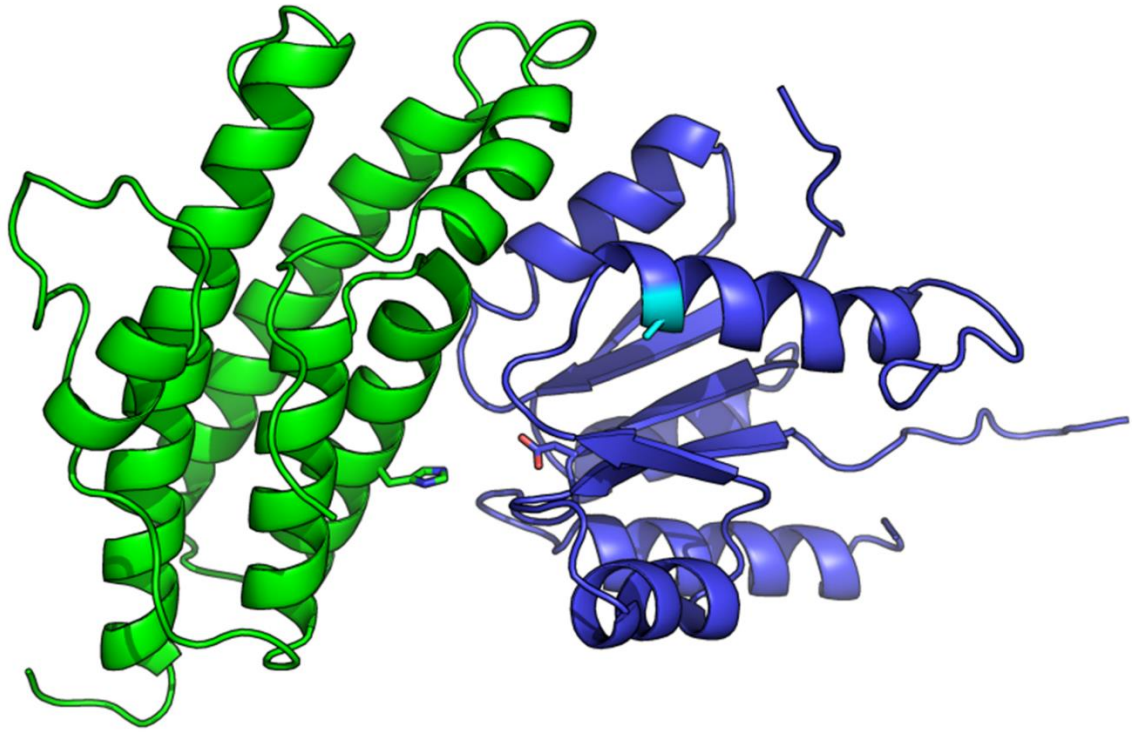

Figure 12. Ribbon representation of the complex between Ypd1 and Ssk1-R2^{W638A}. *S. cerevisiae* Ypd1 (green) has a four-helix bundle core; the active site histidine (H64) is shown in stick. The Ssk1^{W638A} receiver domain (blue) adopts the canonical response regulator $(\beta\alpha)_5$ fold; the active site aspartate (D554) is shown in stick and the mutation site (W638A) is shown in cyan.

Discussion

Based on the co-crystal complex of Ssk1-R2^{W638A}/Ypd1, point mutants on Ssk1-R2 at the interface with Ypd1 were created and biochemically characterized with respect to binding affinity and phosphotransfer. These data and a thorough comparison with the published structures of Ypd1 and Sln1-R1[4, 10] support a detailed biochemical explanation for the physiological function of Ssk1. These topics will be discussed in extensive detail in Chapters 3 and 4.

Experimental Section

Construction of mutants

The Ssk1-R2-W638A mutant was created by QuikChange mutagenesis (see Appendix A) from the wild-type plasmid in the hybrid pET11a/pCYB2 vector.

Protein Purification

S. cerevisiae Ypd1 was purified from *E. coli* DH5α cells as a tag-less, full length, 167-residue protein[1]. Ypd1 was constitutively expressed from a pUC19 plasmid (New England Biolabs (NEB)) for 19 hours at 37 °C, 200 rpm. Cells were lysed by French Press in lysis buffer (100 mM sodium phosphate, pH 7.0, 1 mM EDTA, and 1 mM βME) and the lysate was clarified by centrifugation for 1 hour at ~25,000 x g, 4 °C. Saturated ammonium sulfate was slowly added to the supernatant up to 55% by volume and stirred slowly at 4 °C for 30 minutes. After centrifugation, the supernatant was discarded and the pellet was resuspended in dialysis buffer (20 mM BisTris pH 6.5, 1 mM βME). Dialysis into 2 L of buffer was performed twice to remove ammonium sulfate. Protein was recovered and centrifuged to remove any debris and then filtered through a 0.45 µm syringe filter. This sample was added to a 5 mL HiTrap Q anion exchange column (GE Healthcare) on an AKTA prime chromatography system and run in 20 mM BisTris pH 6.5 with increasing concentrations of NaCl (0-1 M). Ypd1 fractions were pooled, concentrated, filtered and added to a Sephadex® G-50 or Sephacryl® S-100 column in 20 mM Tris pH 8.0, 100 mM NaCl and 1% glycerol.

Ssk1-R2-WT and Ssk1-R2-W638A were expressed in *E. coli* BL21 Star or Gold cells (Appendix B). Two 1 L flasks of Luria Broth (LB) + ampicillin (100 µg/mL) were inoculated with 10 mL saturated cultures and grown at 37 °C, 200 rpm until OD_{600} >

0.8. The temperature was changed to 16 °C and cultures were induced with 1 mM isopropyl β-D-1-thiogalactopyranoside (IPTG) and grown for approximately 22 hours. Cell pellets were kept for no longer than 24 hours at -20 °C before lysis. Cells were lysed with French Press or an Emulsiflex (Avestin) and the lysate was clarified by centrifugation at ~25,000 x g for 1 hour at 4 °C. Proteins were purified using chitin affinity chromatography (IMPACT system, NEB) as follows. The cell lysate supernatant was added to a 3-4 mL chitin column pre-equilibrated in lysis buffer (20 mM Tris pH 8.0, 500 mM NaCl, 1 mM EDTA, 10% glycerol and 0.1% Triton X-100). The flow-through (FT) was discarded and the column was washed with 10 column volumes (CV) of lysis buffer and 10 CV of cleavage buffer (20 mM Tris pH 8.0, 100 or 500 mM NaCl, 10% glycerol). The column was left to incubate overnight in cleavage buffer + 30 mM βME at 4 °C. Cleaved protein was eluted with chelexed cleavage buffer (20 mM Tris pH 8.0, 500 mM NaCl, 10% glycerol) and flash-frozen until ready for size-exclusion chromatography (Sephadex G®-75, Sephacryl® S-100 or S-200) in 20 mM Tris pH 8, 100 mM NaCl and 1% glycerol.

Crystallization and data collection

Equimolar amounts of Ssk1-R2-W638A and Ypd1 were combined, co-concentrated to 15 mg/mL and set up at room temperature in 96-well broad screens (Index, PACT, Wizard, CSHT, MCSG I-IV, and JCSG) in the MCL. An initial promising lead came from well A5 of MCSG-II: 0.2 M lithium sulfate, 0.1 M CAPS/NaOH pH 10.5, 1.2 M NaH_2PO_4/0.8 M K_2HPO_4. Fine 24-well vapor diffusion hanging drop screens were set up around these conditions. Proteins were co-concentrated in 20 mM HEPES pH 7.0, 100 mM NaCl, 50 mM $MgCl_2$ and 1 mM βME.

The wells were clearly overnucleated and the crystals were very small. To produce large, diffraction-quality crystals, the co-concentration buffer was changed to 50 mM Tris pH 8.0, 100 mM NaCl and 1% glycerol by Dr. Smita Menon. These conditions produced crystals approximately 100-200 μm in diameter that diffracted to 3.0 Å at the MCL at the University of Oklahoma (Rigaku 007HF Micromax generator with Cu Kα line and a Dectris Pilatus 200K detector). To collect independent phasing information, a heavy atom derivative was created. Selenomethionine was introduced into the Ssk1-R2-W638A protein and it was co-crystallized with Ypd1. Crystals were grown in 24-well vapor diffusion hanging-drop trays under the following conditions: 2-7 mg/mL concentrated protein in 20 mM Tris pH 8.0, 100 mM NaCl, and 1% glycerol (1:1 with well solution). The best crystals were produced under the following well conditions: 0.1 M CAPS pH 10.5, 1.0-1.2 M NaH_2PO_4, 0.1-0.2 M $LiSO_4$, 0.8 M K_2HPO_4. Dr. Smita Menon used 1.2 M NaH_2PO_4, 0.8 M K_2HPO_4, 0.2 M $LiSO_4$, 0.1 M CAPS pH 10.5, and 9% glycerol as the final cryo conditions for the co-crystals of Ypd1 and Ssk1-$R2^{W638A}$. A multiple wavelength anomalous diffraction (MAD) data set was collected at the Stanford Synchrotron Radiation Lightsource (SSRL) on beam line 11-1.

Structure determination and refinement

The structure of the Ssk1-$R2^{W638A}$ response regulator receiver domain in complex with histidine phosphotransfer protein Ypd1 was solved by Dr. Smita Menon using phasing information obtained from MAD data and the program PHENIX-1.9-1692[11]. After calculation of the initial electron density map, the initial crystallographic R-factor was 29.8% with an R_{free} of 36.3%. After several rounds of refinement using phenix.refine[12], the R-factor dropped to 23.17% with an R_{free} of 27.66%. The final

model was refined to a resolution of 2.80 Å (Table 3). Structure figures were generated using PyMOL[13] or Chimera[14].

Table 3. X-ray data collection and refinement statistics

A. *Data collection*	**Se-peak**	**Se-remote**	**Se-edge**
Wavelength (Å)	0.97910	0.9116	0.97930
Temperature (K)	100	100	100
Resolution (Å)	2.80	2.80	2.80
Unique reflections	125302	124523	124773
Redundancy	10.4	10.3	10.4
Completeness (%)	99.8 (99.5)	99.8 (100.00)	99.8 (99.7)
Mean I/σ (I)	43 (3.25)	40.6 (2.75)	42.7 (3.5)
R_{merge} (%)	0.065 (0.71)	0.062 (0.79)	0.065 (0.81)
B. *Crystal parameters*			
Space group	$P4_32_12$	$P4_32_12$	$P4_32_12$
Unit cell dimensions (Å)	71.69, 71.69, 176.38	71.73, 71.73, 176.47	71.74, 71.74, 176.51
Matthews' coefficient ($Å^3$/Da)	2.51		
Solvent content (%)	51.00		
C. *Refinement*			
Resolution range (Å)	33.27-2.80		
Number of protein atoms	2484		
Average B-factors ($Å^2$)	42.19		
R-factor (%)	23.17		
R_{free} (%)	27.66		
rmsd bond lengths (Å)	0.003		
rmsd bond angles (°)	0.572		
Ramachandran plot (%)			
Most favored region	94.65		
Additionally allowed region	5.02		
Disallowed region	0.33		
Clash score	3.42		

References

[1] Xu, Q., Nguyen, V., and West, A. H. (1999) Purification, crystallization, and preliminary X-ray diffraction analysis of the yeast phosphorelay protein YPD1, *Acta Cryst. D55*, 291-293.

[2] Xu, Q., and West, A. H. (1999) Conservation of structure and function among histidine-containing phosphotransfer (HPt) domains as revealed by the crystal structure of YPD1, *J. Mol. Biol. 292*, 1039-1050.

[3] Xu, Q., Porter, S. W., and West, A. H. (2003) The yeast YPD1/SLN1 complex: Insights into molecular recognition in two-component systems, *Structure 11*, 1569-1581.

[4] Zhao, X., Copeland, D. M., Soares, A. S., and West, A. H. (2008) Crystal structure of a complex between the phosphorelay protein YPD1 and the response regulator domain of SLN1 bound to a phosphoryl analog, *J. Mol. Biol. 375*, 1141-1151.

[5] Bourret, R. B. (2010) Receiver domain structure and function in response regulator proteins, *Curr. Opin. Microbiol. 13*, 142-149.

[6] Riepl, H., Scharf, B., Schmitt, R., Kalbitzer, H. R., and Maurer, T. (2004) Solution structures of the inactive and BeF_3-activated response regulator CheY2, *J. Mol. Biol. 338*, 287-297.

[7] Guhaniyogi, J., Robinson, V. L., and Stock, A. M. (2006) Crystal structures of beryllium fluoride-free and beryllium fluoride-bound CheY in complex with the conserved C-terminal peptide of CheZ reveal dual binding modes specific to CheY conformation, *J. Mol. Biol. 359*, 624-645.

[8] Bachhawat, P., and Stock, A. M. (2007) Crystal structures of the receiver domain of the response regulator PhoP from *Escherichia coli* in the absence and presence of the phosphoryl analog beryllofluoride, *J. Bacteriol. 189*, 5987-5995.

[9] Leonard, P. G., Golemi-Kotra, D., and Stock, A. M. (2013) Phosphorylation-dependent conformational changes and domain rearrangements in *Staphylococcus* aureus VraR activation, *Proc. Natl. Acad. Sci. (USA) 110*, 8525-8530.

[10] Chooback, L., and West, A. H. (2003) Co-crystallization of the yeast phosphorelay protein YPD1 with the SLN1 response regulator domain and preliminary X-ray diffraction analysis, *Acta Cryst. D59*, 927-929.

[11] Adams, P. D., Afonine, P. V., Bunkoczi, G., Chen, V. B., Davis, I. W., Echols, N., Headd, J. J., Hung, L.-W., Kapral, G. J., Grosse-Kunstleve, R. W., McCoy, A. J., Moriarty, N. W., Oeffner, R., Read, R. J., Richardson, D. C., Richardson, J. S., Terwilliger, T. C., and Zwart, P. H. (2010) PHENIX: a comprehensive Python-based system for macromolecular structure solution, *Acta Cryst. D66*, 213-221.

[12] Afonine, P. V., Grosse-Kunstleve, R. W., Echols, N., Headd, J. J., Moriarty, N. W., Mustyakimov, M., Terwilliger, T. C., Urzhumtsev, A., Zwart, P. H., and Adams, P. D. (2012) Towards automated crystallographic structure refinement with phenix.refine, *Acta Cryst. D 68*, 352-367.

[13] Schrödinger, L. (2010) The {PyMOL} Molecular Graphics System, Version~1.3.

[14] Pettersen, E. F., Goddard Td Fau - Huang, C. C., Huang Cc Fau - Couch, G. S., Couch Gs Fau - Greenblatt, D. M., Greenblatt Dm Fau - Meng, E. C., Meng Ec Fau - Ferrin, T. E., and Ferrin, T. E. UCSF Chimera--a visualization system for exploratory research and analysis.

Chapter 3: Biochemical characterization of Ssk1 point mutants

Introduction

To ensure that a crystal complex between Ssk1-R2-W638A with Ypd1 was physiologically relevant, functional properties of the W638A mutant were compared to WT Ssk1-R2. Phosphotransfer was investigated from Ypd1 *in vitro*; phosphorylated lifetimes of Ssk1-R2~P in the presence and absence of Ypd1 were also tested. Protein-protein interaction affinities were measured with a fluorescence binding assay. In almost every case Ssk1-R2-W638A behaved as WT. Three notable anomalies were found. In the fluorescence binding assay, the Ssk1-R2-W638A reversed the signal of Ypd1-T12C~F compared to WT (Figure 15 (pg. 45)). A minor amount of the reverse phosphotransfer reaction from Ssk1-R2-W638A to Ypd1 was observed *in vitro* (Figure 19 (pg. 49)). This reaction was not previously observed from WT Ssk1-R2~P to Ypd1 under similar conditions. Additionally, the phosphorylated lifetime of Ssk1-R2-W638A was extended 3-fold in the presence of Ypd1-H64Q (Figure 25 (pg. 53)).

A structurally-guided investigation of mutations of other potentially important amino acid residues on Ssk1-R2 was carried out using the same methods of fluorescence binding and phosphotransfer assays. Residues at the active site (Ssk1-R2-Q556 and S612) were mutated to alanine to investigate the phospho-stabilization effect of Ypd1 on Ssk1-R2. Residues that formed ionic interactions with Ypd1 in the Ssk1-$R2^{W638A}$/Ypd1 complex (absent from the Sln1-R1/Ypd1 complex; Ssk1-R2-R524, K525 and H637) were mutated to alanine and evaluated in order to understand their contribution to binding affinity with Ypd1. A description of the point mutants used as negative controls (Ssk1-D554N and I518S) along with point mutants that did not affect

Ssk1-R2/Ypd1 activity (Ssk1-R2-T631A, N635A and L636S) are also discussed. Point mutants that are not presented in Ypd1 activity assays are given honorable mention (Ssk1-R2-D554A, V634S, L639S, E645Q, W646A, G647Q, and Q650L).

Ssk1-R2-W638A retains wild type-like activity

Affinity for Ypd1

An *in vitro* fluorescence binding assay was used to measure relative affinities for Ypd1 and Ssk1-R2 and Ssk1-R2-W638A (For location of W638A, see Figure 12 (pg. 35)). A threonine at the edge of the Ypd1 hydrophobic binding patch was selected for the site of fluorescent labeling so that a binding event would be detected without interference (Figure 13 (pg. 44)). Threonine 12 was mutated to cysteine (West lab, unpublished data) to make it amenable to chemical coupling with a fluorescent label (5-iodoacetamidofluorescein (5-IAF), Figure 14 (pg. 44)). Titrations of Ssk1-R2 and Ssk1-R2-W638A caused a change in the fluorescence signal produced by 5-IAF-labeled Ypd1-T12C in a concentration-dependent manner (Figure 15 (pg. 45), Figure 30 (pg. 57)). Calculation of dissociation constants revealed a minor but insignificant change in affinity between Ypd1 and Ssk1-R2-W638A ($\Delta\Delta G_{binding}$ = 0.93 kcal/mol).

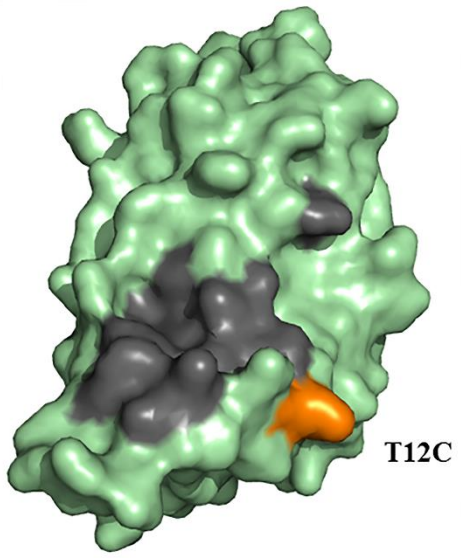

Figure 13. Molecular surface of Ypd1 showing the location of the T12C mutation.
The mutation (shown in orange) at the periphery of the hydrophobic RR-binding patch[1, 2] (shown in charcoal).

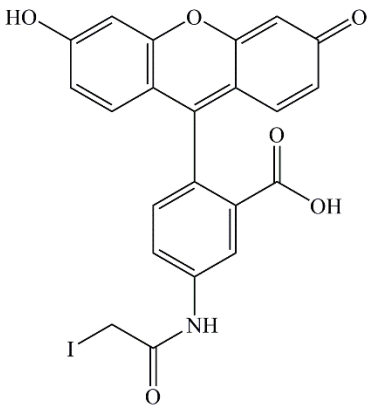

Figure 14. Chemical structure of 5-iodoacetamidofluorescein (5-IAF).
Chemical conjugation takes place due to a nucleophilic substitution of the iodine by a reduced thiol group on Ypd1 cysteine 12.

Binding curves were successfully fitted using a quadratic equation (Equation 1) to obtain dissociation constants. However, the direction of the fluorescence signal was reversed in experiments using Ssk1-R2-W638A compared to WT. The intrinsic fluorescence of Ssk1-R2 tryptophan (excitation at 280 nm and emission at 348 nm), in addition to π-π stacking, could influence the chemical environment of the 5-IAF

fluorophore causing a signal reversal. Although the fluorescence signals are in opposite directions, only the magnitude of the change along with initial slope of the binding curve were used to determine binding affinity. The dissociation constants with Ypd1-T12C~F were calculated to be (25.1 ± 2.4) ± 1.3 nM for Ssk1-R2 (*N*=4) and (122.5± 15.0) ± 36.7 nM for Ssk1-R2-W638A (*N*=3). To verify that analysis was independent of signal direction, data points were artificially flipped across the x-axis, and curve fitting produced identical results. The observed $\Delta\Delta G_{binding}$ between Ssk1-R2-WT and Ssk1-R2-W638A was calculated to be 0.93 kcal/mol (Equation 2). Although a slightly reduced affinity was seen for Ypd1-T12-C~F with Ssk1-R2-W638A, the difference in K_d values was considered insignificant[3].

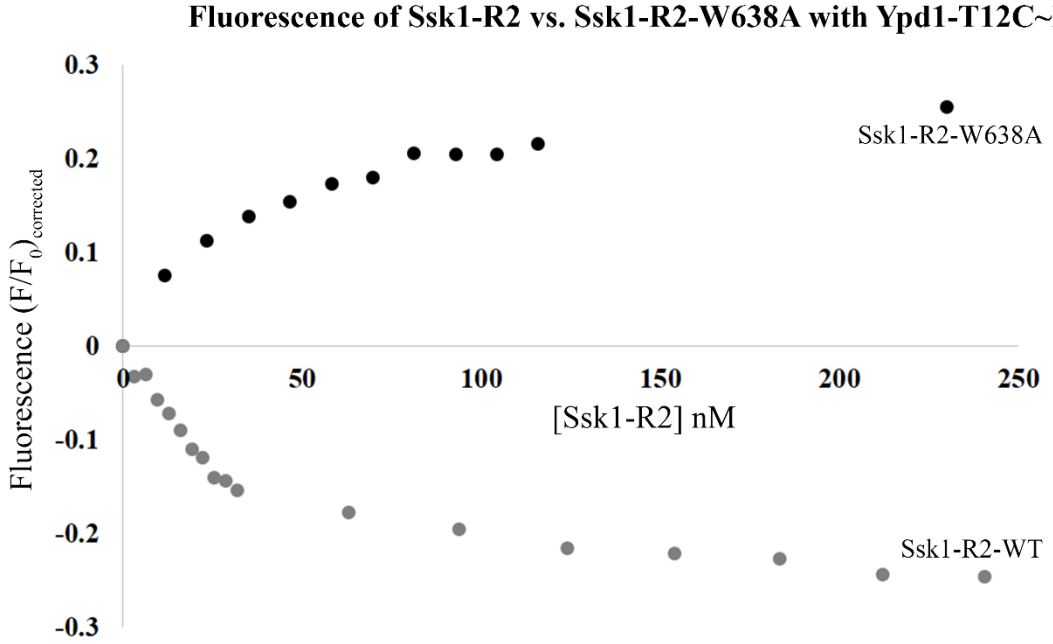

Figure 15. Ssk1-R2-WT vs. Ssk1-R2-W638A fluorescence binding curves.
Ssk1-R2 titration into Ypd1-T12C~F produces fluorescence quenching, while titration of Ssk1-R2-W638A produces fluorescence enhancement. Single experimental curves are shown as examples.

Addition of Ssk1-R2 to Ypd1-T12C~F caused a quenching in the fluorescence signal, while addition of Ssk1-R2-W638A caused an enhancement (Figure 15). This

change is likely due to the physical location of amino acid 638 on Ssk1-R2 relative to the site of fluoresceination on Ypd1. W638 of Ssk1-R2 is in close proximity to the site of fluoresceination on Ypd1-T12C. When tryptophan is modeled into the crystal structure in position 638 of Ssk1 to resemble Ssk1-R2-WT and cysteine is modeled in at residue 12 on Ypd1, the interatomic distance is approximately 9.3 Å (Figure 16). Upon attachment of 5-IAF (~11 Å from end to end) to the cysteine, this gap would be bridged, allowing potential π-π stacking to occur during the WT interaction. This could account for the quenching of the fluorescence signal upon the binding event. The absence of the tryptophan ring in Ssk1-R2-W638A would remove any π-π stacking, resulting in a different chemical environment around the fluorescein. This could explain the enhanced fluorescence observed upon Ssk1-R2-W638A binding to Ypd1-T12C~F.

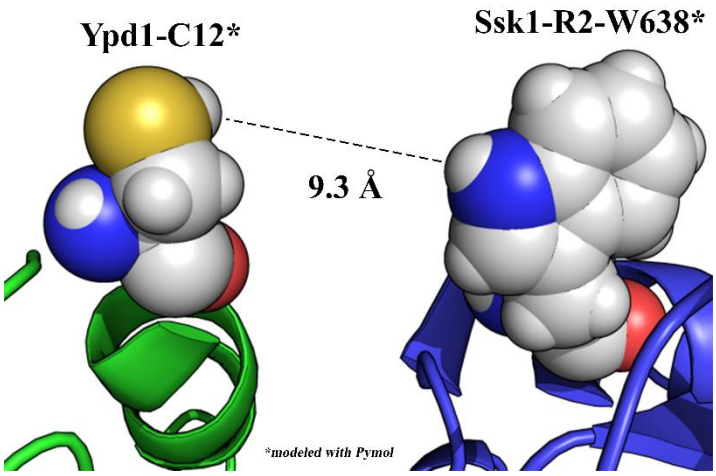

Figure 16. Modeled distance between Ypd1-T12C and W638 in Ssk1-R2^{W638A}.
This figure shows Ypd1-T12C and W638 of Ssk1-R2 modeled in PyMol[4]. The length of 5-IAF is ~11 Å from end to end. When attached to Ypd1-T12C, 5-IAF could be in close enough proximity to W638 of Ssk1-R2 to allow π-π stacking. (Mutations modeled on to Ssk1-R2^{W638A}/Ypd1 co-crystal structure).

Phosphotransfer activity with Ypd1

Phosphotransfer from Ypd1~P to Ssk1-R2 reaches steady-state levels within seconds[5]. In order to compare phosphotransfer efficiency between Ypd1 and Ssk1-R2-

W638A, *in vitro* phosphotransfer experiments were performed. The phosphotransfer efficiency for the Ssk1-R2-W638A mutant was comparable to WT (Figure 17 (pg. 47), Figure 31 (pg. 57)).

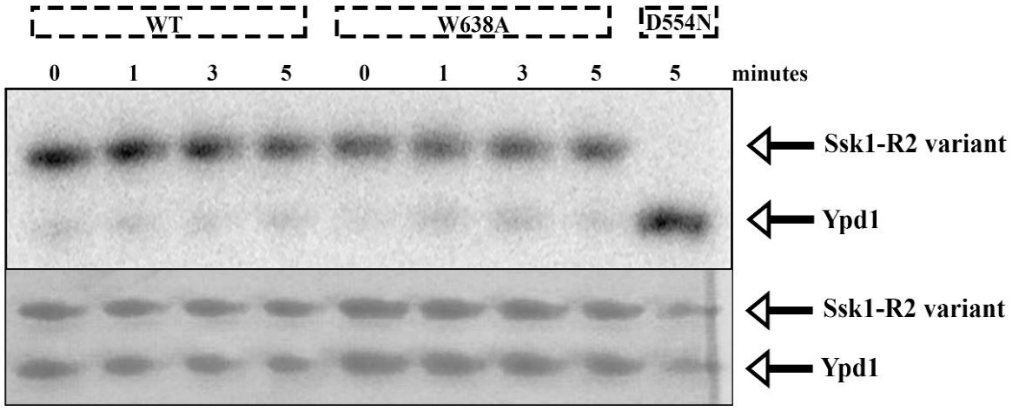

Figure 17. Phosphotransfer from Ypd1~P to Ssk1-R2 variants.
Top panel shows phosphorimage of Ypd1~P phosphoryl transfer to Ssk1-R2 and Ssk1-R2-W638A within seconds that remained at a steady-state level after 5 minutes. The negative control, unphosphorylatable mutant (Ssk1-R2-D554N), shows that the radiolabel remained on Ypd1. Bottom panel shows protein load on 15% Coomassie-stained gel.

In order to compare the phospho-stability of Ssk1-R2-W638A~P to WT, ^{32}P-labeled Ssk1 variants were monitored over time in the presence or absence of Ypd1. The phosphorylated half-lives of Ssk1-R2 and Ssk1-R2-W638A were determined to be 23.6 ± 2.3 min and 22.1 ± 3.1 min, respectively (Figure 18 (pg. 48)). Previously, the *in vitro* phosphorylated half-life of Ssk1-R2 was determined to be ~13 min[6]. Differences in experimental image processing could account for the slight variation in phosphorylated half-life observed in this case compared to published data. For example, previously published phorphorimages were obtained using autoradiography with an x-ray screen and current phosphorimages were obtained using a phosphor screen and a Typhoon (GE Healthcare) imager. In addition, current images of radiolabeled bands were accurately quantified using ImageJ software. When

phosphorylated Ssk1-R2-W638A was paired with Ypd1 using current methods, its half-life was extended to ~ 40 hours (data not shown), comparable to the half-life of WT Ssk1-R2 in the presence of Ypd1 (using autoradiography)[6].

In conclusion, Ssk1-R2-W638A showed near-like WT activity with respect to affinity with Ypd1, phosphotransfer from Ypd1 and autodephosphorylation activity.

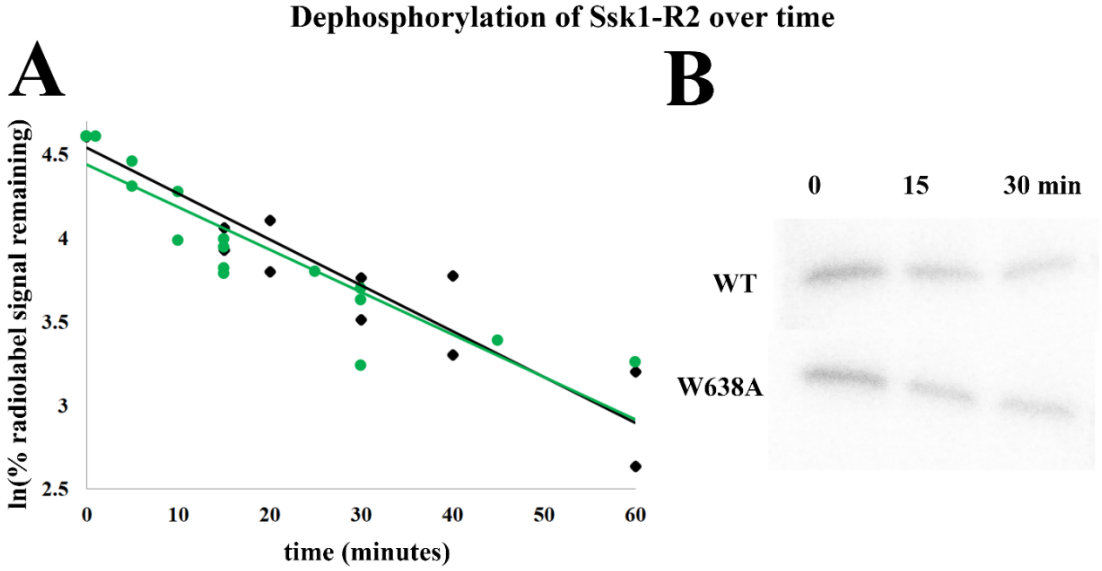

Figure 18. Phosphorylated half-lives of Ssk1-R2 and Ssk1-R2-W638A.
Panel A shows all data points for phosphorylated half-life experiments for Ssk1-R2~P (black) and Ssk1-R2-W638A~P (green) (experiments were done in quadruplicate). Panel B is an example phosphorimage that shows the autodephosphorylation for Ssk1-R2~P and Ssk1-R2-W638A~P over 30 minutes. Calculated phosphorylated half-lives of 23.6 ± 2.3 min (Ssk1-R2) and 22.1 ± 3.1 min (Ssk1-R2-W638A) show that the autodephosphorylation reactions of the two proteins are similar.

Although Ssk1-R2-W638A~P was stabilized by Ypd1 in a comparable manner to WT Ssk1-R2, the reverse phosphotransfer reaction was observed (Figure 19 (pg. 49)). This back-transfer has not been observed with WT Ssk1-R2[7] (Figure 23 (pg. 51)). In these experiments, back-transfer was detected by the appearance of a phosphorylated band corresponding to Ypd1, indicating that phosphotransfer from Ssk1-R2-W638A~P to Ypd1 had occurred.

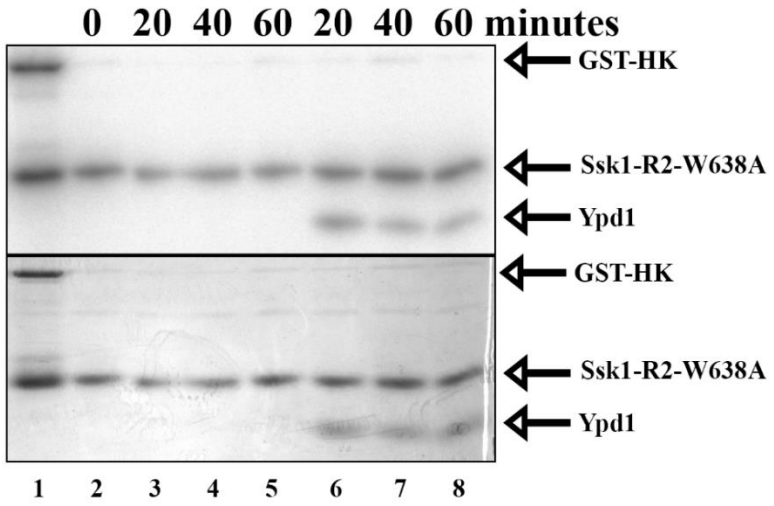

Figure 19. Phosphorimage of Ssk1-R2-W638A~P reverse phosphotransfer to Ypd1.
Top panel shows phosphorimage and bottom panel shows protein load on a 15% Coomassie-stained gel. Lane 1: GST-HK~P + Ssk1-R2-W638A, Lanes 2-5: Ssk1-R2-W638A~P, Lanes 6-8: Ssk1-R2-W638A~P + Ypd1. Appearance of Ypd1~P bands in lanes 6-8 indicate phosphotransfer from Ssk1-R2-W638A to Ypd1.

Ssk1-R2 active site mutants and phosphotransfer with Ypd1

Protein purification

Ssk1-R2 mutants were purified using the same protocol as WT Ssk1-R2 as described in Chapter 2. Some mutants were subjected to an additional size-exclusion purification step (Figure 20). Chitin column purifications of Ssk1-R2-Q556A and Ssk1-R2-S612A are similar to WT (data not shown).

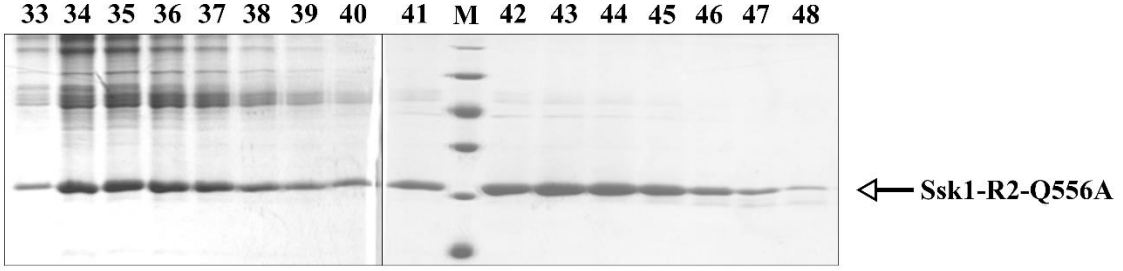

Figure 20. Ssk1-R2-Q556A Sephadex®-G75purification.
Fractions 33-48 from a 100 mL gravity-flow gel filtration column showing a final purification step of Ssk1-R2-Q556A. Gel shows a typical Ssk1-R2 protein yield of 1.5 mg/L.

Phosphotransfer activity with Ypd1

To examine the activity of two residues that have been implicated in RR autodephosphorylation rates[8-11], two point mutants were made: Ssk1-R2-Q556A ("D+2") and Ssk1-R2-S612A ("T+2"). Ssk1-R2-Q556 is located *n*+2 residues away from the phosphorylatable aspartate and Ssk1-R2-S612 is located *n*+2 residues away from the conserved switch threonine residue in the active site (Figure 21).

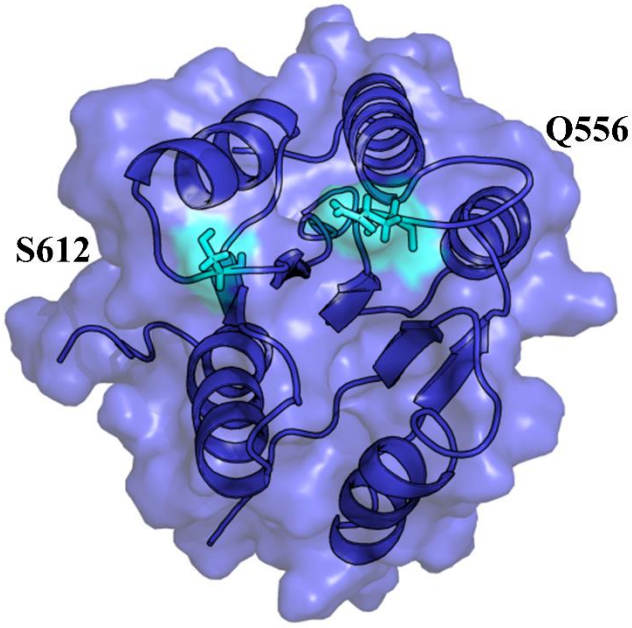

Figure 21. Illustration of the location of Ssk1-R2 active site point mutants.
Surface and ribbon representation showing Ssk1-R2^{W638A} (blue) mutation sites (cyan stick), Q556 ("D+2") and S612 ("T+2") are shown.

Phosphorylated half-lives were tested in the absence and presence of Ypd1. Reverse phosphotransfer from Ssk1-R2-Q556A~P to Ypd1 (Figure 22 (pg. 51)) was observed as in Ssk1-R2-W638A~P to Ypd1. Reverse phosphotransfer from Ssk1-R2-S612A~P was not observed as in WT (Figure 23 (pg. 51)).

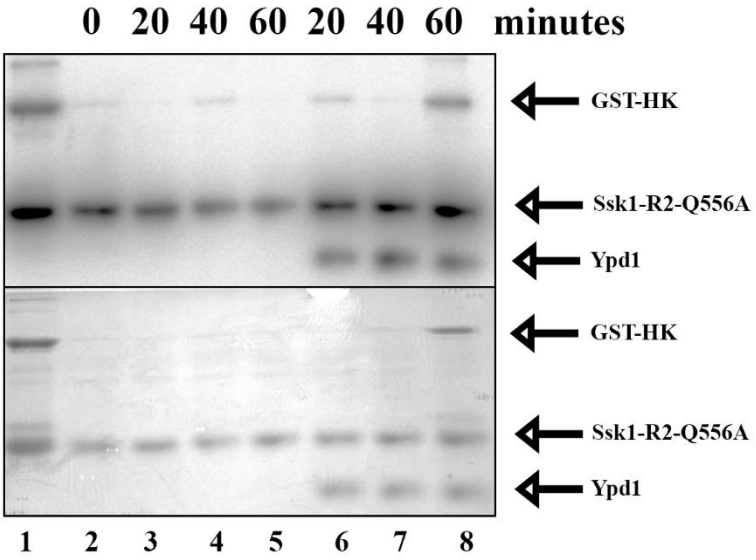

Figure 22. Phosphorimage of Ssk1-R2-Q556A~P reverse phosphotransfer to Ypd1.

Top panel shows phosphorimage and bottom panel shows protein load on a 15% Coomassie-stained gel. Lane 1: GST-HK~P + Ssk1-R2-Q556A, Lanes 2-5: Ssk1-R2-Q556A~P, Lanes 6-8: Ssk1-R2-Q556A~P + Ypd1. Appearance of Ypd1~P bands in lanes 6-8 indicate phosphotransfer from Ssk1-R2-Q556A to Ypd1.

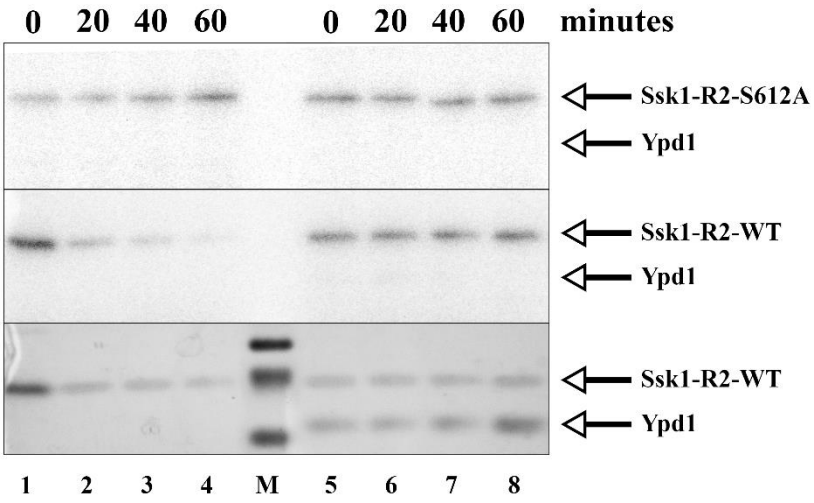

Figure 23. Phosphorimages of Ssk1-R2-S612A and WT Ssk1-R2.

The top panel shows a phosphorimage of Ssk1-R2-S612A~P without Ypd1 (lanes 1-4) and with Ypd1 (lanes 5-8) over 1 hour. The middle panel shows a phosphorimage of WT Ssk1-R2~P without Ypd1 (lanes 1-4) and with Ypd1 (lanes 5-8) over 1 hour. The bottom panel shows protein load of WT Ssk1-R2 on a 15% Coomassie-stained gel (protein load for Ssk1-R2-S612A not shown).

Figure 23 (pg. 51) shows that autodephosphorylation of Ssk1-R2-S612A does not proceed as WT, but remains stable over 1 hour (*N*=2). In contrast to Ssk1-R2-W638A and Q556A, back-transfer from Ssk1-R2-S612A to Ypd1 was not observed. The phosphorimage shows that WT Ssk1-R2 dephosphorylated over time when Ypd1 is absent, but was stabilized in the presence of Ypd1, and back-transfer to Ypd1 was not observed, corroborating published data[6, 7].

Autodephosphorylation of Ssk1-R2-Q556A was measured (Figure 24) and compared to Ssk1-R2 and Ssk1-R2-W638A. The calculated half-life was 23.7 ± 0.3 min (*N*=3), showing no signifiant difference from WT or Ssk1-R2-W638A.

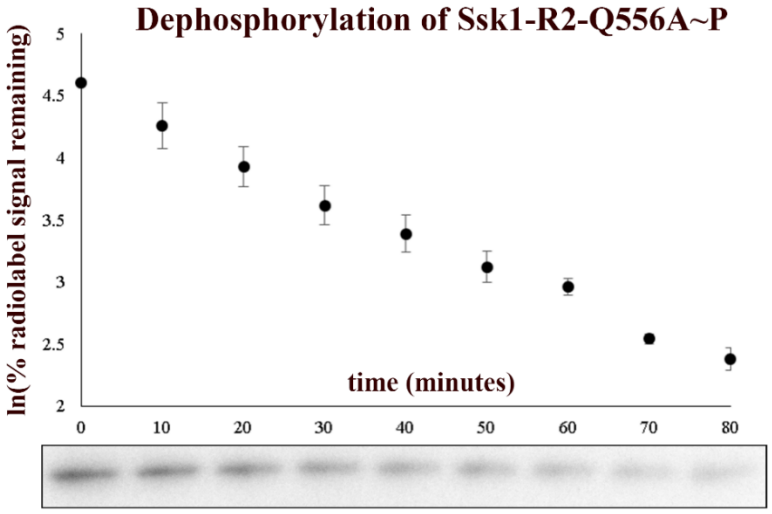

Figure 24. Dephosphorylation and half-life of Ssk1-R2-Q556A~P.
Top panel shows dephosphorylation of Ssk1-R2-Q556A over 80 min. Bottom panel is a phosphorimage of the gradual signal loss due to autodephosphorylation activity. The calculated phosphorylated half-life of Ssk1-R2-Q556A~P was 23.7 ± 0.3 min (*N*=3), compared to 23.6 ± 2.3 min (Ssk1-R2) and 22.1 ± 3.1 min (Ssk1-R2-W638A). Results show no significant difference in the autodephosphorylation activity of these three proteins.

Since Ssk1-R2-W638A~P and Ssk1-R2-Q556A~P were able to transfer a phosphoryl group to Ypd1, their stabilities were tested in the presence of Ypd1-H64Q, a non-phosphorylatable Ypd1 mutant that would prevent the reverse phosphotransfer reaction from occurring. Interestingly, the phosphorylated half-lives of both mutants

were extended >3-fold that of WT Ssk1-R2 in the presence of Ypd1-H64Q (Figure 25). When Ypd1-H64Q was paired with WT Ssk1-R2~P, the phosphorylated half-life was ~2 hours, corroborating published data[6], while the phosphorylated half-life of Ssk1-R2-W638A~P was extended to 6.1 ± 2.9 hours (*N*=2) and the phosphorylated half-life of Ssk1-R2-Q556A was extended to 6.5 ± 2.1 (*N*=2) hours (Figure 25).

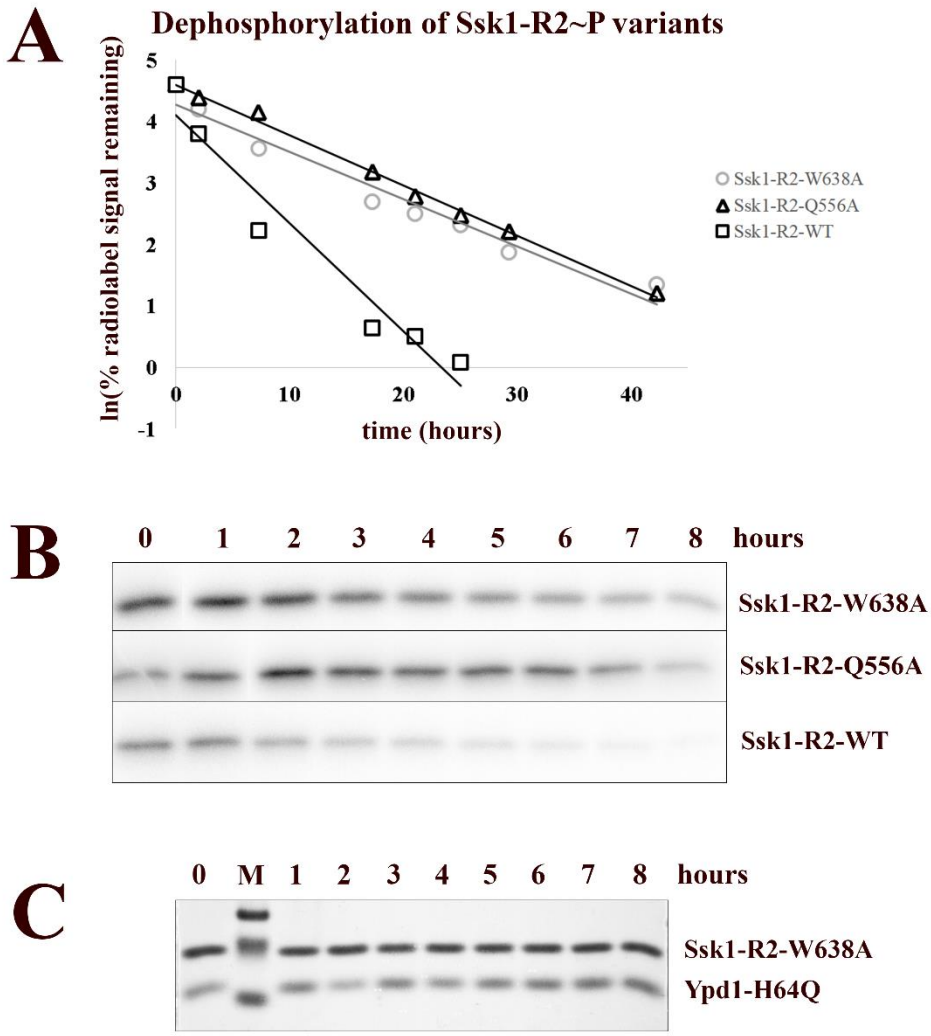

Figure 25. Half-lives of Ssk1-R2-Q556A~P and Ssk1-W638A~P with Ypd1-H64Q compared to WT Ssk1-R2.
A) The natural log of the percentage of remaining radiolabel on each Ssk1-R2 variant over ~25-45 hours. B) Phosphorimages of Ssk1-R2~P variants showing the decay of radiolabel over 8 hours (marker lanes have been removed for clarity). C) 15% Coomassie-stained gel showing protein load of the Ssk1-R2-W638A~P panel B experiment as an example (protein load of WT Ssk1-R2 and Ssk1-R2-Q556A not shown).

Negative control mutants of Ssk1-R2

Point mutants of Ssk1-R2 (Figure 26) were constructed to act as negative controls in phosphotransfer and fluorescence binding assays. The first mutants constructed were the unphosphorylatable mutants, Ssk1-R2-D554N and Ssk1-R2-D554A (C-terminal end of β3). Ssk1-R2-I518S (α1 helix), was made to disrupt the formation of the Ypd1/Ssk1-R2 complex by interfering with the hydrophobic docking site interaction. The reasons for choosing the I518 residue as a control mutant were 2-fold: before the co-crystal structure was solved, a sequence alignment indicated that I518 occupied the same position as V1102 in Sln1-R1, which is an essential hydrophobic interface contact with Ypd1[12]. This position was predicted to have the same significance in the Ssk1-R2/Ypd1 complex. Additionally, when I518 was mutated to a polar residue (threonine), Ypd1 association was disrupted *in vivo*[13].

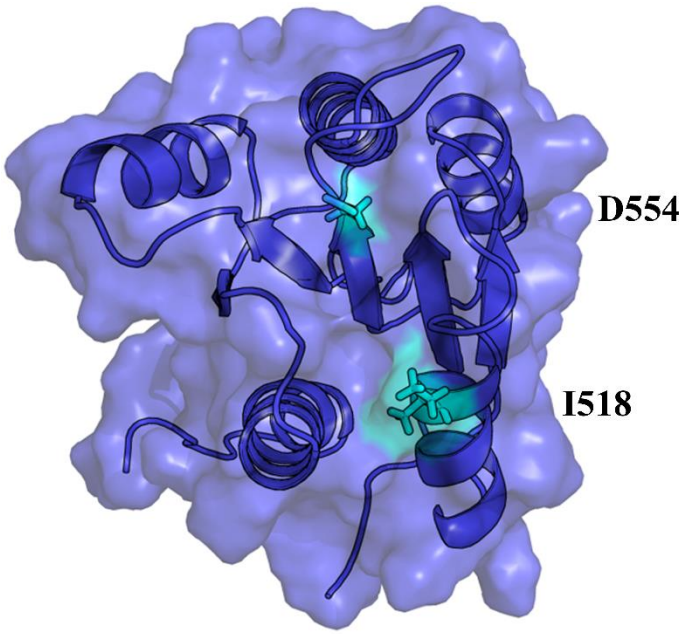

Figure 26. Illustration of the location of Ssk1-R2 negative control point mutants. Surface and ribbon representation showing Ssk1-R2^{W638A} (blue) mutation sites (cyan stick), D554 (phosphorylatable aspartate, β3) and I518 (essential hydrophobic contact point, α1) are shown.

Protein purification

Ssk1-R2-D554N (Figure 27), D554A (data not shown) and I518S (Figure 28) were purified using the same protocol as WT Ssk1-R2 as described in Chapter 2.

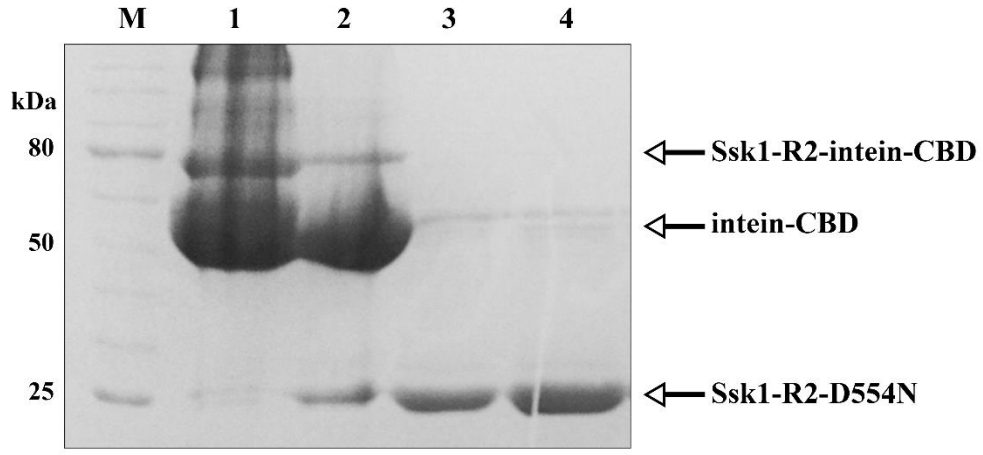

Figure 27. Chitin column purification of Ssk1-R2-D554N.
M- marker, 1- loaded chitin resin for Ssk1-R2-D554N, 2- chitin resin after βME incubation and elution of cleaved Ssk1-R2-D554N protein, 3-4- elutions of Ssk1-R2-D554N.

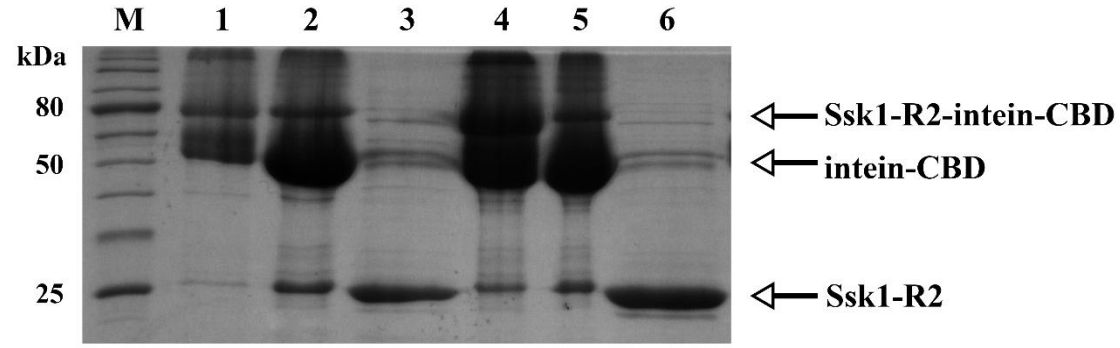

Figure 28. Chitin column purification of Ssk1-R2 and Ssk1-R2-I518S.
M- marker, 1- loaded chitin resin for Ssk1-R2-WT, 2- chitin resin after βME incubation and elution of cleaved Ssk1-R2-WT protein, 3- elution of Ssk1-R2-WT, 4- loaded chitin resin for Ssk1-R2-I518S, 5- chitin resin after βME incubation and elution of cleaved Ssk1-R2-I518S protein, 6- elution of Ssk1-R2-I518S. Gel illustrates that the purification of Ssk1-R2-I518S is similar to WT purification.

An alternative mutant (Ssk1-R2-V634S) was selected to disrupt the Ssk1-R2/Ypd1 binding interface based on an Sln1-R1 sequence alignment, but due to insolubility, purification attempts were abandoned (Figure 29 (pg. 56)).

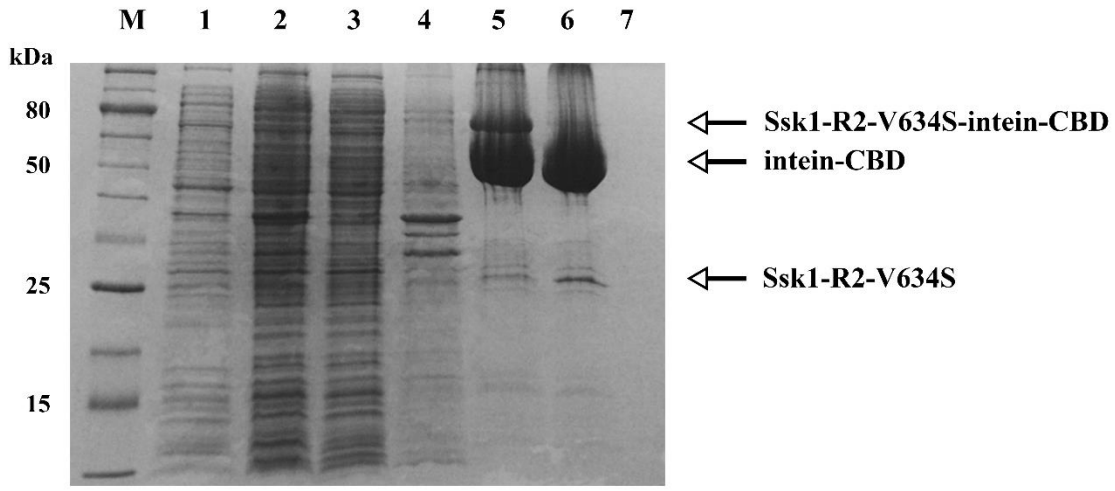

Figure 29. Purification of Ssk1-R2-V634S.
M- marker, 1- uninduced BL21-Star cells, 2- induced BL21-Star cells, 3- supernatant of whole cell lysate, 4- pellet of whole cell lysate, 5- loaded chitin resin, 6- chitin resin after βME incubation and elution of cleaved protein, 7- elution of Ssk1-R2-V634S. Gel illustrates that the Ssk1-R2-V634A mutant did not yield purified protein.

Binding affinity and phosphotransfer activity with Ypd1

The D554N mutant did not display significantly different affinity for Ypd1 in the fluorescence binding assay (Table 5 (pg. 63), Figure 30 (pg. 57)), but as expected, was unable to accept a phosphoryl group from Ypd1~P in a phosphotransfer assay (Figure 17 (pg. 47) and Figure 31 (pg. 57)).

The I518S mutation completely abolished Ypd1 binding in the fluorescence binding assay (Figure 30 (pg. 57)). It also demonstrated a greatly diminished ability to accept a phosphoryl group from Ypd1~P in a phosphotransfer assay (Figure 31 (pg. 57)).

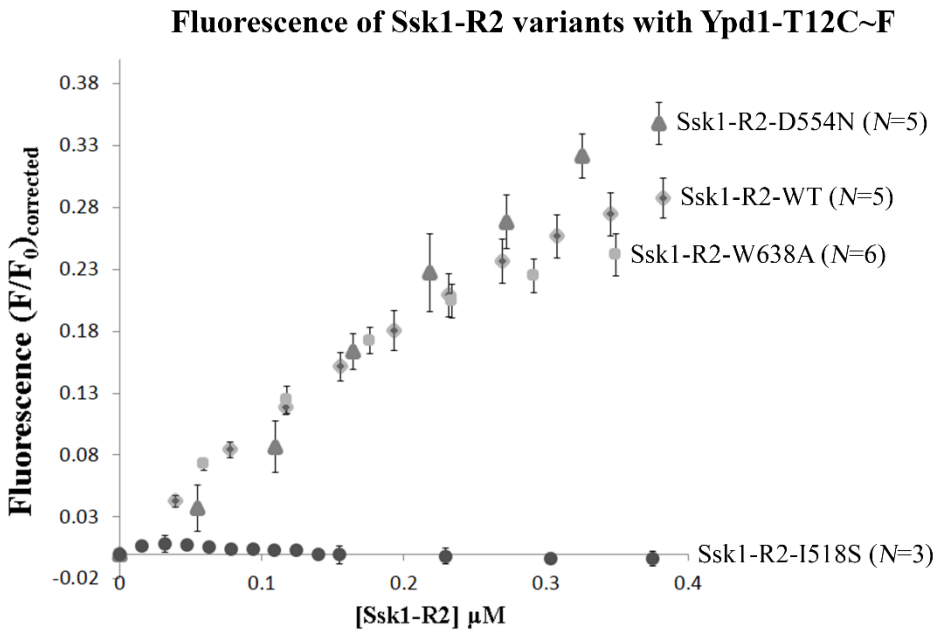

Figure 30. Initial portion of fluorescence binding curves.
Initial portions of equilibrium binding curves from Ssk1-R2, Ssk1-R2-W638A, Ssk1-D554N and Ssk1-I518S titrated in to 6 nM Ypd1-T12C~F. Curves for Ssk1-R2, Ssk1-R2-D554N and Ssk1-R2-I518S were mathematically adjusted to begin at the origin and have a positive slope in order to highlight the magnitude of fluorescence signal change. Ssk1-R2-W638A was not adjusted, as it naturally produced an enhanced fluorescence signal.

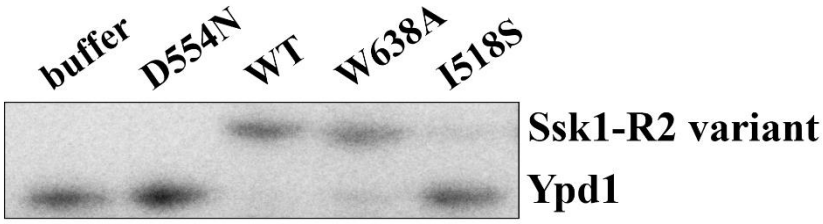

Figure 31. Phosphorimage of Ypd1~P phosphotransfer to Ssk1-R2 variants.
The image shows that Ypd1~P transfers a phosphoryl group to Ssk1-R2 (100%) and Ssk1-R2-W638A within seconds. Ssk1-R2-D554N is not able to accept a phosphoryl group and the phospho-accepting activity of Ssk1-R2-I518S is greatly diminished, with most of the radiolabel remaining on Ypd1.

Ssk1-R2-I518S was able to accept a phosphoryl group from an artificial upstream donor, the HK domain from Sln1 (Figure 32 (pg. 58)). Although the transfer was not efficient and most of the radiolabel remains on HK, the transfer ability indicates

that Ssk1-R2-I518S is able to be phosphorylated in a limited manner, suggesting that it retains proper tertiary structure.

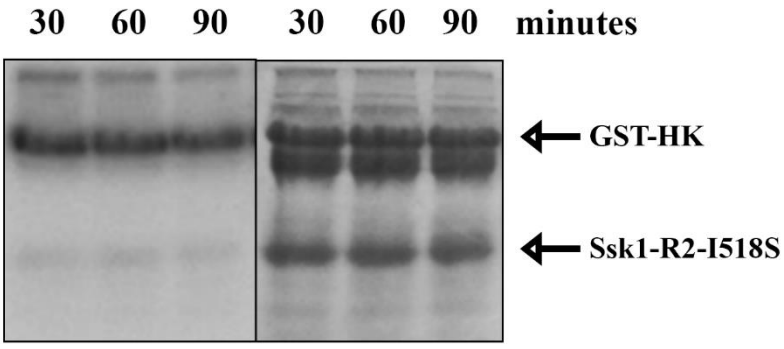

Figure 32. Ssk1-R2-I518S is able to accept a phosphoryl group from GST-HK~P. Left panel shows phosphorimage of Ssk1-R2-I518S accepting a phosphoryl group from GST-HK~P. Right panel shows protein load on a15% Coomassie-stained gel.

Abolishment of salt bridge formation affects binding affinity

Due to the physiological role of the Ssk1/Ypd1 interaction as part of the osmotic stress response[6, 14] and *in vitro* reaction to osmolyte concentrations[15], electrostatic interactions were examined as a possible explanation for the functional differences of Sln1-R1/Ypd1 and Ssk1-R2/Ypd1. Interface analysis was performed on the co-crystal structure of Ssk1-R2^{W638A}/Ypd1 and revealed two additional intermolecular salt bridges (Ssk1-R2-R524/Ypd1-D24 and Ssk1-R2-K525/Ypd1-D23) and one possible ionic interaction (Ssk1-R2-H637/Ypd1-E16) when compared to the Sln1-R1/Ypd1 co-crystal complex (Figure 33 (pg. 59)).

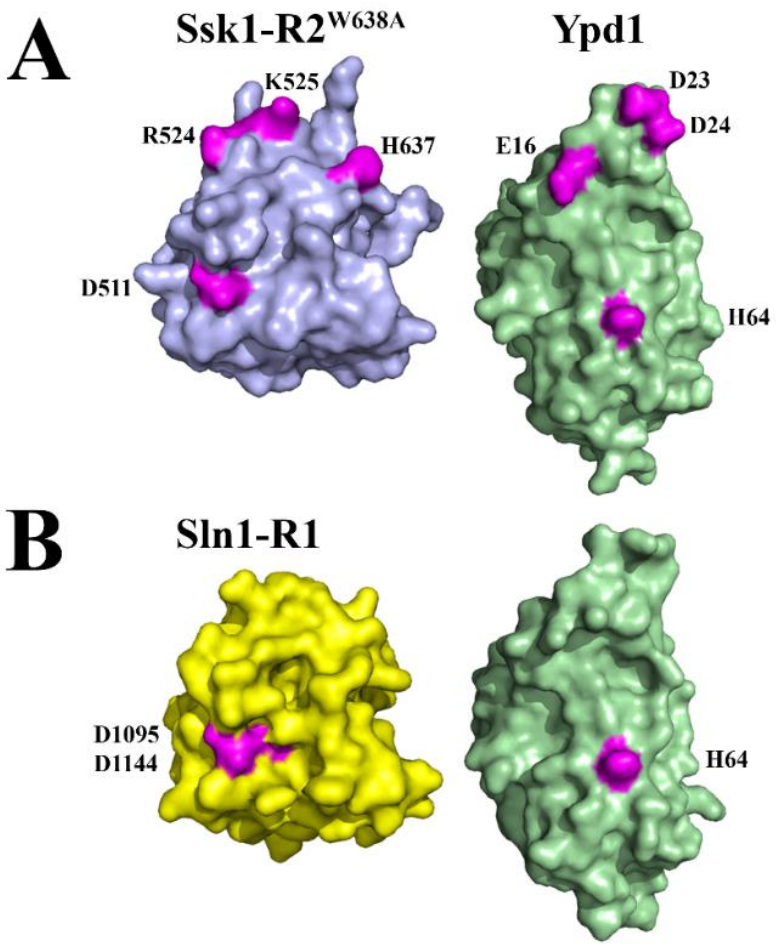

Figure 33. Molecular surfaces illustrating salt bridge locations of Sln1-R1 and Ssk1-R2^{W638A} and Ypd1.

Complexes have been pulled apart and rotated 90° in order to directly view interfaces. A) Ssk1-R2^{W638A} (blue) and Ypd1 (green). B) Sln1-R1 (yellow) and Ypd1 (green) (PDB ID: 1OXB). Observed salt bridge interactions are shown in magenta. Sln1-R1/Ypd1 interface contains one double salt bridge at the active site while the Ssk1-R2^{W638A}/Ypd1 interface contains ionic interaction patches surrounding the hydrophobic docking site.

Protein purification

Ssk1-R2-R524A, K525A and H637A were purified using the same protocol as WT Ssk1-R2 as described in Chapter 2 (Figure 34 (pg. 60)).

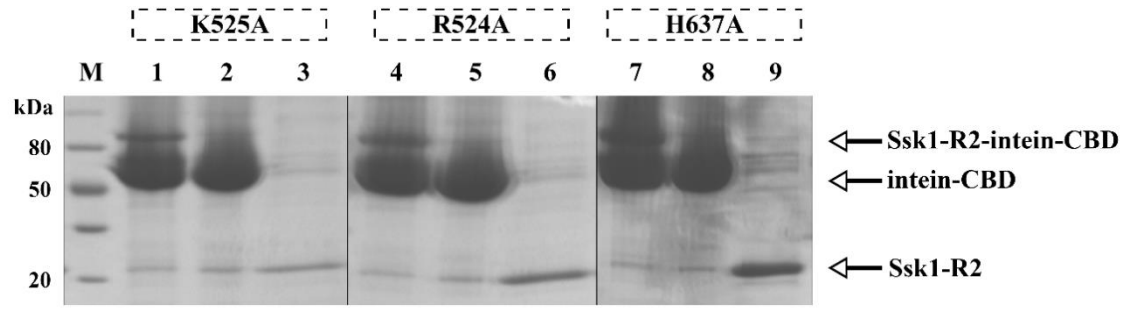

Figure 34. Chitin column purification gels of Ssk1-R2-R524A, Ssk1-R2-K525A and Ssk1-R2-H637A.
M- marker; Lanes 1, 4, 7- loaded chitin resin; Lanes 2, 5, 8- chitin resin after βME incubation and elution of cleaved Ssk1-R2-WT protein; Lanes 3, 6, 9- protein elution.

Binding affinity between Ssk1-R2 salt bridge mutants and Ypd1

Ssk1-R2 point mutations were constructed to abolish the unique ionic interactions at the Ssk1-R2/Ypd1 interface. Ssk1-R2-R524, K525 and H637 were mutated to alanine and tested in the fluorescence binding assay with Ypd1-T12C~F. Binding to Ypd1 was significantly reduced with R524A and K525A and insignificantly reduced with H637A[3] (Figure 35, Table 4 (pg. 61)). At the concentrations tested, Ssk1-R2-R524 and Ssk1-R2-K525 produced linear curves, indicating that binding with Ypd1-T12C~F was not saturated. Without a hyperbolic binding curve, accurate dissociation constants could not be calculated. From examination of preliminary data, dissociation constants for both mutants are > 0.5 μM. In addition, a double mutant (Ssk1-R2-R524A/H637A) showed a markedly decreased affinity for Ypd1-T12C~F (data not shown).

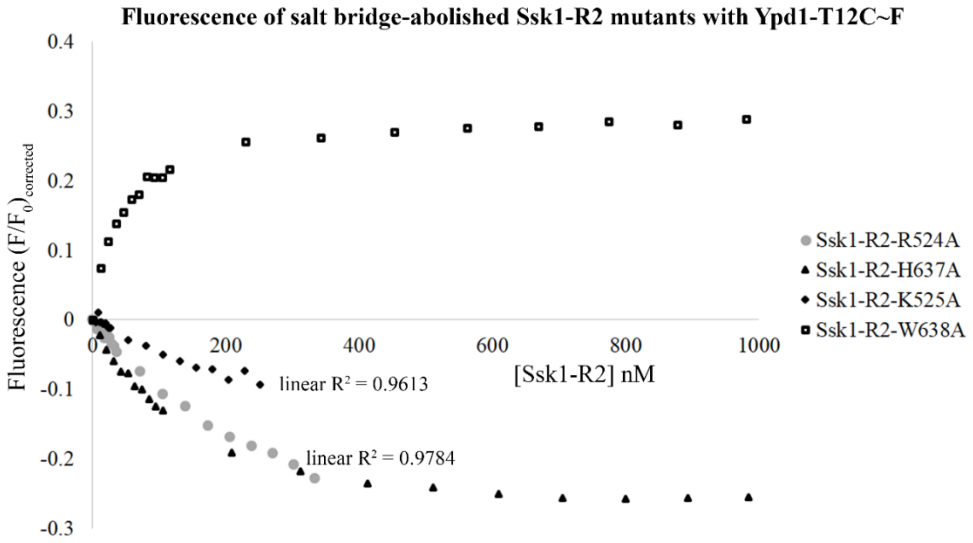

Figure 35. Fluorescence binding assay of Ssk1-R2 mutants with Ypd1-T12C~F.
Hyperbolic binding curves indicate strong binding (low nanomolar K_d) while linear binding curves (Ssk1-R2-R524A and Ssk1-R2-K525A) signify that K_ds are so high that they cannot be calculated because binding saturation has not been reached. A dissociation constant was calculated only for Ssk1-R2-H637A. (Ssk1-R2-W638A is shown as a positive control.) These results illustrate the reduced binding affinity with Ypd1 by mutating basic residues R524 and K525 on Ssk1-R2 to alanine.

Table 4. Dissociation constants of Ssk1-R2 salt bridge point mutants.
Entropic contributions were assumed constant when calculating observed $\Delta\Delta G_{binding}$ for each mutant.

Ssk1-R2 variant	Observed K_d with Ypd1-T12C~F (K_d ± mean error) ± standard error of mean	Observed $\Delta\Delta G_{binding}$ (kcal/mol)
WT	**(25.1 ± 2.4) ± 1.3 nM**	**0**
R524A	N/D	n/a
K525A	N/D	n/a
H637A	(129.6 ± 4.9) nM	0.97

Although mutating salt bridge residues on Ssk1-R2 disrupted affinity for Ypd1 in the fluorescence binding assay, they did not abolish phosphotransfer to Ssk1-R2, nor did they shift the preference of Ypd1 to phosphorylate Ssk1-R2 over Skn7-R3 (Figure

36). Qualitatively, there was more radiolabel present after 5 minutes on all Ssk1-R2 variants than on Skn7-R3 (approximate equimolar load, data not shown).

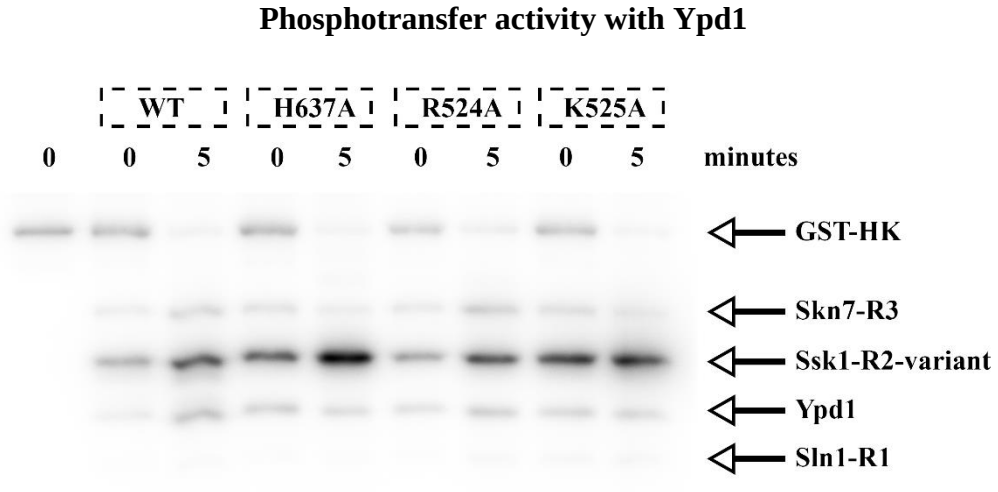

Figure 36. Ypd1~P phosphotransfer to Ssk1-R2 variants vs. WT Skn7-R3.
Phosphorimage shows phosphorelay through the entire Sln1 pathway. Sln1-HK → Sln1-R1 → Ypd1 → Ssk1-R2 or Skn7-R3.

Mutations that do not affect Ssk1-R2 activity

Before the co-crystal structure was solved, Ssk1-R2 mutants were constructed to test the effects of binding with Ypd1. The following mutants did not significantly affect binding with Ypd1-T12C~F in the fluorescence assay: D554N, S612A, T631A, N635A, L636S (purifications not shown) (Figure 37 (pg. 63)). When tested in the fluorescence binding assay, these mutants retained a low nanomolar dissociation constant with Ypd1, similar to WT Ssk1-R2 (Table 5). A significant observed $\Delta\Delta G_{binding}$ was considered to be >1 kcal/mol[3]. When titrated into Ypd1-T12C~F in the fluorescence binding assay, all mutants produced a quenching effect of the fluorescence signal, supporting the hypothesis that W638 is responsible for this effect. Other mutants that were created but not tested due to their distal positions with respect to the interface in the final co-crystal

structure were L639S, E645Q, W646A, G647Q, and Q650L (purifications not shown) (Figure 37).

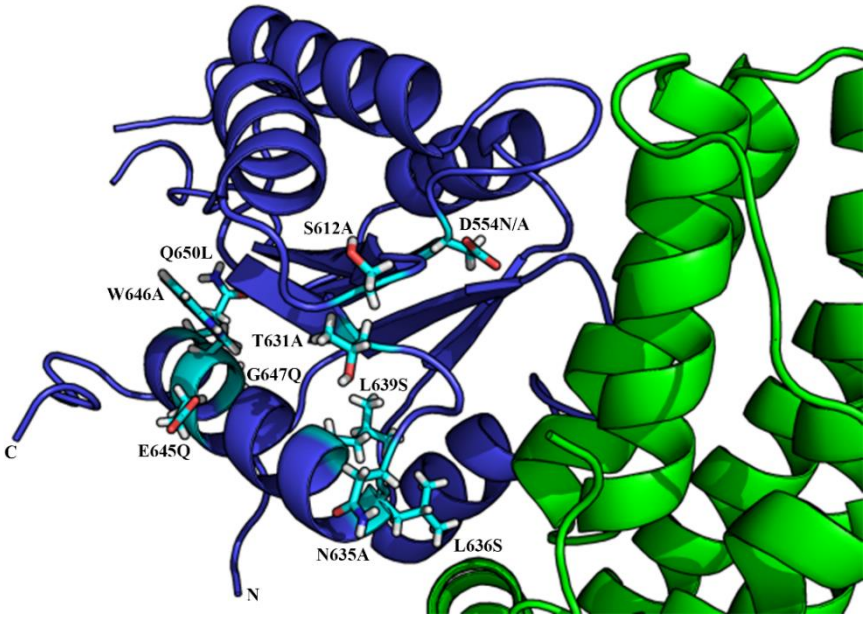

Figure 37. Illustration of Ssk1-R2 mutants that did not affect Ypd1 binding.
Ribbon representation of point mutants (stick, cyan) are shown on Ssk1-R2^{W638A} (blue). Ypd1 is shown in green.

Table 5. K_d values of Ssk1-R2 point mutants that did not affect Ypd1 binding.
Minimum number of replicates (*N*=3). Entropic contributions were assumed constant when calculating observed $\Delta\Delta G_{binding}$ for each mutant.

Ssk1-R2 variant	Observed K_d with Ypd1-T12C~F (K_d ± mean error) ± standard error of mean	Observed $\Delta\Delta G_{binding}$ (kcal/mol)
WT	**(25.1 ± 2.4) ± 1.3 nM**	**0**
W638A	(122.5± 15.0) ± 36.7 nM	0.93
D554N	(71.1 ± 6.2) ± 4.9 nM	0.61
Q556A	(75.9 ± 1.6) ± 1.0 nM	0.65
S612A	(22.9 ± 1.9) ± 1 nM	-0.05
L636S	(18.7 ± 1.6) ± 1.5 nM	-0.17
N635A	(14.3 ± 1.0) ± 0.6 nM	-0.33
T631A	(14.3 ± 1.5) ± 1.6 nM	-0.33

Discussion

Ssk1-R2-W638A was not significantly altered from WT activity with respect to Ypd1 binding affinity, phospho-accepting ability, or autodephosphorylation activity, suggesting that the co-crystal structure likely represents a physiologically relevant complex.

However, Ssk1-R2-W638A~P exhibited minor back-transfer to Ypd1 *in vitro*. Active site mutant Ssk1-R2-Q556A~P displayed the same reversible transfer to Ypd1. Since neither Ssk1-W638A nor Q556A significantly altered the ability to bind to Ypd1, these results indicate that W638 and Q556 of Ssk1 could play a role in stabilizing the strongly-favored unidirectional Sln1 pathway. Ssk1-R2-S612A did not show reversible phosphotransfer to Ypd1, but it did not retain WT-like autodephosphorylation like the Ssk1-R2-Q556A mutant. Since it also did not alter Ypd1 binding, it is likely that residue S612 of Ssk1 does not play a role in the apparent irreversibility of the phosphotransfer reaction, but may be implicated in affecting autodephosphorylation of Ssk1-R2.

Since both Ssk1-R2-W638A~P and Q556A~P showed back-transfer to Ypd1, quantifying the phospho-stabilization by Ypd1 could not be done accurately. Instead, the non-phosphorylatable Ypd1-H64 mutant was used. In published WT Ssk1-R2 assays, the half-life of Ssk1-R2~P in the presence of Ypd1 is ~40 hours and ~2 hours in the presence of Ypd1-H64Q[6]. Compared to WT, both Ssk1-R2-W638A and Ssk1-R2-Q556A displayed 3-fold extended phosphorylated half lives in the presence of Ypd1-H64Q.

Ssk1-R2-I518S served as a suitable negative control in the fluorescence assay by disrupting binding with Ypd1-T12C~F, which was reflected in a phosphotransfer assay with Ypd1. Ssk1-R2-D554N was a reliable control for the phosphotransfer assay due to its inability to accept a phosphoryl group without disrupting binding to Ypd1, per the fluorescence binding assay.

Guided by the co-crystal structure, two ionic interactions were found to play an important role in the affinity of Ypd1 and Ssk1-R2. Ssk1-R2-R524/Ypd1-D24 (2.6 Å) along with Ssk1-R2-K525/Ypd1-D23 (3.5 Å) formed an adjacent double salt bridge at the interface of Ypd1 (αA-αB loop) and Ssk1-R2^{W638A} (α1 helix) (Figure 38).

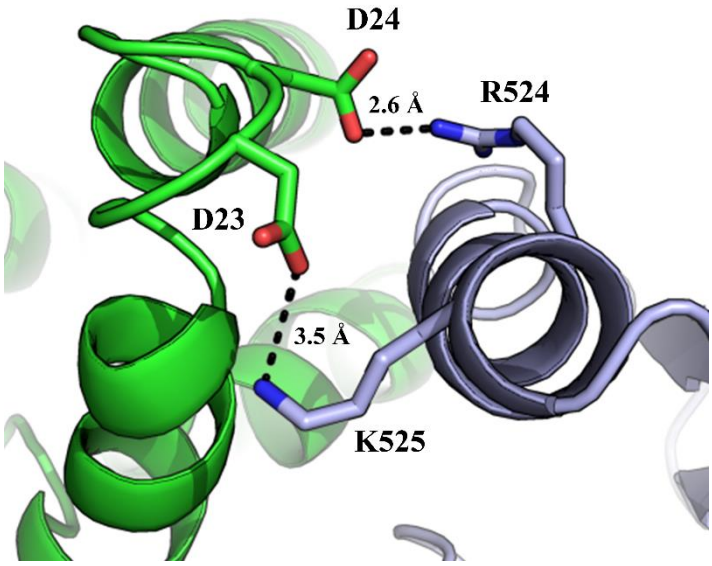

Figure 38. Ribbon and stick illustration of salt bridge interactions.
Ypd1 (green) D23 and D24 on the αA-αB loop forms two contiguous salt bridges with Ssk1-R2^{W638A} (blue) K525 and R524 on the α1 helix, respectively.

Although Ssk1-R2-R524A and Ssk1-R2-K525A played an important role in binding affinity with Ypd1, the mutants did not disrupt phosphotransfer from Ypd1~P *in vitro*, nor alter the preference of Ypd1 to phosphorylate Ssk1-R2 over Skn7-R3. These single ionic mutations disrupted binding in the fluorescence assay, but did not

completely abolish the Ypd1-Ssk1-R2 interaction. This leads me to believe that both salt bridges must be disrupted at once to see an abolishment that would be reflected in phosphorelay from Ypd1. Since Ssk1-R2-R524 and K525 form a contiguous salt bridge patch, a double mutant was constructed and verified with DNA sequencing (Ssk1-R2-R524A/K525A) to abolish both interactions. Unfortunately, this mutant would not transform into expression cells and could not be evaluated. The double-abolishment would likely have a greater impact on binding affinity and phosphotransfer with Ypd1. In the future, this hypothesis could be tested by using a single point mutant from Ssk1-R2 (e.g. Ssk1-R2-R524A) and a single point mutant from Ypd1 (e.g. Ypd1-D23A) to abolish both ionic interactions.

Experimental Section

Construction of mutants

All Ssk1-R2 mutants were created by QuikChange mutagenesis (see Appendix A) from the wild-type plasmid in a hybrid pET11a/pCYB2 vector. Double and triple mutants (Ssk1-R2-R524A-K525A and Ssk1-R2-R524A-K525A-H637A) were constructed and confirmed by DNA sequencing. They could not be transformed into expression cells and were not able to be evaluated. For most of the point mutants, with the exception of V634S (insoluble) and W638A (increased solubility), purification was identical to WT Ssk1-R2 and produced soluble protein with a similar yield (1-2 mg/L).

Transformation

Transformations were carried out by incubating nanogram quantities of plasmid DNA with competent *E. coli* cells (50-250 µL) on ice for 30 minutes followed by a 30-45 second heat-shock at 42 °C. After cooling cells on ice for 2-5 minutes, LB or SOC

was added to the reaction up to 500-1000 µL and cells were incubated for 60 minutes, 200 rpm, 37 °C. Cells were plated on LB + ampicillin and incubated overnight at 37 °C.

Protein purification

Ssk1-R2 mutants were purified using the IMPACT (NEB) system as described in Chapter 2. For phosphotransfer and fluorescence binding assays, 1 mL or 500 µL elutions from chitin columns were sufficiently pure. In some cases, proteins were further purified by size-exclusion chromatography (Sephadex®-G75). Proteins were generally flash-frozen in an ethanol/dry ice bath directly from the chitin columns and stored at -20 °C until ready for use.

Phosphotransfer experiments

Phosphotransfer from Ypd1 to Ssk1-R2 variants was measured as described previously[16] with minor modifications. Resin-bound glutathione S-transferase (GST)-HK-Sln1-R1 was incubated in 50 mM Tris pH 8.0, 100 mM KCl, 10 mM $MgCl_2$, 2 mM dithiothreitol (DTT) and 20% glycerol with 5-10 µCi (17-34 nM) [γ-^{32}P]ATP (Perkin Elmer, BLU002A250UC, 3000 Ci/mmol) and ~25 µM ATP for 30 minutes in 50-100 µL reactions for autophosphorylation. Next, Ypd1 (35 µM) was added for 5 minutes. The reaction was filter-centrifuged to remove resin-bound phospho-donor (0.45 µm filter) and the supernatant (Ypd1~P) was removed and transferred into a 50 µL solution of equimolar Ssk1-R2 variant (50 mM Tris pH 8.0, 100 mM KCl, 15 mM $MgCl_2$, 2 mM DTT). Aliquots were removed at various time points and added to 1X stop buffer (0.25 M Tris pH 6.8, 8% SDS, 60 mM EDTA, 40% glycerol, and 0.008% bromophenol blue) to quench reactions. Samples were separated on 15% SDS-PAGE gels and analyzed

with a Typhoon phosphorimager (GE Healthcare). Gels were stained in Coomassie stain and each phosphorimage band and Coomassie-stained gel was quantified using ImageJ[17]. When phosphorylation levels were quantified, each radio label signal was normalized with its corresponding Coomassie protein band to correct for any loading inconsistencies. The radiolabel signals were compared to each other to determine efficiency.

Phosphorylated half-life experiments were conducted as reported previously[5] with the only modification being the use of [γ-^{32}P]ATP with higher specific activity (Perkin Elmer, BLU002A250UC, 3000 Ci/mmol). GST-Sln1-HK and the Ssk1-R2 variant (100 µL) were incubated for 90 minutes in 50 mM Tris pH 8.0, 100 mM KCl, 10 mM $MgCl_2$, 2 mM DTT and 20% glycerol with 10 µCi (~30-70 nM) [γ-^{32}P]ATP. The reaction was filter-centrifuged to remove resin-bound phospho-donor (0.45 µm filter) and the supernatant (Ssk1-R2~P) was removed and transferred into a 5 µL solution of equimolar Ypd1, Ypd1-H64Q or buffer (50 mM Tris pH 8.0, 100 mM KCl, 15 mM $MgCl_2$, 2 mM DTT). Aliquots were removed at various time points and added to 1X stop buffer (0.25 M Tris pH 6.8, 8% SDS, 60 mM EDTA, 40% glycerol, and 0.008% bromophenol blue) to quench reactions. Samples were flash-frozen as needed and stored at -20 °C until all aliquots were ready for analysis. Samples were separated on 15% SDS-PAGE gels and exposed to a storage phosphor screen (GE Healthcare) overnight. The screens were analyzed with a Typhoon phosphorimager (GE Healthcare) and processed with ImageJ[17]. Gels were Coomassie-stained to determine protein load. Rate constants for the dephosphorylation of Ssk1-R2 variants and half-

lives were determined by least-squares fitting of the natural logarithm of the data to a linear relationship assuming first-order kinetics as previously published[6].

Fluorescence binding affinity

Ypd1-T12C was purified and buffer-exchanged into 50 mM Tris-HCl pH 9.0 with 100 mM NaCl with 5-fold molar excess of Tris-(2-carboxyethyl)phosphine-HCl (TCEP) to keep the reaction in a reduced environment. The protein was incubated in darkness for 2 hours at room temperature with a 7-fold molar excess of 5-IAF for covalent labeling on the exposed cysteine. Unincorporated 5-IAF was removed using size-exclusion chromatography (50 mL Sephadex®-G25 column at pH 8.0). Labeling efficiency of Ypd1-T12C was 71%. Labeled Ypd1-T12C (Ypd1-T12C~F) was aliquoted and stored in the presence of 10% glycerol at -20 ˚C until ready for use.

Before beginning the assay, proteins were thawed and equilibrated to room temperature. Fluoresceinated Ypd1-T12C was added to a quartz fluorescence cuvette containing a reaction buffer of 50 mM Tris-HCl pH 8.0, 10 mM $MgCl_2$, and 1 mM DTT in a total volume of 2.5 mL. All assay buffers were passed through a 10 mL Chelex® (BioRad) column to remove trace metal impurities before use. Ssk1-R2 variants were titrated into the cuvette in 2-20 μL increments to a final volume of 2.7 mL. The reaction was constantly stirred slowly with a magnetic stir bar and allowed to equilibrate for 20 seconds. The fluorescence intensity was measured with each addition of Ssk1-R2 variant in order to generate an equilibrium binding curve. Ssk1-R2 concentrations were optimized for each assay and the Ypd1-T12C~F concentration was kept constant at 6, 15 or 30 nM. Assays were designed in such a way that the concentration of the first addition of the Ssk1-R2 variant started below the

concentration of Ypd1-T12C~F and gradually increased in order to bracket the expected K_d. For Ssk1-R2-W638A, titrations spanned 10-1300 nM. For Ssk1-R2 and other mutants, titrations spanned 3-300 nM. The 5-IAF tag attached to Ypd1-T12C was excited at 488 nm and emission was observed at 515 nm (Fluoromax-4 Spectrofluorometer from Horiba Scientific, excitation and emission slit widths set to 5 nm, 23 °C). The fluorescence intensity measurements were corrected for volume before data analysis. Fractional fluorescence was calculated (F/F_0) and response curves were adjusted to begin at the origin and increase ((F/F_0-1) for Ssk1-R2-W638A; (1-F/F_0) for all other Ssk1-R2 variants). Kaleidagraph was used to program an expanded quadratic equation to fit data and calculate dissociation constants (Equation 1). $\Delta\Delta G_{binding}$ was determined by assuming entropic contributions were constant (Equation 2).

Equation 1. Quadratic equation used to analyze fluorescence binding data.

$$F_T = F_B\left(\frac{(K_d+[A_T]+[B_T])\pm\sqrt{(K_d+[A_T]+[B_T])^2-4[A_T][B_T]}}{2}\right)+$$

$$F_F\left([B_T]-\left(\frac{(K_d+[A_T]+[B_T])\pm\sqrt{(K_d+[A_T]+[B_T])^2-4[A_T][B_T]}}{2}\right)\right)$$

$[A_T] = [\text{Ssk1} - \text{R2}], x$ variable; $[B_T] = [\text{Ypd1}]$; $K_d =$ dissociation constant; $F_B =$ fluorescence of bound protein; $F_F =$ fluorescence of free protein; $F_T =$ total fluorescence; $[B_T] < K_d$

Equation 2. Equation to calculate $\Delta\Delta G_{binding}$ between Ssk1-R2 and mutants with Ypd1-T12C~F.

$$\left[\frac{RT(\ln K_d)}{4184\ \text{J}}\right]_{WT} - \left[\frac{RT(\ln K_d)}{4184\ \text{J}}\right]_{mutant}$$

$R =$ gas constant ($8.314462\ \text{J}\cdot\text{K}^{-1}\text{mol}^{-1}$; $T =$ temperature (296 K)

References

[1] Porter, S. W., Xu, Q., and West, A. H. (2003) Ssk1p response regulator binding surface on histidine-containing phosphotransfer protein Ypd1p, *Euk. Cell 2*, 27-33.

[2] Porter, S. W., and West, A. H. (2005) A common docking site for response regulators on the yeast phosphorelay protein YPD1, *Biochim. Biophys. Acta 1748*, 138-145.

[3] Lise, S., Buchan, D., Pontil, M., and Jones, D. T. (2011) Predictions of hot spot residues at protein-protein interfaces using support vector machines, *PLoS ONE 6*, e16774.

[4] Schrödinger, L. (2010) The {PyMOL} Molecular Graphics System, Version~1.3.

[5] Janiak-Spens, F., Sparling, J. M., Gurfinkel, M., and West, A. H. (1999) Differential stabilities of phosphorylated response regulator domains reflect functional roles of the yeast osmoregulatory SLN1 and SSK1 proteins, *J. Bacteriol. 181*, 411-417.

[6] Janiak-Spens, F., Sparling, D. P., and West, A. H. (2000) Novel role for an HPt domain in stabilizing the phosphorylated state of a response regulator domain, *J. Bacteriol. 182*, 6673-6678.

[7] Janiak-Spens, F., Cook, P. F., and West, A. H. (2005) Kinetic analysis of YPD1-dependent phosphotransfer reactions in the yeast osmoregulatory phosphorelay system, *Biochemistry 44*, 377-386.

[8] Bourret, R. B. (2010) Receiver domain structure and function in response regulator proteins, *Curr. Opin. Microbiol. 13*, 142-149.

[9] Pazy, Y., Wollish, A. C., Thomas, S. A., Miller, P. J., Collins, E. J., Bourret, R. B., and Silversmith, R. E. (2009) Matching biochemical reaction kinetics to the timescales of life: structural determinants that influence the autodephosphorylation rate of response regulator proteins, *J Mol Biol 392*, 1205-1220.

[10] Thomas, S. A., Brewster, J. A., and Bourret.R.B. (2008) Two variable active site residues modulate response regulator phosphoryl group stability, *Mol. Microbiol. 69*, 453-465.

[11] Freeman, A. M., Mole, B. M., Silversmith, R. E., and Bourret, R. B. (2011) Action at a distance: Amino acid substitutions that affect binding of the phosphorylated CheY response regulator and catalysis of dephosphorylation can be far from the CheZ phosphatase active site, *J. Bacteriol. 193*, 4709-4718.

[12] Xu, Q., Porter, S. W., and West, A. H. (2003) The yeast YPD1/SLN1 complex: Insights into molecular recognition in two-component systems, *Structure 11*, 1569-1581.

[13] Horie, T., Tatebayashi, K., Yamada, R., and Saito, H. (2008) Phosphorylated Ssk1 prevents unphosphorylated Ssk1 from activating the Ssk2 MAP kinase kinase kinase in the yeast HOG osmoregulatory pathway, *Mol. Cell. Biol. 28*, 5172-5183.

[14] Li, S., Ault, A., Malone, C. L., Raitt, D., Dean, S., Johnston, L. H., Deschenes, R. J., and Fassler, J. S. (1998) The yeast histidine protein kinase, Sln1p, mediates phosphotransfer to two response regulators, Ssk1p and Skn7p, *EMBO J. 17*, 6952-6962.

[15] Kaserer, A. O., Andi, B., Cook, P. F., and West, A. H. (2009) Effects of osmolytes on the SLN1-YPD1-SSK1 phosphorelay system from *Saccharomyces cerevisiae*, *Biochemistry 48*, 8044-8050.

[16] Fassler, J., and West, A. H. (2010) Genetic and biochemical analysis of the SLN1 pathway in *Saccharomyces cerevisiae*, *Meth. Enzymol. 471*, 291-317.

[17] Schneider, C. A., Rasband, W. S., and Eliceiri, K. W. (2012) NIH Image to ImageJ: 25 years of image analysis, *Nat Meth 9*, 671-675.

Chapter 4: Insights gained from the co-crystal structure of Ssk1-R2^{W638A}/Ypd1

Introduction

Ypd1 has shown preference for Ssk1-R2 in phosphotransfer experiments[1], exhibited a three-fold increase in affinity for Ssk1-R2 over Sln1-R1 in yeast two-hybrid experiments[2], showed a ~1000-fold increase over Sln1-R1 in binding affinity in the fluorescence binding assay (West lab, unpublished data) and is known to stabilize phosphorylated Ssk1-R2 *in vitro*[3]. This evidence indicates that Ypd1 likely forms a strong-transient complex with Ssk1-R2, while forming a weak-transient complex with its upstream cognate partner, Sln1-R1[4, 5]. These differences are likely essential to the cell in order to maintain the function of the Sln1 stress response pathway. Ypd1~P constitutively phosphorylates Ssk1 to maintain homeostasis during unstressed periods[6] while the unphosphorylated Ssk1 dimer accumulates in the cell to activate the HOG1 pathway in times of hyperosmotic stress[7]. Since Sln1-R1 and Ssk1-R2 dock with Ypd1 on a common hydrophobic docking patch[2] using many of the same contacts, structural differences between the receiver domains of Sln1 and Ssk1 along with their interactions with Ypd1 must be responsible for their distinct biological roles.

In order to elucidate the structural basis for the differences in physiological function, this chapter compares and contrasts the individual receiver domain structures, rigid body docking positions with Ypd1, interface contacts with Ypd1 and the active site geometries of Sln1-R1 and Ssk1-R2^{W638A}. This chapter also brings together the biochemical data collected from Ssk1-R2 point mutants and discusses the possible

physiological implications to the Sln1 pathway and questions that still remain unanswered.

Comparison of Ssk1-R2^{W638A}/Ypd1 and Sln1-R1/Ypd1 complexes

Direct comparison of the structures of Sln1-R1 and Ssk1-R2^{W638A} show that they retain the same conserved $(\beta\alpha)_5$ topology. Structural alignment of the receiver domains of Sln1 and Ssk1^{W638A} shows an overall rmsd of 0.915 Å using sequence-independent superpositioning (Figure 39, panel B (pg. 75)). One notable difference is a ~20 residue loop extending from α3 to β4 on the distal end of Ssk1 that is absent in Sln1. In the Ssk1-R2^{W638A}/Ypd1 crystal structure, electron density was not observed for 15 residues of this loop, suggesting that this region is highly flexible. In addition, the construct of Ssk1-R2^{W638A} contains a 50-residue C-terminal tail with no observable electron density, suggesting high flexibility and lack of ordered structure.

Although there is high tertiary structure similarity (<1 Å rmsd), the receiver domains are not identical (Figure 39, panel C (pg. 75)). The largest differences appear on the side of the receiver domain distal to the Ypd1 interface. For example, the C-terminal end of the α1 helix is shifted 4.2 Å in Ssk1-R2^{W638A}. Additionally, the α3 helix in Ssk1-R2^{W638A} extends 6.9 Å further than the α3 helix in Sln1-R1. In Sln1-R1, the α2-β3 loop extends 7.4 Å beyond the α2-β3 loop in Ssk1-R2^{W638A}. These differences may or may not affect the Ypd1 interaction, but since they are not located at the interface, it is unlikely that these differences play a central role.

The high conservation in tertiary structure between Sln1-R1 and Ssk1-R2^{W638A} and the shared Ypd1 binding site suggest that the receiver domains may interact with Ypd1 in approximately the same orientation. Comparison of the co-crystal structures

show that this is not the case. A rigid body movement of the receiver domain docking positions on Ypd1 is apparent (Figure 39, panel A). This indicates that the interfaces between Ypd1 and its cognate receiver domains are distinct, at least in the unphosphorylated state.

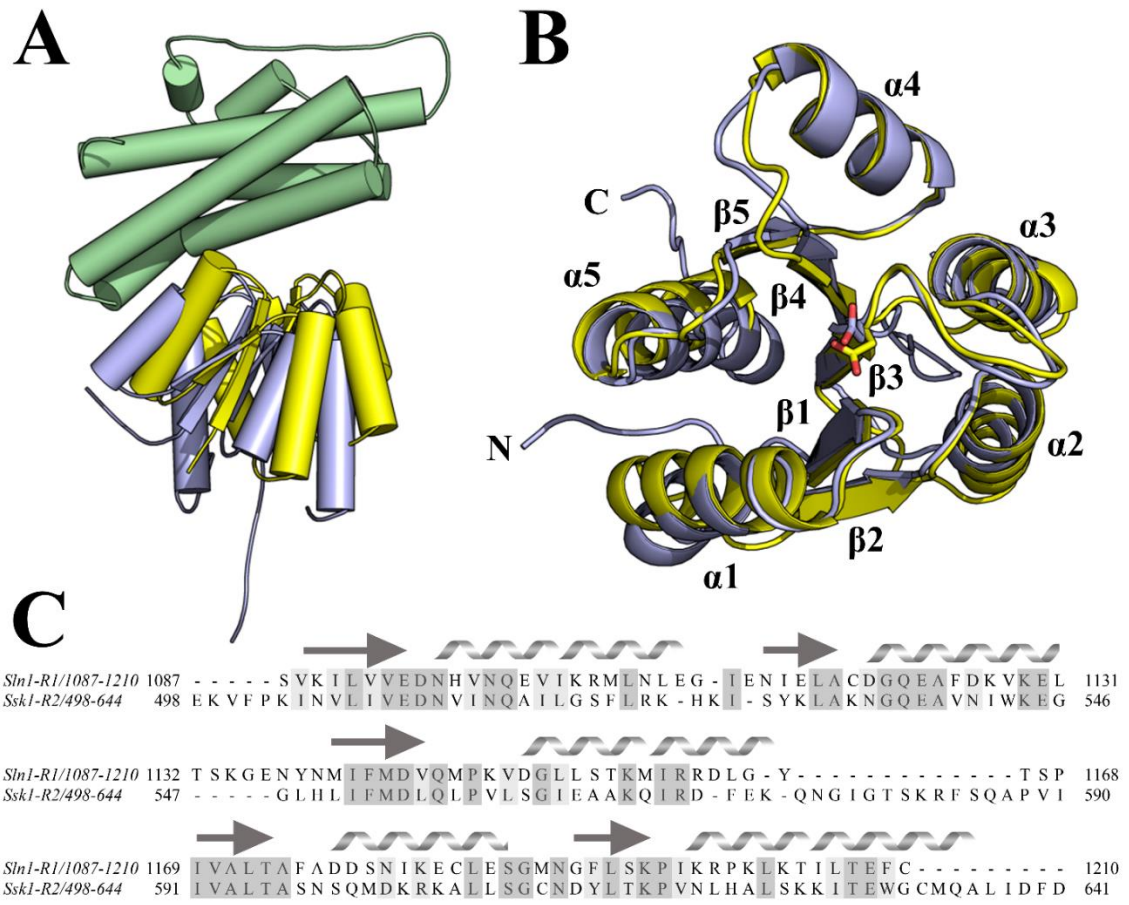

Figure 39. Structural comparison of Sln1-R1 and Ssk1-R2^{W638A} with Ypd1.
A) Sln1-R1 (yellow, PDB ID: 1OXB) and Ssk1-R2^{W638A} (blue) interface with Ypd1 (green) at the same hydrophobic docking site but have different rigid body positions. B) Sln1-R1 (yellow, PDB ID: 1OXB) superpositioned with Ssk1-R2^{W638A} (blue). The sites of phosphorylation (Sln1-R1-D1144, Ssk1-R2-D554) are shown as sticks. C) Sln1-R1 and Ssk1-R2 structure-based sequence alignment performed with UCSF Chimera[8]. Secondary structure is indicated above the sequence (β-strands are arrows, α-helices are ribbons).

Comparison of Ssk1-R2^{W638A}/Ypd1 and Sln1-R1/Ypd1 interfaces

In 2008, Horie et al.[7] described mutants of Ssk1-R2 (E510G, N512T, I514T, and I518T) that abolished interactions with Ypd1 *in vivo*. The co-crystal structure strongly corroborates that data by demonstrating that these residues play important roles in Ypd1 complex formation. N512 on Ssk1-R2^{W638A} is a central interfacial residue. It forms hydrogen bonds with Q38 and S69 of Ypd1 along with a hydrophobic contact to F65. I514 is involved in a hydrophobic contact with F35 of Ypd1, while I518 is involved in hydrophobic contacts with L31, I17 and A72 of Ypd1. E510 is a highly conserved active site residue that participates in coordination of the divalent metal cation required for proper side chain geometry during the phosphotransfer event. It does not directly contact Ypd1 in the complex structure, but it does appear to stabilize N515 through an intramolecular salt bridge (4.0 Å). This asparagine forms a hydrophobic contact with A72 and G68 of Ypd1.

In addition to corroborating *in vivo* data, the structure also confirms that Ypd1 uses the same hydrophobic patch[2] to interact with Sln1-R1 and Ssk1-R2. Although the area of interaction on Ypd1 is the same, the rigid body docking positions are different and there are many unique contacts at the Ssk1-R2^{W638A}/Ypd1 interface (Table 6).

Table 6. Interface contacts in Sln1-R1/Ypd1 and Ssk1-R2^{W638A}/Ypd1.

Ypd1 Residue	Location	Sln1-R1 Residue(s)	Location	Ssk1-R2^{W638A} Residue(s)	Location
Interactions that are similar in Sln1-R1/Ypd1 (PDB 1OXB) and Ssk1-R2^{W638A}/Ypd1					
Hydrophobic interactions					
ILE13	αA	PRO1196	β5-α5 loop	PRO633	β5-α5 loop
ILE17	αA	VAL1102	α1	ILE518	α1
MET20	αA	LEU1109	α1	LYS525	α1
PHE27	αB	ARG1105	α1	SER521	α1
LEU31	αB	VAL1102, VAL1098	α1	ILE518, ILE514	α1
SER69	αC	VAL1098	α1	ILE514	α1
ALA71	αC	PRO1196	β5-α5 loop	PRO633	β5-α5 loop
ALA72	αC	PRO1196, VAL1102	β5-α5 loop, α1	PRO633, ILE518	β5-α5 loop, α1
Hydrogen bonds					
GLN38 Oε1	αB	ASN1096 Nδ2	β1-α1 loop	ASN512 Nδ2	α1
GLN38 Nε2	αB	ASN1096 Oδ1	β1-α1 loop	ASN512 Oδ1	α1
PHE65 O	αC	ASN1096 Nδ2	β1-α1 loop	ASN512 Nδ2	α1
GLY68 O	αC	ASN1099 Nδ2	α1	ASN515 Nδ2	α1
Salt bridges					
HIS64 Nε2	αC	ASP1095 Oδ2	β1-α1 loop	ASP511 Oδ2	β1-α1 loop
Interactions that are unique between Sln1-R1/Ypd1 (PDB 1OXB) and Ssk1-R2^{W638A} Ypd1					
Hydrophobic interactions					
ILE13	αA	LYS1198	α5		
ILE17	αA			LEU636	α5
MET20	αA	ARG1105, MET1106	α1	ILE518, LEU636	α1, α5
PHE27	αB	VAL1102	α1	ALA517	α1
LEU31	αB			ALA517	α1
PHE35	αB			ILE514	α1
ALA72	αC	VAL1098	α1		
LEU73	αC	VAL1098	α1	ILE514, ILE518	α1
GLU83	αD	PHE1175	β4-α4 loop		
Hydrogen bonds					
GLU16 Oε1	αA	ARG1199 N	α5	HIS637 N	α5
GLU16 Oε2	αA			ASN635 Nδ2, N	α5
MET20 O	αA	ARG1105 Nη2	α1		

ASP24 Oδ2	αA-αB loop			ARG524 Nη1	α1
GLN34 Oε1	αB	HIS1097 Nδ1	α1		
GLN34 Nε2	αB	GLU1101 Oε2	α1		
ASP60 Oδ1	αC	GLN1146 Nε2	β3-α3 loop		
ASN61 Oδ1	αC	GLN1146 Nε2	β3-α3 loop		
HIS64 Nε2	αC	ASP1095 Oδ2, GLN1146 O	β1-α1 loop, β3-α3 loop		
SER69 N	αC	ASN1099 Oδ1	α1		
SER69 Oγ	αC			ASN512 Nδ2	α1
ARG90 Nη2	αD	GLN1146 Oε1	β3-α3 loop		
Water-mediated hydrogen bonds					
ASP24 Oδ2	αA-αB loop			SER521 O, Oγ	α1
HIS64 O	αC	ASP1095 Oδ2	β1-α1 loop		
GLY68 O	αC	ASN1099 Nδ2	α1		
Salt bridges					
ASP24 Oδ2	αA-αB loop			ARG524 Nη1	α1
ASP23 Oδ2	αA-αB loop			LYS525 Nζ	α1
HIS64 Nε2	αC	ASP1095 Oδ1, ASP1144 Oδ2	β1-α1 loop, β3		

Experimental data show that Ypd1 has ~1000-fold higher affinity for Ssk1-R2 than Sln1-R1. While the apo complexes of Ssk1-R2^{W638A}/Ypd1 and Sln1-R1/Ypd1 share approximately the same number of hydrophobic contacts, the Sln1-R1/Ypd1 complex possesses several structural features that are often associated with higher binding affinity[9-11]. The Ssk1-R2^{W638A}/Ypd1 complex contains only half of the number of observed hydrogen bonds, and the Sln1-R1/Ypd1 interface is ~20% larger than the Ssk1-R2^{W638A}/Ypd1 interface (analyzed with PDBePISA[12]). Because of these seemingly contradictory data, additional factors must exist that overwhelmingly contribute to the 1000-fold higher binding affinity and complex formation between Ssk1-R2 and Ypd1.

Other characteristics of the Ssk1-R2^{W638A}/Ypd1 interface can help explain the dissimilar biochemical activities observed between Ypd1 and its upstream and downstream cognate receiver domains. The Sln1-R1/Ypd1 structure has a surface complementarity score (Sc) of 0.624, and the Ssk1-R2^{W638A}/Ypd1 structure has Sc = 0.651 (where 0 = no complementarity and 1= perfect complementarity)[13]. This indicates that as Ypd1 encounters Ssk1-R2^{W638A}, their shapes conform to one another to a higher degree than Ypd1/Sln1-R1. The slightly higher surface complementarity could partially contribute to the higher Ypd1/Ssk1-R2 affinity[14] and stabilization of Ssk1-R2~P by Ypd1.

Although surface complementarity could be a contributing factor, the co-crystal structure revealed that the most likely reason for the observed ~25 nM affinity and strong transient complex formation between Ypd1 and Ssk1-R2 is electrostatic complementarity. Firstly, the overall electrostatic potential profiles of Sln1-R1 and Ssk1-R2^{W638A} are very dissimilar; secondly, the Ssk1-R2^{W638A}/Ypd1 complex revealed a unique, contiguous salt bridge patch between the αA-αB loop of Ypd1 and the α1 helix of Ssk1-R2^{W638A}.

The calculated isoelectric point of Ypd1 is ~4, which would cause its overall charge to be negative at physiological pH (7.4). The calculated isoelectric point of Sln1-R1 is ~7, suggesting that its overall charge would be neutral at physiological pH. The calculated isoelectric point of Ssk1-R2 is ~10.5, indicating that it would carry a strong positive charge at physiological pH, causing a heightened attraction between Ypd1 and Ssk1-R2. This overall attraction between Ypd1 and Ssk1-R2 would influence kinetic on rates that contribute to affinity[15]. Electrostatic potential maps (Figure 40) of

the co-crystal structures confirm that large patches of negative potential on Ypd1 correlate to patches of positive potential on Ssk1-R2^{W638A}. Similar areas of positive and negative potential exist at the Sln1-R1/Ypd1 interface, but are much weaker. The strongest complementary potential occurs at the location of the salt bridge formations between Ssk1-R2^{W638A} and Ypd1 (R524-D24 and K525-D23).

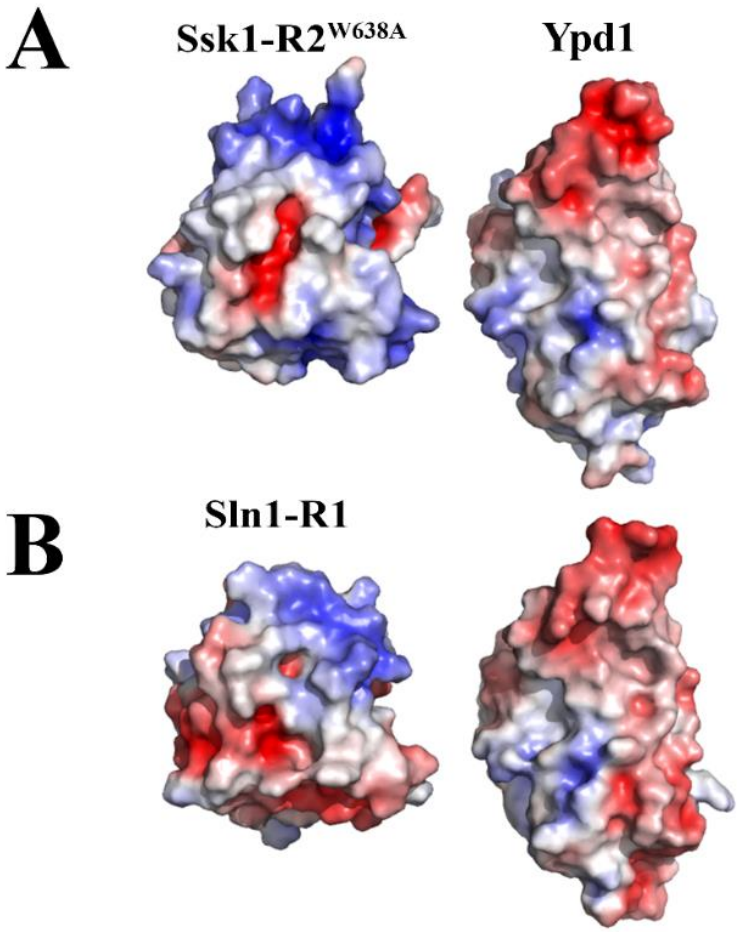

Figure 40. Electrostatic molecular surface representation of the interface view of Sln1-R1 and Ssk1-R2^{W638A} with Ypd1.
Complexes have been pulled apart and rotated 90° in order to directly view interfaces. A) Ssk1-R2^{W638A} (left) and Ypd1 (right). B) Sln1-R1 (left) and Ypd1 (right) (PDB ID: 1OXB). Electrostatic maps using AMBER ff99 force field[16] are shown. Red represents negative potential, blue represents positive potential, and white represents neutral areas.

Analysis of Ssk1-R2^{W638A}/Ypd1 and Sln1-R1/Ypd1 active sites

Comparison of the distances between the phospho-donor and acceptor atoms in the active sites of the Sln1-R1/Ypd1 and Ssk1-R2^{W638A}/Ypd1 structures reveals differences. In both apo (4.6 Å; Figure 41, panel A) and BeF_3^--activated (4.9 Å; Figure 41, panel B) structures of Sln1-R1/Ypd1, the distance between the phospho-donor (D554 Oδ1) and phospho-acceptor (H64 Nε) is ≤4.9 Å, while the distance between phospho-donor and acceptor in apo Ssk1-R2^{W638A}/Ypd1 is 6.3 Å (Figure 41, panel C).

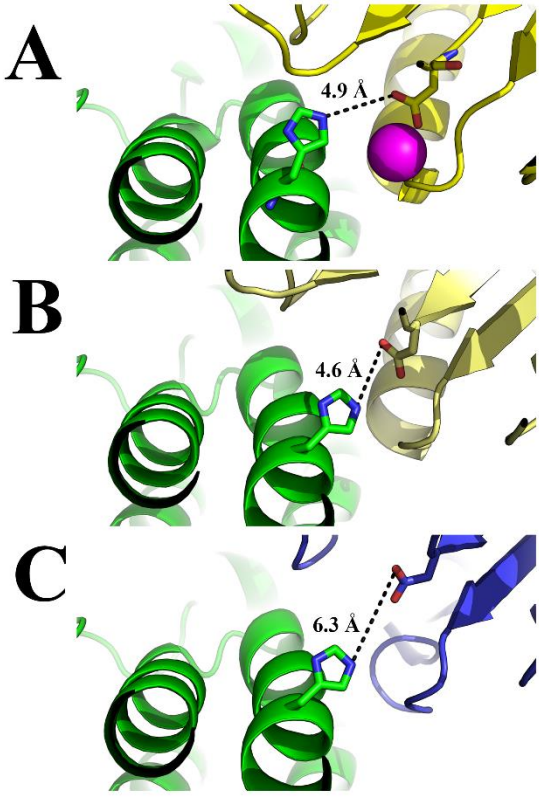

Figure 41. Distances from Ypd1-H64 to the phosphorylatable aspartate.
A) Distance of H64 Nε to D1144 Oδ1 on BeF_3^--activated Sln1-R1/Ypd1 structure (PDB ID: 2R25). Mg^{2+} shown as a magenta sphere, BeF_3^- removed for simplicity. B) Distance of H64 Nε to D1144 Oδ1 on apo Sln1-R1/Ypd1 structure (PDB ID: 1OXB). C) Distance of H64 Nε to D554 Oδ1 on apo Ssk1-R2^{W638A}/Ypd1 structure.

Since this co-crystal structure likely represents the pre-ground state encounter complex of Ssk1-R2^{W638A}/Ypd1, the active site geometry will likely shift upon Mg^{2+}-binding and phosphorylation as seen in the BeF_3^--activated structure of Sln1-R1/Ypd1[17].

The anomalous behavior of Ssk1-R2-W638A, Q556A and S612A may hold clues to the unique intermolecular interactions of Ssk1-R2 and Ypd1. Point mutations Ssk1-R2-W638A and Q556A transformed a large amino acid to a smaller amino acid, possibly allowing the phospho-donor and acceptor to come into closer proximity. This closer proximity could account for the D → H back-transfer reaction observed. Upon encounter, WT Ypd1-H64 and Ssk1-R2-D554 would be under ideal conditions to support the favored H → D phosphoryl transfer, due to the high chemical lability of the H~P bond[18] and the catalytically active receiver domain with a strong aspartate nucleophile. In the WT interaction, a larger distance between the active site residues could prevent the reverse reaction from occurring in the Ssk1-R2/Ypd1 complex. If, however, the phospho-donor and acceptor came into closer proximity, the reverse D → H reaction could occur (observed in Sln1-R1 → Ypd1[1]). Unlike the rapid dissociation of Sln1-R1 and Ypd1, which leaves 97% of Ypd1 phosphorylated before the reverse reaction can occur[1], the higher affinity between Ssk1-R2 and Ypd1 keeps them bound in a strong transient complex. By remaining bound, this could allow back-transfer to occur and be observed in phosphotransfer assays.

In the crystal structure, the position of amino acid 638 of Ssk1 does not come into direct contact with Ypd1. However, the tryptophan could make intramolecular contacts with the β5-α5 loop that interfaces with Ypd1, changing the docking position of WT Ssk1-R2 and maintaining a larger distance between the phospho-donor and

acceptor in the active site. Position 556 of Ssk1-R2 is directly in the active site in this co-crystal structure. The glutamine side chain has a very high B-factor (50.3 $Å^2$), indicating the ability to adopt multiple conformations, which was not observed in either the apo or BeF_3^--activated Sln1-R1/Ypd1 complexes[17, 19]. The highly flexible Q556 in the apo structure could be stabilized in the phosphorylated structure, keeping a larger distance between the phospho-donor and acceptor atoms in the active site. Both of these residues could also be involved in keeping the active site closed off and shielded from a hydrolytic water, accounting for the WT Ssk1-R2~P/Ypd1 stabilization.

Ssk1-W638A~P and Q556A~P were both observed to have a 3-fold increase in phosphorylated half-lives in the presence of Ypd1-H64Q 3-fold over WT. Extended half-life experiments were repeated with WT proteins on the newer phosphorimaging equipment and slight discrepancies did not appear on the hour timescale like they did on the minute timescale. As seen in Janiak-Spens et al.[3], glutamine is a poor substitute for histidine when stabilizing WT Ssk1-R2~P (~40 hours with WT Ypd1 vs. ~2 hours with Ypd1-H64Q). If W638 and Q556 are involved in maintaining the >6 Å distance between Ypd1-H64 and Ssk1-R2-D554~P, mutating them to alanine could bring the phosphoryl group closer to the nitrogen on Ypd1-H64Q, creating a shorter, stronger hydrogen bond, explaining the observed 3-fold increase of the phosphorylated half-lives of Ssk1-R2-W638A~P and Q556A~P.

Mutant Ssk1-R2-S612A~P did not exhibit normal autodephosphorylation activity in phosphotransfer assays (WT $t_{½}$ is on a ~13-23 min timescale). T610 is known to "switch" orientation upon phosphorylation to help stabilize the activated RR structure. Residue S612 is positioned in a way to be able to interact with T610, but the

current co-crystal structure does not yield enough information to form a working hypothesis about this mechanism of the apparent stabilization of Ssk1-R2-S612A~P. In order to gain more insight, a BeF_3^--activated WT co-crystal structure of Ssk1-R2 and Ypd1 would be very informative.

Discussion

In conclusion, a point mutant of Ssk1-R2 was discovered that yielded great solubility benefits and allowed for the co-crystallization of Ssk1-$R2^{W638A}_{SeMet}$ with Ypd1. The co-crystal structure showed conservation of the $(\beta\alpha)_5$ topology of receiver domains, confirmed the shared Ypd1/RR hydrophobic docking site, and also highlighted differences at the Ypd1/RR interfaces. The insertion of a single polar residue in the hydrophobic docking site abolished Ssk1-R2/Ypd1 binding and greatly diminish phosphotransfer ability.

Point mutations of intermolecular salt bridge residues (Ssk1-R2-R524A and K525A) showed that these ionic interactions played an important role in Ssk1-R2/Ypd1 affinity, but did not abolish Ypd1 phosphotransfer activity. Electrostatic potentials of Ypd1, Sln1-R1 and Ssk1-R2 could also explain to the ~1000-fold increase in affinity observed between Ypd1 and Ssk1-R2 over Sln1-R1. Ssk1 and Ypd1 should form a strong transient complex *in vivo,* explaining the constitutively phosphorylated state of Ssk1 under non-stress conditions. If electrostatic interactions are the primary basis for the Ypd1/Ssk1 complex formation, this would corroborate the reduced phospho-stability of Ssk1-R2~P by Ypd1 in response to osmolyte concentration[20]. The initial cellular response to hyperosmotic stress is a rapid efflux of water out of the cell, creating a slightly higher intracellular salt concentration. This could function as a

physiological "switch" to promote dissociation of the Ssk1-R2/Ypd1 complex *in vivo*, activating the HOG1 pathway. High levels of intracellular glycerol would again favor Ssk1-R2/Ypd1 complex formation. This could provide clues for the physiological role for Ypd1 and Ssk1 in the Sln1 pathway in response to hyperosmotic stress.

Residues W638 and Q556 were found to play a role in the apparent irreversibility of the Ypd1 → Ssk1-R2 phosphotransfer reaction, and I hypothesize that these residues are involved in maintaining a >6 Å distance between Ypd1-H64 and Ssk1-R2-D554, as well as shielding Ssk1-R2-D554~P from hydrolytic water when in complex. Point mutant S612A did not show WT autodephosphorylation activity, but any explanation would be highly speculative with the current data.

Studying the nature of protein-protein interactions in the Sln1 signaling pathway has answered some questions but also raised others. The process of how unphosphorylated Ssk1 dissociates from Ypd1 and binds Ssk2 has not been elucidated. Previous studies suggest that Ssk1 acts as an unphosphorylated dimer in the cell to bind to Ssk2/22[7], but the dimerization interface has not yet been described. Comparing the following *in vitro* affinities could shed light on the Ypd1/Ssk1~P *in vivo* dissociation, Ssk1 dimerization and Ssk1/Ssk2 binding event: Ypd1/Ssk1-R2 vs. Ssk1-R2~P, Ssk1-R2 /Ssk1-R2~P vs.Ssk1-R2. In addition, we have no structural information on full-length Ssk1. Both BLAST searches and homology modeling have turned up no clues as to the function of the N-terminal domain of *S. cerevisiae* Ssk1. Structural analysis of full-length *S. cerevisiae* Ssk1 would greatly help elucidate the complete function of Ssk1 in the Sln1 pathway.

References

[1] Janiak-Spens, F., Cook, P. F., and West, A. H. (2005) Kinetic analysis of YPD1-dependent phosphotransfer reactions in the yeast osmoregulatory phosphorelay system, *Biochemistry 44*, 377-386.

[2] Porter, S. W., and West, A. H. (2005) A common docking site for response regulators on the yeast phosphorelay protein YPD1, *Biochim. Biophys. Acta 1748*, 138-145.

[3] Janiak-Spens, F., Sparling, D. P., and West, A. H. (2000) Novel role for an HPt domain in stabilizing the phosphorylated state of a response regulator domain, *J. Bacteriol. 182*, 6673-6678.

[4] Nooren, I. M. A., and Thornton, J. M. (2003) Structural characterisation and functional significance of transient protein-protein interactions, *J. Mol. Biol. 325*, 991-1018.

[5] Perkins, J. R., Diboun, I., Dessailly, B. H., Lees, J. G., and Orengo, C. (2010) Transient protein-protein interactions: structural, functional, and network properties, *Structure 18*, 1233-1243.

[6] Posas, F., Wurgler-Murphy, S. M., Maeda, T., Witten, E. A., Thai, T. C., and Saito, H. (1996) Yeast HOG1 MAP kinase cascade is regulated by a multistep phosphorelay mechanism in the SLN1-YPD1-SSK1 "two-component" osmosensor, *Cell 86*, 865-875.

[7] Horie, T., Tatebayashi, K., Yamada, R., and Saito, H. (2008) Phosphorylated Ssk1 prevents unphosphorylated Ssk1 from activating the Ssk2 MAP kinase kinase kinase in the yeast HOG osmoregulatory pathway, *Mol. Cell. Biol. 28*, 5172-5183.

[8] Pettersen, E. F., Goddard Td Fau - Huang, C. C., Huang Cc Fau - Couch, G. S., Couch Gs Fau - Greenblatt, D. M., Greenblatt Dm Fau - Meng, E. C., Meng Ec Fau - Ferrin, T. E., and Ferrin, T. E. UCSF Chimera--a visualization system for exploratory research and analysis.

[9] Chen, J., Sawyer, N., and Regan, L. (2013) Protein–protein interactions: General trends in the relationship between binding affinity and interfacial buried surface area, *Protein Science 22*, 510-515.

[10] Sheinerman, F. B., Norel, R., and Honig, B. (2000) Electrostatic aspects of protein-protein interactions, *Curr. Opin. Struct. Biol. 10*, 153-159.

[11] Jones, S., and Thornton, J. M. (1996) Principles of protein-protein interactions, *Proc. Natl. Acad. Sci. (USA) 93*, 13-20.

[12] Krissinel, E., and Henrick, K. (2007) Protein interfaces, surfaces and assemblies' service PISA at the European Bioinformatics Institute (http://www.ebi.ac.uk/pdbe/prot_int/pistart.html); Inference of macromolecular assemblies from crystalline state, *J. Mol. Biol. 372*, 774-797.

[13] Lawrence, M. C., and Colman, P. M. (1993) Shape complementarity at protein/protein interfaces, *J. Mol. Biol. 234*, 946-950.

[14] Li, Y., Zhang, X., and Cao, D. (2013) The role of shape complementarity in the protein-protein interactions, *Sci. Rep. 3*.

[15] Sheinerman, F. B., Norel, R., and Honig, B. (2000) Electrostatic aspects of protein–protein interactions, *Curr Opin Struct Biol 10*, 153-159.

[16] Wang, J., Cieplak, P., and Kollman, P. A. (2000) How well does a restrained electrostatic potential (RESP) model perform in calculating conformational energies of organic and biological molecules?, *J. Comput. Chem. 21*, 1049-1074.

[17] Zhao, X., Copeland, D. M., Soares, A. S., and West, A. H. (2008) Crystal structure of a complex between the phosphorelay protein YPD1 and the response regulator domain of SLN1 bound to a phosphoryl analog, *J. Mol. Biol. 375*, 1141-1151.

[18] Attwood, P. V., Piggott, M. J., Zu, X. L., and Besant, P. G. (2007) Focus on phosphohistidine, *Amino Acids 32*, 145-156.

[19] Xu, Q., Porter, S. W., and West, A. H. (2003) The yeast YPD1/SLN1 complex: Insights into molecular recognition in two-component systems, *Structure 11*, 1569-1581.

[20] Kaserer, A. O., Andi, B., Cook, P. F., and West, A. H. (2009) Effects of osmolytes on the SLN1-YPD1-SSK1 phosphorelay system from *Saccharomyces cerevisiae*, *Biochemistry 48*, 8044-8050.

Chapter 5: Plasmid expression constructs for Ssk1 from *Cryptococcus neoformans*

Introduction

Cryptococcus neoformans is currently one of the most deadly of all human fungal pathogens[1]. Infections occur mostly in immunocompromised people and cause over 600,000 deaths annually worldwide[2]. *C. neoformans* is the most lethal opportunistic infection of AIDS patients in Africa (survival rate <40%) and continues to be a problem even in regions where current antifungal treatments are available. A one year mortality study was performed in Bangkok, Thailand, on AIDS patients infected with cryptococcosis. Even with treatment of amphotericin B, flucytosine, fluconazole and intraconazole, patient mortality rate was greater than 40 %[3]. Individuals with competent immune systems are generally equipped to handle exposure to fungal pathogens, but recently a related species, *Cryptococcus gattii* was found to be infectious to healthy people[4]. These developments have led to an increased urgency for the development of new antifungal therapies.

Cryptococcus is a basidiomycete yeast found in pigeon excrement, trees and soil. First exposure is usually through inhalation into the respiratory tract and normally initiates immediate immune responses such as phagocytosis and proinflammatory reactions. *C. neoformans* has adapted to invade the immunocompromised host via known virulence factors: polysaccharide capsule, melanin, cell enlargement, and sexual reproduction (α mating type). The *Cryptococcus* polysaccharide capsule blocks recognition by host phagocyte-expressed pattern-recognition receptors, while melanin prevents oxidative damage and promotes survival inside phagocytes. Melanin also allows cells to resist temperature, heavy metal and ionizing radiation stress[4, 5].

During its sexual cycle, *C. neoformans* switches from unicellular budding yeast to hyphal growth. Spores produced during mating are infectious and can colonize lung tissue, propagate in the blood, and cross the blood-brain barrier, ultimately colonizing brain tissue. Mating can also produce clinically relevant hybrids, although the yeast form is the most common morphological form in host infections[6].

To combat deadly fungal pathogens, new drugs are urgently needed. Current therapies are often toxic, lack efficacy or are rendered less effective due to the emergence of antifungal resistant strains. With the exception of 5-flucytosine, all current antifungals targeting systemic infection target cellular integrity. This is problematic since fungal pathogens are eukaryotes and share many similarities in proteins and cellular structure with humans. Only two known compounds are in the antifungal pipeline that have novel targets, and no new antifungal medications have been approved since 2006. As of 2015, at most 6 new compounds are in active clinical development for systemic fungal infections[1]. *Cryptococcus* species are intrinsically resistant to echinocandins (targets β-Glucan synthesis) and cryptococcal meningitis responds poorly to fluconazole (targets ergosterol biosynthesis)[1]. These characteristics make *C. neoformans* an excellent candidate for studying novel antifungal drug targets.

An ideal drug target would be essential to survival or virulence in the pathogen and be absent in the host organism. TCS proteins have been implicated in virulence in multiple pathogenic species (reviewed in Shor et al.[7]). No TCS inhibitor has yet reached clinical stages, even though inhibitor identification efforts have been going on for approximately 20 years. Most have focused on the inhibition of HK phosphorylation, not downstream HPts or RRs[7]. The TCS pathway that is upstream of

the *C. neoformans* HOG1 stress response pathway has been identified as an excellent candidate and may contain viable drug targets. The *C. neoformans* Tco pathway is homologous to the model organism *S. cerevisiae* Sln1 pathway.

The *C. neoformans* Tco system controls the HOG1 pathway, regulates stress responses, antifungal sensitivity, virulence factors and sexual reproduction (Figure 42 (pg. 92)). Histidine kinases Tco 1-7 don't contain transmembrane domains, so they are likely cytosolic[8]. Some Tco proteins interact with Ypd1 which functions as an intermediate HPt protein in the pathway. It interacts with Ssk1 and is also essential for *C. neoformans* survival. The fact that there is no Ypd1 homolog in mammals and that it is essential for survival make it a highly desirable drug target. All information about CnYpd1 and its cognate partners would be of great clinical interest.

C. neoformans Hog1 phosphorylation requires Ssk1. Ssk1 is essential in response to oxidative stress or UV irradiation. It is important but not essential in mediating osmotic stress responses. Deletion of Ssk1 increases fludioxonil and high temperature resistance. Ssk1 negatively regulates sexual reproduction. Disruption of the Ssk1 gene dramatically enhanced capsule and melanin productions, indicating that the HOG1 pathway negatively regulates virulence[8].

Cryptococcus hyper-virulent serotype A H99 (>95% of clinical isolates worldwide) has opposite HOG1 regulation than the less virulent *Cryptococcus* serotype D JEC21 strains and other yeasts. The HOG1 pathway is uniquely suited to attenuate virulence and differentiation in H99 but not JEC21 even though they share ~95% genome sequence identity. *CnHOG1* is a true functional homolog of *ScHOG1* because it rescued a Sc*hog1Δ* strain from hyper-osmosensitivity. Crosstalk is present between

HOG1 pathway and cAMP signaling pathway, which controls biosynthesis of capsule and melanin. Normally, Hog1 is unphosphorylated and is quickly phosphorylated and activated in response to hyperosmotic stress. Serotype D (JEC21) and *S. cerevisiae* both have this pattern. Serotype A (H99) has the opposite regulation; Hog1 is constitutively phosphorylated and is rapidly dephosphorylated upon exposure to 1M NaCl. Hog1 in serotype A and D can complement each other- the difference is in the upstream or downstream proteins. In serotype D and *S. cerevisiae*, Hog1 localizes to the nucleus after osmotic stress, but in serotype A, Hog1 is more evenly distributed between cytosol and nucleus. Hog1 is phosphorylated by Pbs2 as in the *S. cerevisiae* pathway[9]. Ssk2 is the likely upstream factor that distinguishes between constitutive Hog1 phosphorylation or dephosphorylation by interacting with Pbs2[10]. There are two informative reviews on the current understanding of the *Cryptococcus* Hog1 pathway[11, 12].

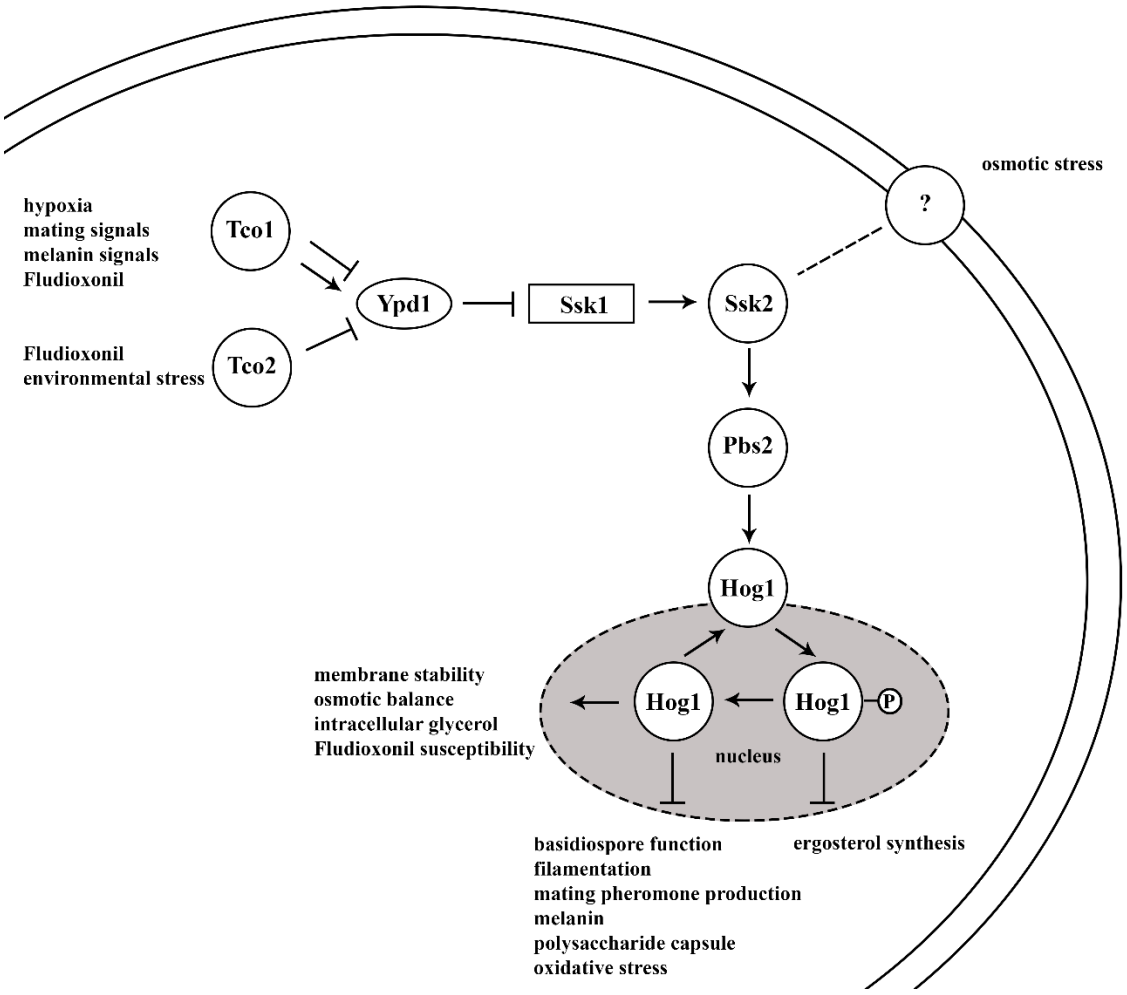

Figure 42. Illustration of HOG1 pathway in *C. neoformans*.
Figure adapted from[12].

In *C. neoformans* H99, Ssk1 is the link between Ypd1 (putative drug target, essential for survival) and Ssk2, the "master switch" for controlling the hyper-virulent characteristic of constitutive Hog1 phosphorylation. Although the *S. cerevisiae* Sln1 pathway is an important model system, there are many differences that support the rationale to study *C. neoformans* signaling proteins directly. Sequence alignments of *S. cerevisiae* Ssk1 and *C. neoformans* Ssk1 show high conservation of the receiver domains region but little overall similarity. Full length Ssk1 proteins share 17.1%

identity (global alignment with EBLOSUM62 matrix, Emboss Needle[13]) but a pairwise alignment illustrates that 189 residues encompassing the receiver domains share 51.9% identity (BLOSUM62 matrix, Expasy SIM[14]). These residues are 987-1175 of CnSsk1 and 483-666 of ScSsk1. High conservation of the receiver domain is shown in Figure 43.

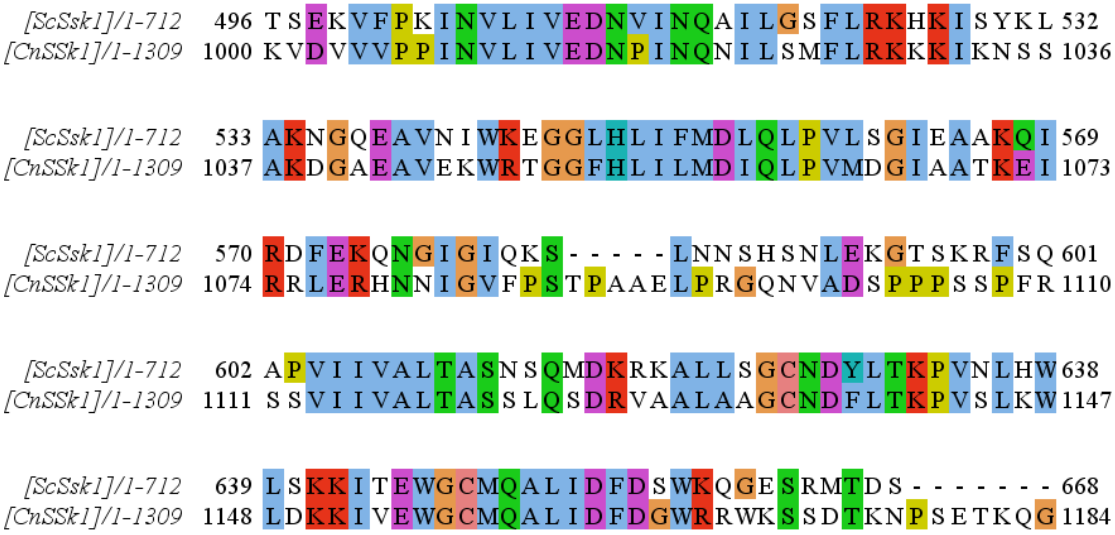

Figure 43. Sequence alignment of *Sc* and *Cn* Ssk1 receiver domains.
This figure was generated by JalView[15] using the Clustal algorithm[16].

In this chapter, attempts were made to purify portions of CnSsk1 for structural and biochemical characterization.

CnSsk1 homology modeling

Full length CnSsk1 was submitted to homology modeling using the Phyre2 program[17]. From the tertiary structure predictions, three discreet domains were generated. In order to investigate their putative functions, each domain was submitted separately to an amino acid sequence BLAST search[18]. Domain 1 (aa 265-425) and domain 2 (aa 650-825) returned no similarities to known domains. When submitted to

3D BLAST[19] and compared to known structures in the Protein Data Bank (PDB)[20] (http://www.rcsb.org/pdb/), both domains returned almost identical structure similarity to the catalytic subunit of a histidine kinase. Domain 1 was most similar to a *Thermatoga maritima* histidine kinase (PDB ID: 2C2A) with rmsd = 0.77 Å and sequence identity = 12.1%. Domain 2 was most similar to *T. maritima* histidine kinase CheA (PDB ID: 2CH4) with rmsd = 1.10 Å and sequence identity = 5.1%. Domain 3 (aa 1005-1165) was identified as an RR receiver domain (referred to as CnR2) by sequence identity and structural similarity (Figure 44). Domain 1 amino acid sequence was submitted separately to Phyre2 and the top model was returned with 97% confidence and 44% coverage as an ATPase domain of HSP90 chaperone/DNA topoisomerase II/histidine kinase fold from the histidine kinase family. When domain 2 was submitted for homology modeling alone, the predicted structure was not similar to a histidine kinase (it was mostly disordered). In conclusion, domain 1 may be a histidine kinase domain, but domain 2 is ambiguous.

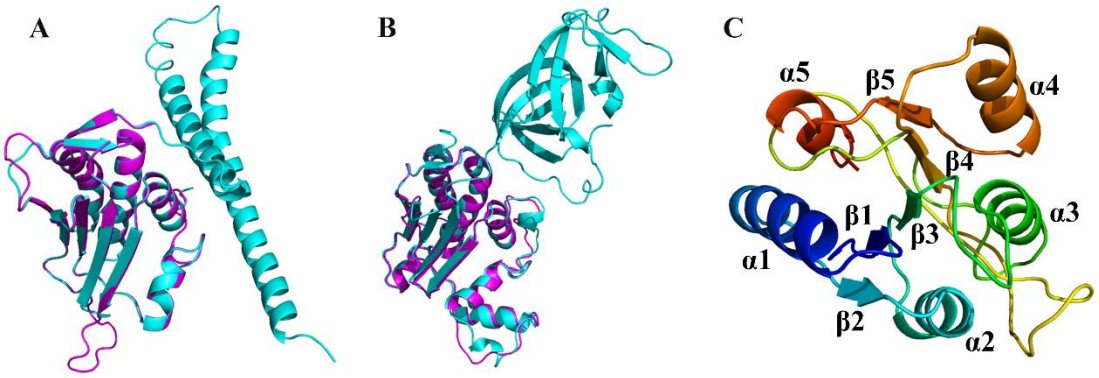

Figure 44. Homology models of 3 putative domains of CnSsk1.
A) CnSsk1 domain 1 (aa 265-425, magenta) superpositioned with a sensor histidine kinase from *T. maritima* (PDB ID: 2C2A, cyan). B) CnSsk1 domain 2 (aa 650-825, magenta) superpositioned with CheA from *T. maritima* (PDB ID: 2CH4, cyan). C) CnSsk1 domain 3 (CnR2, aa 1005-1165) receiver domain exhibiting the canonical $(\beta\alpha)_5$ fold.

In order to generate working plasmid expression constructs, segments were PCR-amplified from *C. neoformans* H99 cDNA and inserted into expression vectors to create fusion proteins. Sequencing of the cDNA revealed that we did not have full coverage of the CnSsk1 gene, making the creation of a full-length CnSsk1 protein impossible. Experiments to collect cDNA from CnSsk1 were done in the lab of Dr. Jan Fassler at the University of Iowa before I joined the West lab, and it was impractical to obtain the missing nucleotides. We had coverage from nucleotide 1-1210 (amino acid 1-403) and nucleotide 1057-3930 (amino acid 650 through the C-terminal end). Therefore we decided to mainly focus on purification of the receiver domain (CnR2), ± domain 2 or ± the C-terminal tail in order to evaluate protein-protein interactions with CnYpd1. Twelve constructs were created (named CnR2-B – CnR2-M) (Figure 45 (pg. 96)) to evaluate expression, solubility and phosphotransfer activity. In general, these protein constructs were difficult to work with. Many were insoluble. The protein constructs that were soluble were difficult to purify, and once purification was complete, phosphotransfer activity with CnYpd1 was not observed. The following is a summary of the work that was accomplished in pursuit of knowledge about the Tco1 His-Asp phosphorelay pathway of the human pathogen *C. neoformans*.

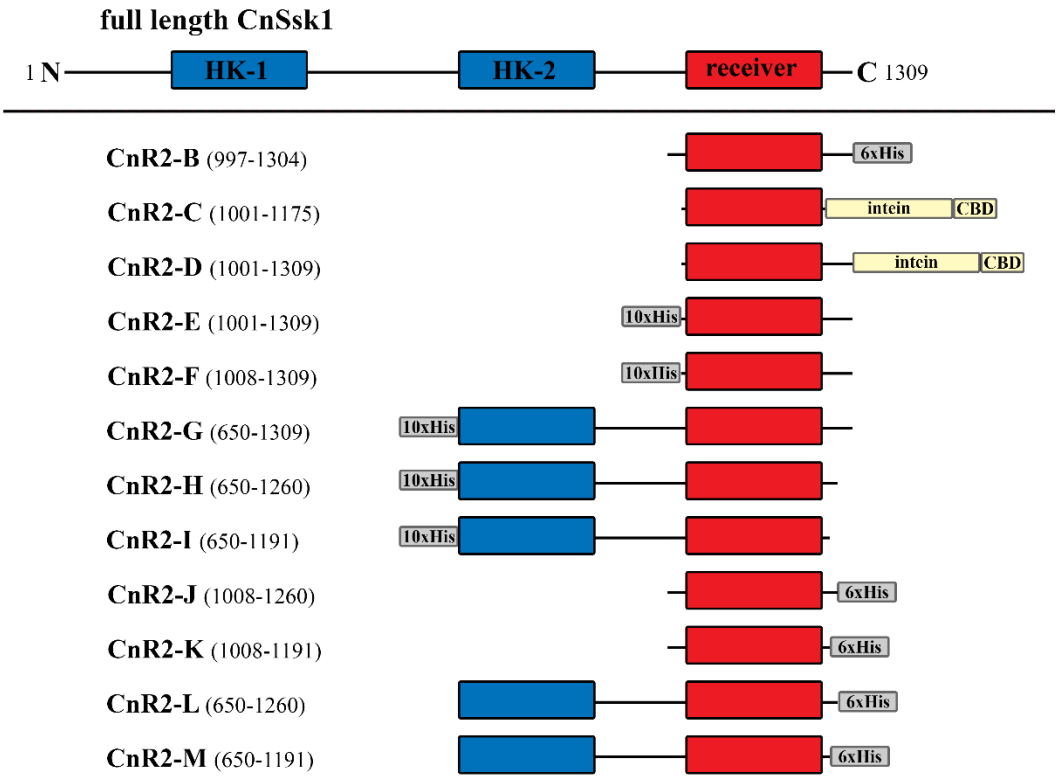

Figure 45. Schematic representation of all fusion proteins created from CnSsk1.

CnR2-A

CnR2-A (~26 kDa) was a His-tagged construct created by Lu Zhou. This construct was purified and crystallized but it was discovered that the final purified protein was not CnR2. Another 26 kDa protein was overexpressed by the addition of IPTG and was purified by a combination of Ni-NTA affinity and ion exchange chromatography. From mass spectrometry peptide ID, it was identified as beta-lactamase, the ampicillin-resistance gene carried on the pET16b plasmid.

CnR2-B

The construct, CnR2-B was created from cDNA nucleotides 2989-3912 of the *C. neoformans* H99 Ssk1 gene (Figure 46 (pg. 97)). The final 341 amino acid fusion protein had a C-terminal 6x His-tag, a calculated molecular mass of 37,239 Da and a

theoretical isoelectric point of 9.51. CnR2-B was not expressed in Rosetta cells (Figure 47).

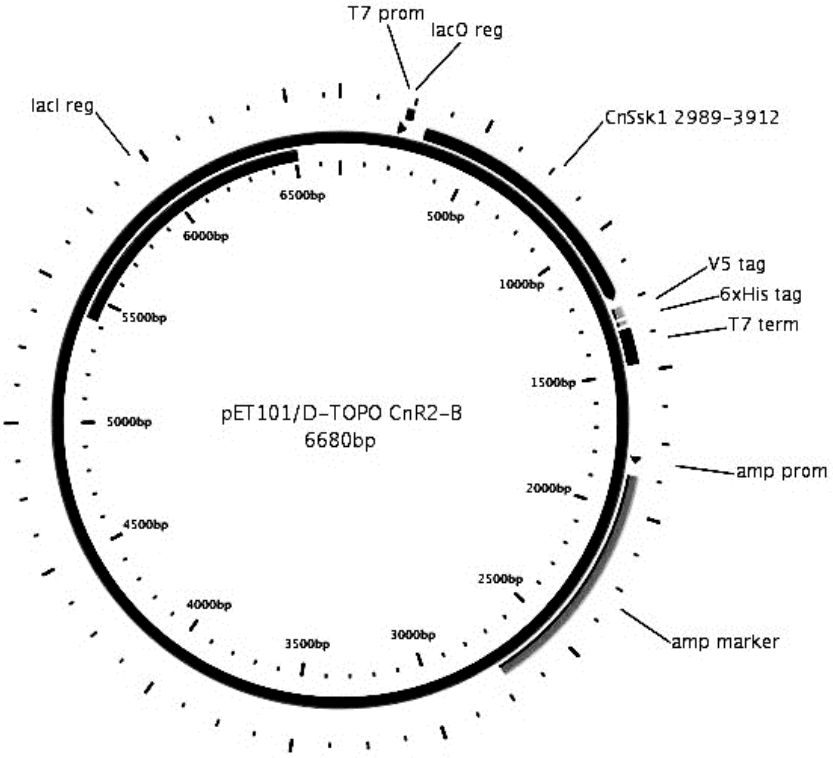

Figure 46. Plasmid map of construct CnR2-B.

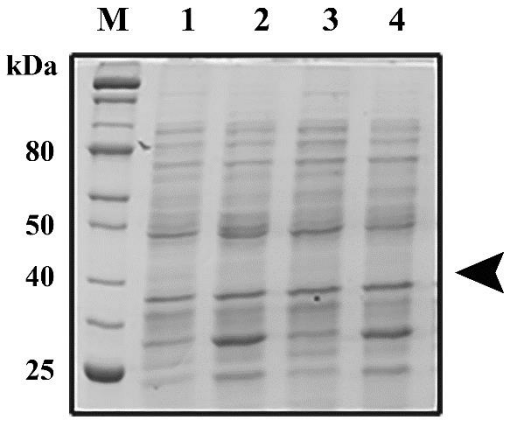

Figure 47. SDS-PAGE gel showing the absence of fusion protein CnR2-B.
M- protein marker, 1- uninduced Rosetta cells + empty vector, 2- induced Rosetta cells + empty vector, 3- uninduced Rosetta cells + vector with CnR2-B insert, 4- induced Rosetta cells + vector with CnR2-B insert. CnR2-B (~37 kDa).

CnR2-C

The construct, CnR2-C was created from cDNA nucleotides 3001-3525 of the *C. neoformans* H99 Ssk1 gene (Figure 48 (pg. 99)). The final 693 amino acid fusion protein had a C-terminal intein-chitin binding domain (CBD) tag, a calculated molecular mass of 76,966 Da and a theoretical isoelectric point of 8.55. After cleavage of the intein tag (Figure 49 (pg. 99)), the final 176 amino acid protein had a calculated molecular mass of 19,448 Da and a theoretical isoelectric point of 8.97. CnR2-C was confirmed with mass spectrometry peptide ID as a portion of *C. neoformans* Ssk1. Chitin affinity chromatography was successful as the first step of purification in CnR2-C. However, after concentration and size-exclusion chromatography, most of the protein became insoluble. Cation exchange was also attempted as a second purification step but the results were identical. Protein yield was undetectable after each second purification step. CnR2-C was, therefore, not used in any activity assays.

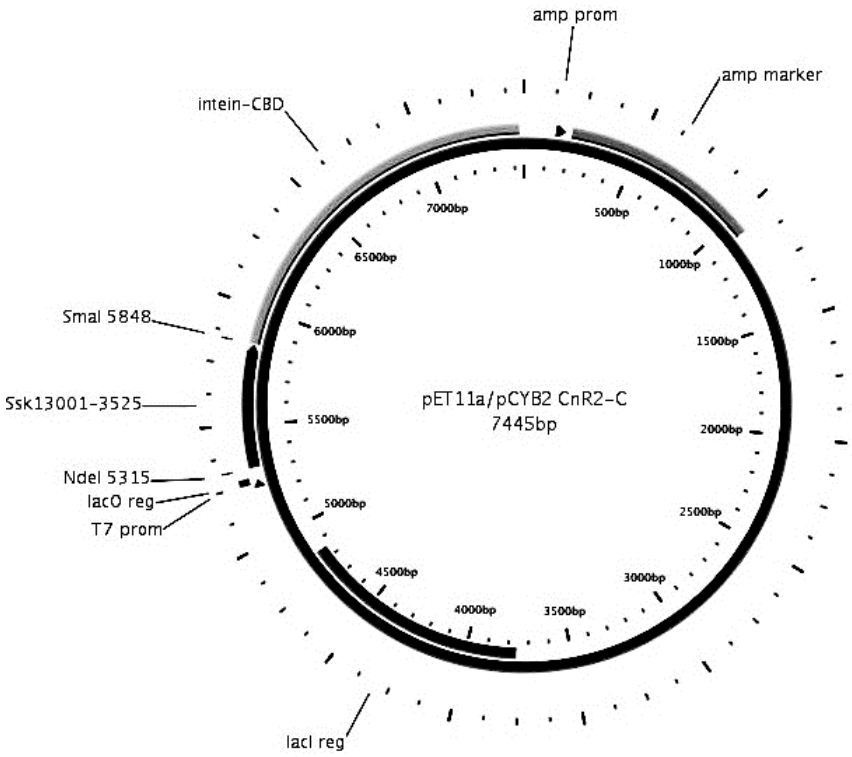

Figure 48. Plasmid map of construct CnR2-C.

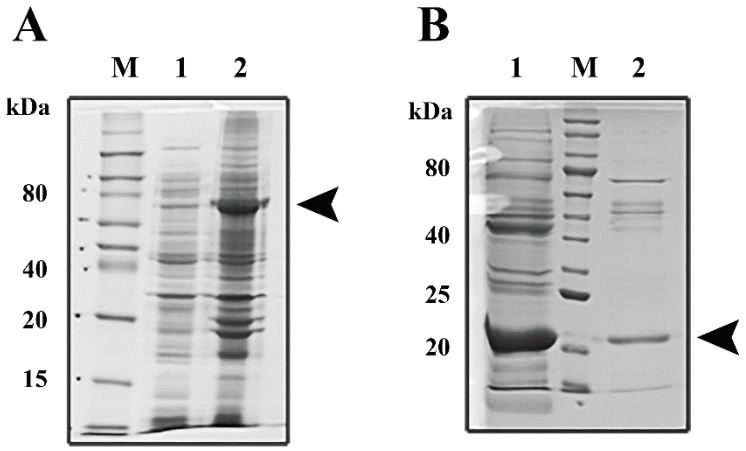

Figure 49. SDS-PAGE gels showing fusion protein CnR2-C.
A) M- protein marker, 1- uninduced Rosetta cells, 2- induced Rosetta cells overexpressing CnR2-C (~77 kDa). B) 1- pellet of cleaved CnR2-C, M- protein marker, 2- supernatant of cleaved CnR2-C. After cleavage of the intein-CBD tag (~19 kDa) and concentration, the majority of CnR2-C was insoluble.

CnR2-D

The construct, CnR2-D was created from cDNA nucleotides 3001-3927 of the *C. neoformans* H99 Ssk1 gene (Figure 50 (pg. 101)). The final 827 amino acid fusion protein had a C-terminal intein-chitin binding domain tag, a calculated molecular mass of 91,236 Da and a theoretical isoelectric point of 8.76. After cleavage of the intein tag, the final 310 amino acid protein had a calculated molecular mass of 33,717 Da and a theoretical isoelectric point of 9.32. CnR2-D was confirmed with mass spectrometry peptide ID as a portion of *C. neoformans* Ssk1. CnR2-D was successfully purified by chitin affinity chromatography as a first step. Size exclusion, cation exchange and phenyl sepharose chromatography were all attempted as a final step. Phenyl sepharose and cation exchange were unsuccessful because they did not separate CnR2-D from other proteins. Size exclusion was not successful because CnR2-D became partially insoluble during the concentration step before chromatography and the remaining soluble protein was not separated from higher molecular weight proteins (Figure 51 (pg. 101)). Despite the remaining impurities, CnR2-D was subjected to a phosphotransfer assay with CnYpd1 but did not display any activity (data not shown).

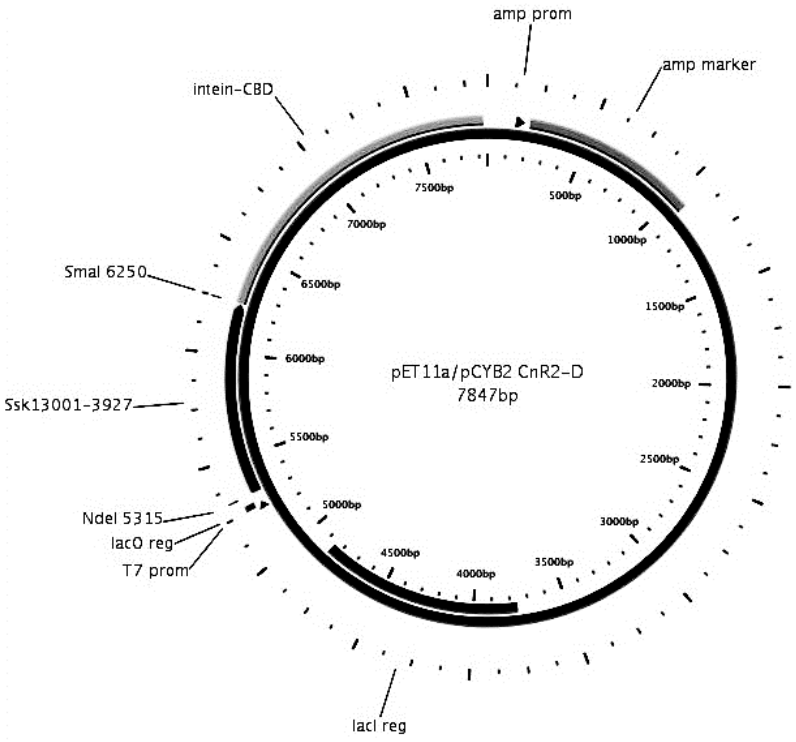

Figure 50. Plasmid map of construct CnR2-D.

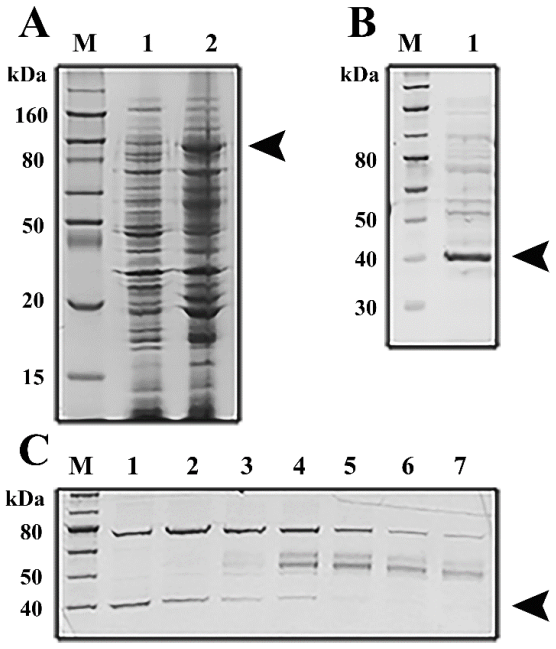

Figure 51. SDS-PAGE gels showing fusion protein CnR2-D.
A) M- protein marker, 1- uninduced Rosetta cells, 2- induced Rosetta cells overexpressing CnR2-D (~91 kDa). B) M- protein parker, 1- CnR2-D after cleavage of intein-CBD tag (~34 kDa). C) M- marker, 1-7- fractions 30-37 of a gravity S-100 size exclusion column. Gel illustrates that the majority of CnR2-D elutes with higher molecular weight proteins and the remaining pure protein was negligible.

CnR2-E

The construct, CnR2-E was created from cDNA nucleotides 3001-3927 of the *C. neoformans* H99 Ssk1 gene (Figure 52 (pg. 103)). The final 331 amino acid fusion protein had an N-terminal 10x His-tag, a calculated molecular mass of 36,238 Da and a theoretical isoelectric point of 9.32. CnR2-E was confirmed with mass spectrometry peptide ID as a portion of *C. neoformans* Ssk1. During Ni-NTA affinity chromatography, a portion of the protein appeared in the FT and did not appear to bind completely. Even though it did not bind completely, the protein yield at early stages was much more promising than constructs C-D. Cobalt and nickel HP Chelating columns (GE Healthcare) run on an AKTA prime chromatography system with imidazole gradients were attempted; nickel had the fewest impurities in the fractions containing CnR2-E. Unfortunately, cobalt and nickel affinity columns did not enrich CnR2-E. The protein was spread through approximately 15-20 fractions with no "peak" (Figure 53 (pg. 103)). During the concentration step before size exclusion chromatography, a significant amount of the protein was observed to be insoluble. In order to try to improve solubility and yield, an alanine substitution was introduced to W1147, the tryptophan residue that aligns with W638 in *S. cerevisiae* Ssk1-R2. Expression and purification attempts of CnR2-E-W1147A were identical to CnR2-E (Figure 54 (pg. 104)). A non-phosphorylatable mutant (CnR2-E-D1058A) was created, but was never purified or used in activity assays. After construct CnR2-E showed some promise, constructs F-M were created to capitalize on the success of the His-tag while searching for a protein composition that would be more amenable to purification and crystallization.

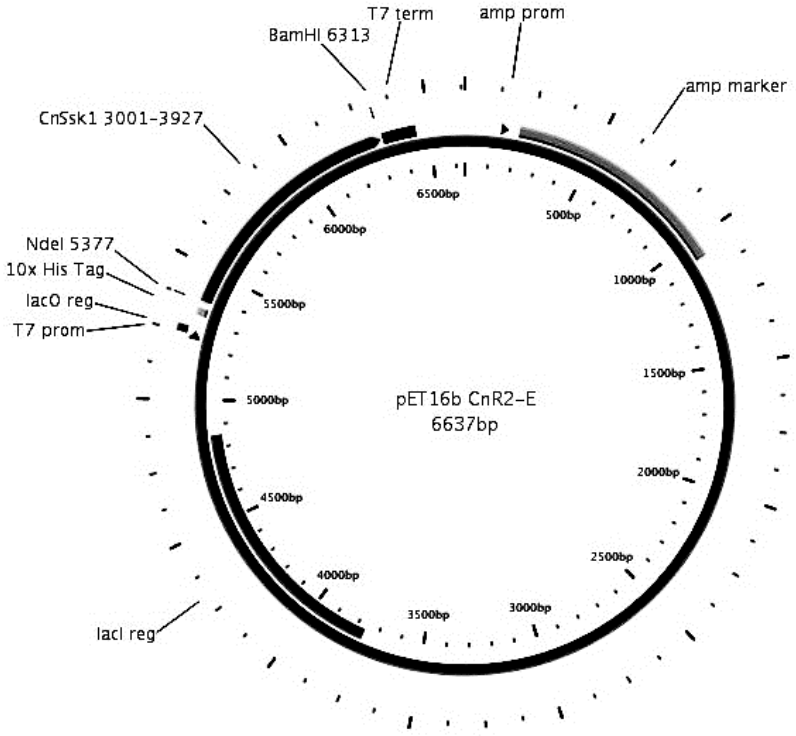

Figure 52. Plasmid map of construct CnR2-E.

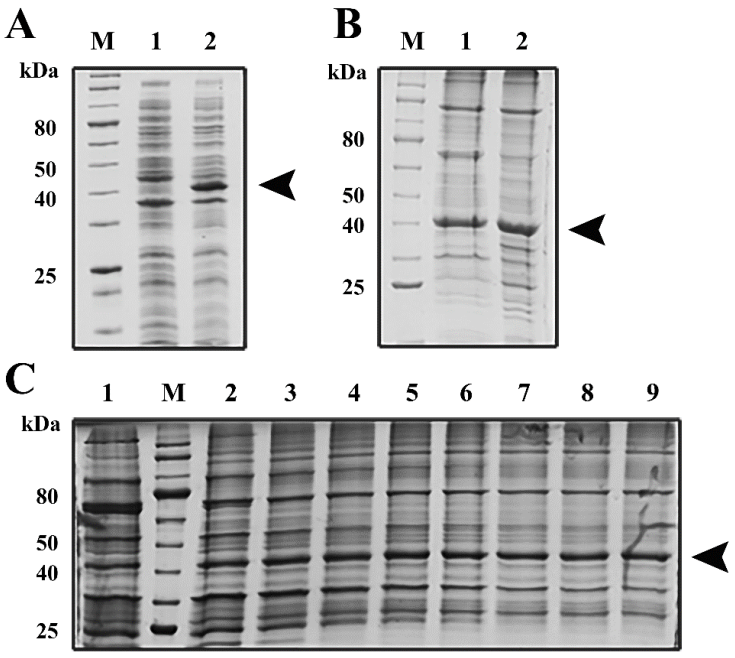

Figure 53. SDS-PAGE gels showing fusion protein CnR2-E.

A) M- protein marker, 1- uninduced Rosetta cells, 2- induced Rosetta cells overexpressing CnR2-E (~36 kDa). B) M- protein marker, 1- supernatant after Ni-NTA chromatography and concentration, 2- pellet after Ni-NTA chromatography and concentration. Approximately 50% of CnR2-E is soluble. C) 1-9- fractions 36-44 of HP Chelating Ni-NTA column (GE Healthcare), M- marker. Gel illustrates that CnR2-E is not enriched by chromatography, but was spread over many fractions.

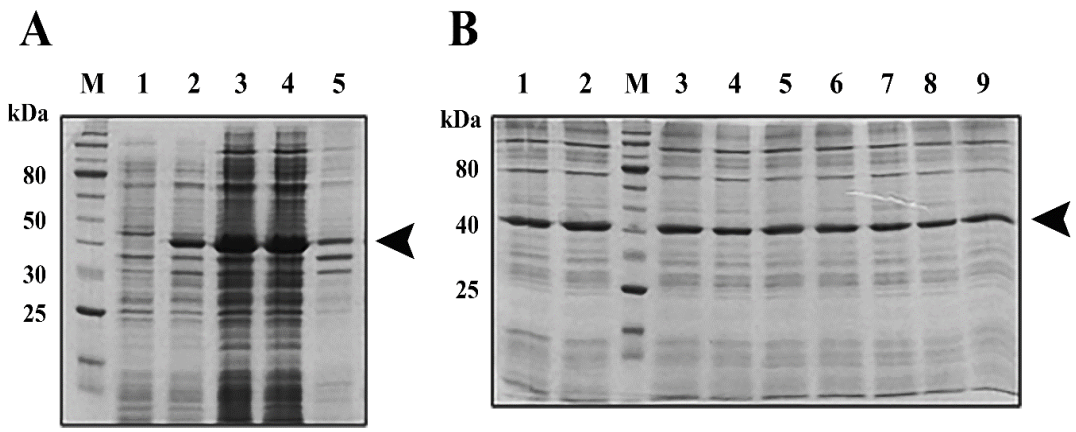

Figure 54. SDS-PAGE gels showing fusion protein CnR2-E-W1147A.
A) M- protein marker, 1- uninduced Rosetta cells, 2- induced Rosetta cells overexpressing CnR2-E-W1147A (~36 kDa), 3- supernatant of whole cell lysate, 4- pellet of whole cell lysate. The majority of CnR2-E-W1147A is soluble before purification. C) 1-9- fractions 54-62 of a HP Chelating Ni-NTA column (GE Healthcare), M- marker. Gel illustrates that CnR2-E-W1147A was not enriched by chromatography, but was spread over many fractions

CnR2-F

The construct, CnR2-F, was created from cDNA nucleotides 3022-3930 of the *C. neoformans* H99 Ssk1 gene (Figure 55 (pg. 105)). The final 324 amino acid fusion protein had an N-terminal 10x His-tag, a calculated molecular mass of 35,532 Da and a theoretical isoelectric point of 9.43. CnR2-F was expressed in Rosetta cells at 37 °C (Figure 56, panel A (pg. 105)), ambient temperature (24-30 °C) and 16 °C. The protein was approximately 50% soluble at 37 °C, but improved to 75% solubility at ambient temperature and 16 °C. CnR2-F eluted with 600 mM imidazole from a hand-poured Ni-NTA column, and remained soluble after dialysis into a low-salt buffer. CnR2-F eluted from a Hi-Trap Ni-NTA (GE Healthcare) 5 mL column using the AKTA prime system, but the protein was spread through many fractions (Figure 56, panel B(pg. 105)). After concentrating and freezing the protein at -20 °C in 50 mM Tris pH 8.0, 100 mM KCl, 15 mM $MgCl_2$ and 10% glycerol, CnR2-F showed precipitation when thawed on ice.

Although relatively pure, the yield was low (0.32 mg/L). CnR2-F was not subjected to further purification attempts.

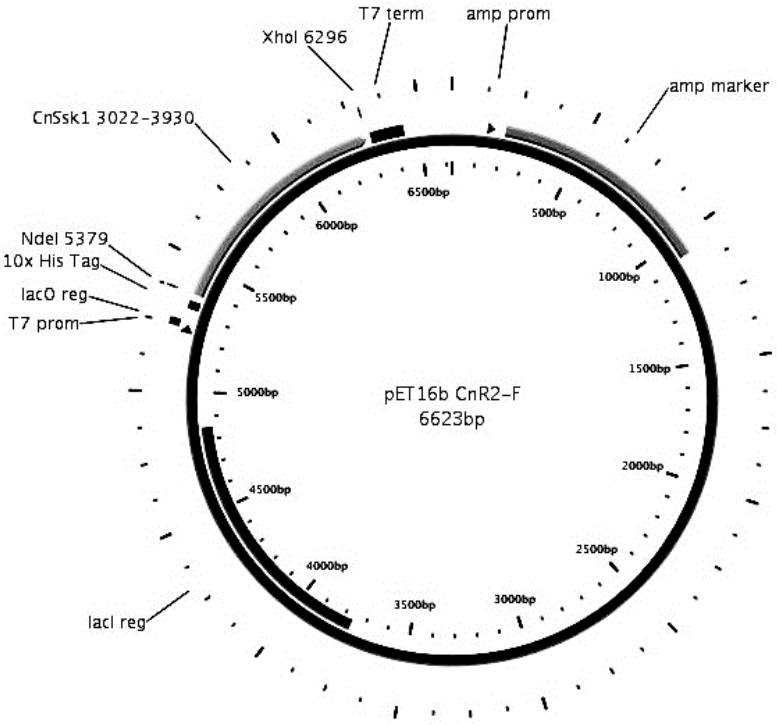

Figure 55. Plasmid map of construct CnR2-F.

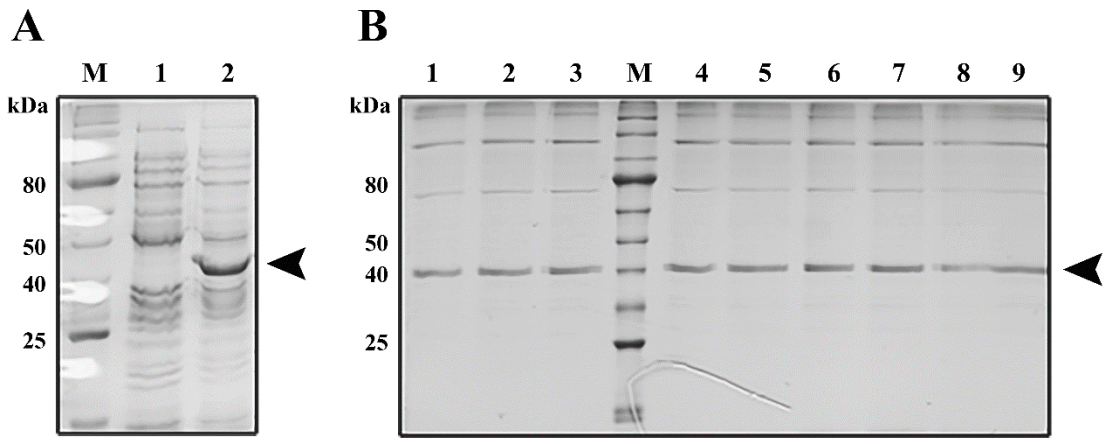

Figure 56. SDS-PAGE gels showing fusion protein CnR2-F.
A) M- marker, 1- uninduced Rosetta cells, 2- induced Rosetta cells overexpressing CnR2-F (~36 kDa). B) 1-9- fractions 36-44 of a HP Chelating Ni-NTA column (GE Healthcare), M- marker. Gel illustrates that CnR2-F was not enriched by chromatography, but was spread over many fractions.

CnR2-G

The construct, CnR2-G was created from cDNA nucleotides 1948-3927 of the *C. neoformans* H99 Ssk1 gene (Figure 57). The final 682 amino acid fusion protein had an N-terminal 10x His-tag, a calculated molecular mass of 74,127 Da and a theoretical isoelectric point of 9.89. CnR2-G was expressed in Rosetta cells at 37 °C, ambient temperature (24-30 °C) and 16 °C. The protein was mostly insoluble at 37 °C, but had improved solubility at ambient temperature and 16 °C. Protein expression in all temperatures was very low. Upon scale-up, CnR2-G did not bind Ni-NTA resin during chromatography (Figure 58 (pg. 107)). CnR2-G was not subjected to further purification attempts.

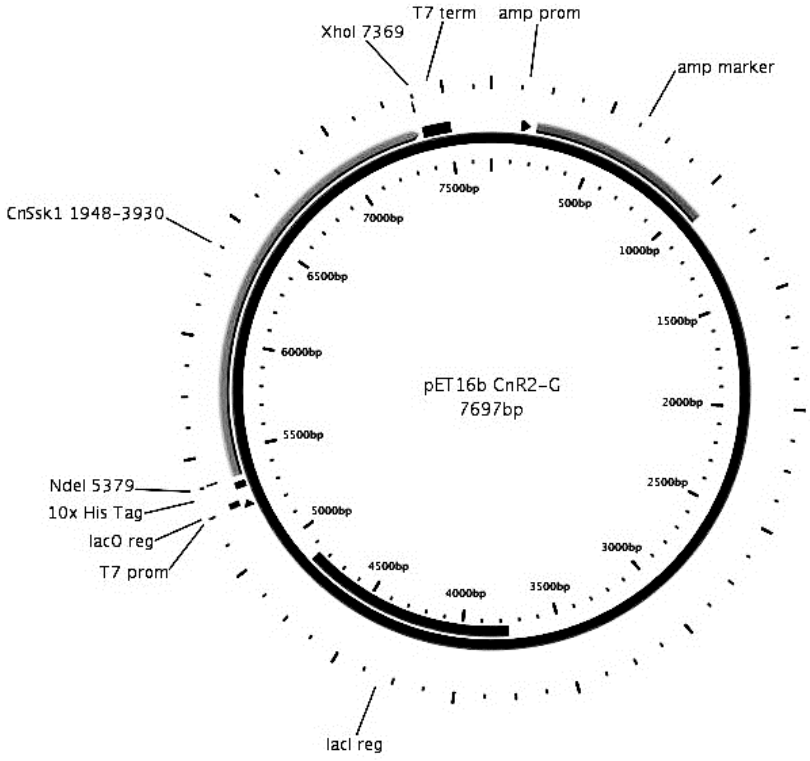

Figure 57. Plasmid map of construct CnR2-G.

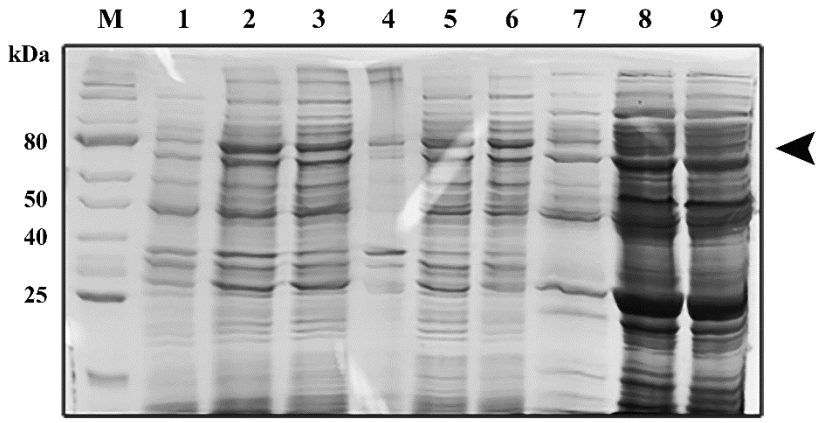

Figure 58. SDS-PAGE gel showing Ni-NTA purification attempt of CnR2-G.
M- protein marker, 1- uninduced Rosetta cells, 2- whole cell lysate of Rosetta cells at 16 °C showing the overexpression of CnR2-G (~74 kDa), 3- supernatant, 4- pellet, 5- flow-thru showing the presence of CnR2-G, 6- flow-thru showing the presence of CnR2-G, 7- 100 mM imidazole wash 1, 8- 100 mM imidazole wash 2, 9- 200 mM imidazole wash.

CnR2-H

The construct, CnR2-H was created from cDNA nucleotides 1948-3780 of the *C. neoformans* H99 Ssk1 gene (Figure 59 (pg. 108)). The final 633 amino acid fusion protein had an N-terminal 10x His-tag, a calculated molecular mass of 68,810 Da and a theoretical isoelectric point of 10.11. Due to its similarity to CnR2-G and CnR2-I, expression studies were not done on CnR2-H.

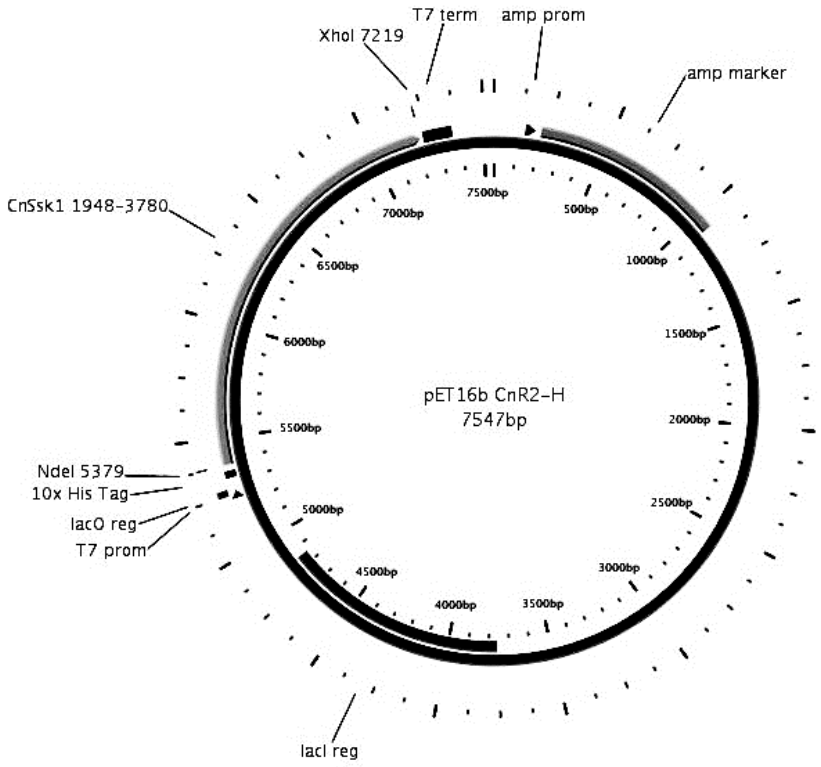

Figure 59. Plasmid map of construct CnR2-H.

CnR2-I

The construct, CnR2-I was created from cDNA nucleotides 1948-3573 of the *C. neoformans* H99 Ssk1 gene (Figure 60 (pg. 109)). The final 564 amino acid fusion protein had an N-terminal 10x His-tag, a calculated molecular mass of 61,571 Da and a theoretical isoelectric point of 9.94. CnR2-I was expressed in Rosetta cells at 37 °C and 16 °C. The protein was completely insoluble at 16 °C (Figure 61 (pg. 109)). CnR2-I was not subjected to further purification attempts.

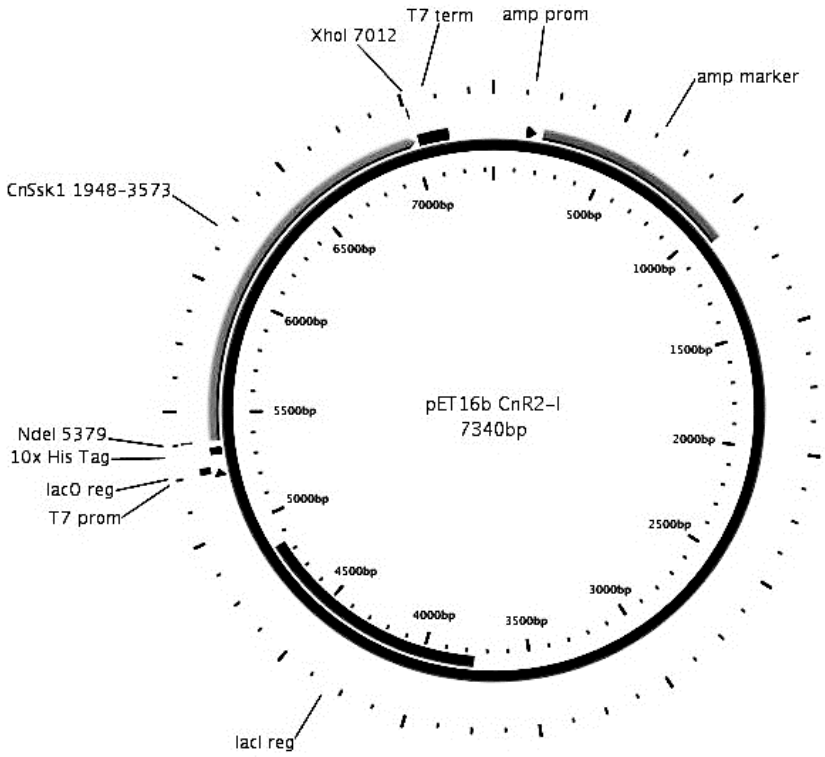

Figure 60. Plasmid map of construct CnR2-I.

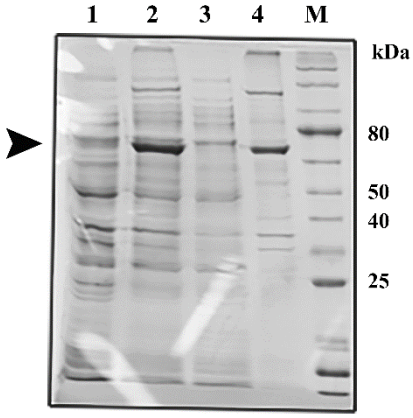

Figure 61. SDS-PAGE gel showing fusion protein CnR2-I.
1- uninduced Rosetta cells, 2- induced Rosetta cells overexpressing CnR2-I (~62 kDa), 3- supernatant of whole cell lysate at 16 °C, 4- pellet of whole cell lysate at 16 °C, M- protein marker. CnR2-I was insoluble.

CnR2-J

The construct, CnR2-J was created from cDNA nucleotides 3022-3780 of the *C. neoformans* H99 Ssk1 gene (Figure 62 (pg. 110)). The final 262 amino acid fusion

protein had a C-terminal 6x His-tag, a calculated molecular mass of 28,759 Da and a theoretical isoelectric point of 9.82. CnR2-J was overexpressed in Rosetta cells at 37 °C (Figure 63, panel A (pg. 111)), ambient temperature and 16 °C. Solubility was greatest at 16 °C, so a scale-up culture was grown and purified by nickel and cobalt affinity chromatography. Nickel gave better separation, although the protein was not enriched by chromatography; it was spread out over approximately 20 fractions. Despite this, the fractions were pooled, concentrated and subjected to size-exclusion chromatography which did not further purify the sample (Figure 63, panel B (pg. 111)). Despite the remaining impurities, CnR2-J was subjected to a phosphotransfer assay with CnYpd1 but did not display any activity.

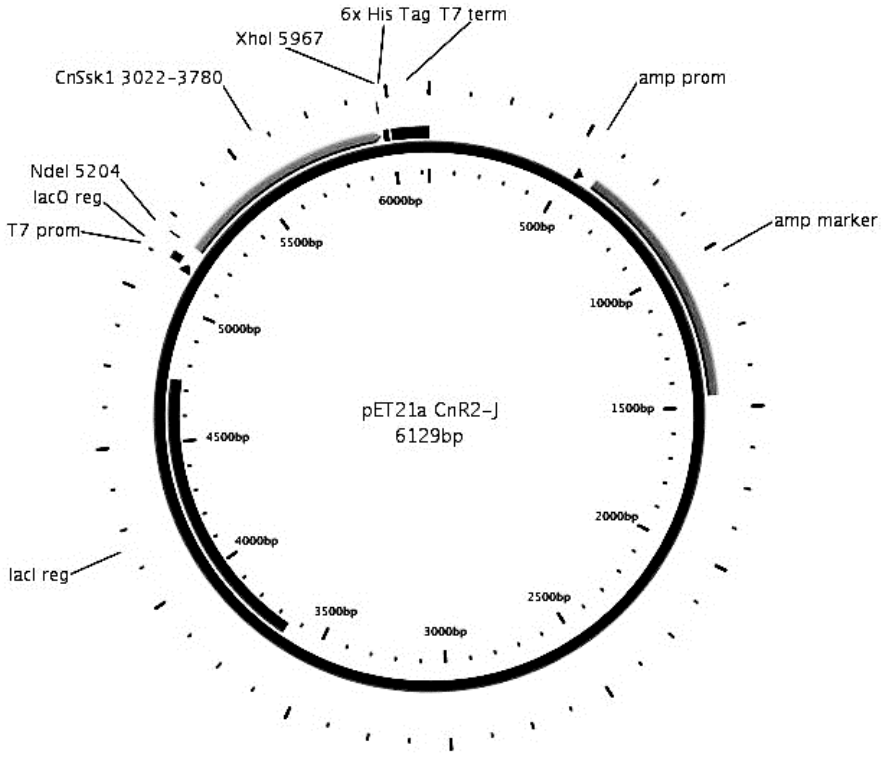

Figure 62. Plasmid map of construct CnR2-J.

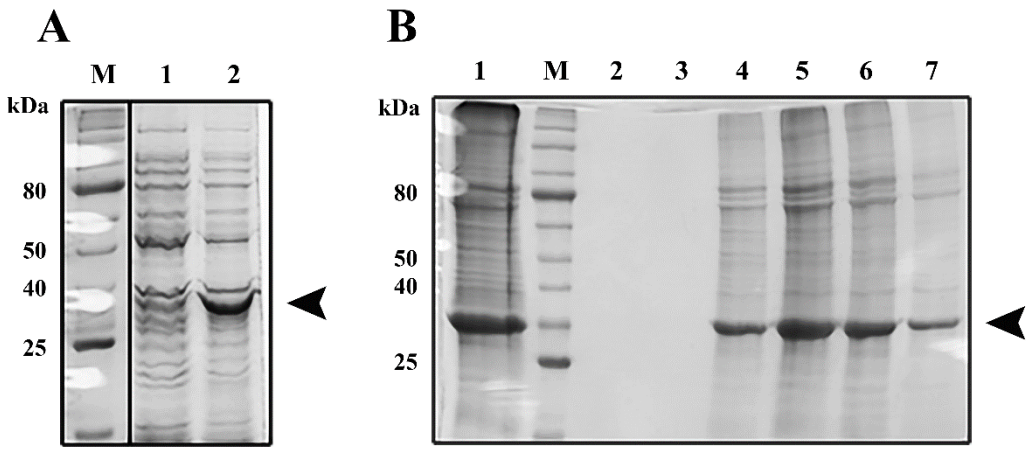

Figure 63. SDS-PAGE gels showing fusion protein CnR2-J.
A) M- marker, 1- uninduced Rosetta cells, 2- induced Rosetta cells overexpressing CnR2-J (~29 kDa). B) 1- size exclusion chromatography load, M- protein marker, 2-7- fractions 18-23 of size exclusion chromatography column. Gel illustrates that CnR2-J is not significantly purified by size exclusion chromatography after Ni-NTA affinity chromatography.

CnR2-K

The construct, CnR2-K was created from cDNA nucleotides 3022-3573 of the *C. neoformans* H99 Ssk1 gene (Figure 64 (pg. 112)). The final 193 amino acid fusion protein had a C-terminal 6x His-tag, a calculated molecular mass of 21,521 Da and a theoretical isoelectric point of 9.17. CnR2-K was expressed in Rosetta cells at 37 °C (Figure 65 (pg. 112)), ambient temperature, and 16 °C. The majority of the protein was insoluble at all temperatures.

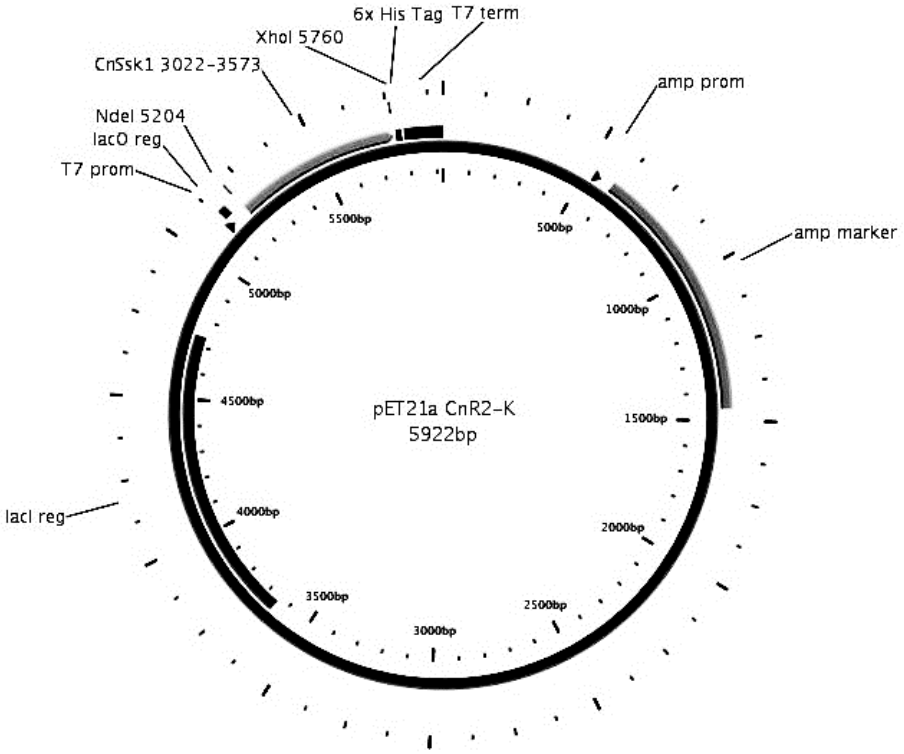

Figure 64. Plasmid map of construct CnR2-K.

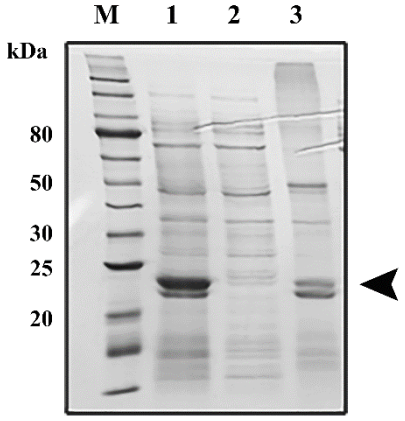

Figure 65. SDS-PAGE gel showing fusion protein CnR2-K.
M- marker, 1- induced Rosetta cells overexpressing CnR2-K (~22 kDa), 3- supernatant of whole cell lysate, 4- pellet of whole cell lysate. CnR2-K was insoluble.

CnR2-L

The construct, CnR2-L was created from cDNA nucleotides 1948-3780 of the *C. neoformans* H99 Ssk1 gene (Figure 66 (pg. 113)). The final 620 amino acid fusion

protein had a C-terminal 6x His-tag, a calculated molecular mass of 67,354 Da and a theoretical isoelectric point of 10.07. CnR2-L was expressed in Rosetta cells at 37 °C (Figure 67), ambient temperature, and 16 °C. The majority of the protein was insoluble at all temperatures.

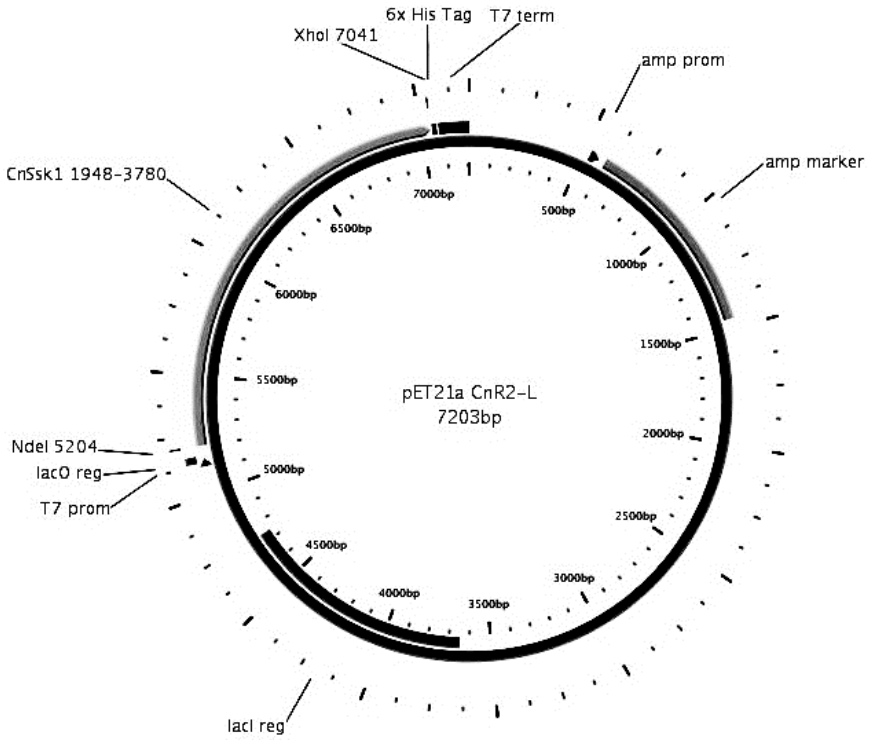

Figure 66. Plasmid map of construct CnR2-L.

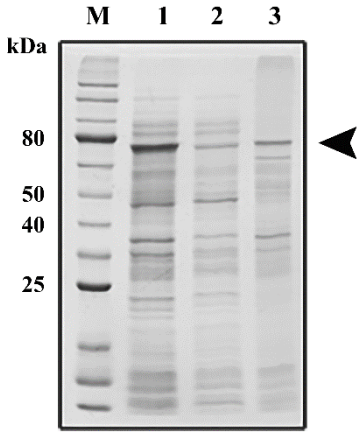

Figure 67. SDS-PAGE gel showing fusion protein CnR2-L.
M- marker, 1- induced Rosetta cells overexpressing CnR2-L (~67 kDa), 3- supernatant of whole cell lysate at 37 °C, 4- pellet of whole cell lysate at 37 °C. CnR2-L was equally insoluble at all temperatures.

CnR2-M

The construct, CnR2-M was created from cDNA nucleotides 1948-3573 of the *C. neoformans* H99 Ssk1 gene (Figure 68). The final 551 amino acid fusion protein had a C-terminal 6x His-tag, a calculated molecular mass of 60,116 Da and a theoretical isoelectric point of 9.90. CnR2-M was expressed in Rosetta cells at 37 °C and 16 °C. The protein was completely insoluble at 16 °C (Figure 69 (pg. 115)). CnR2-M was not subjected to further purification attempts.

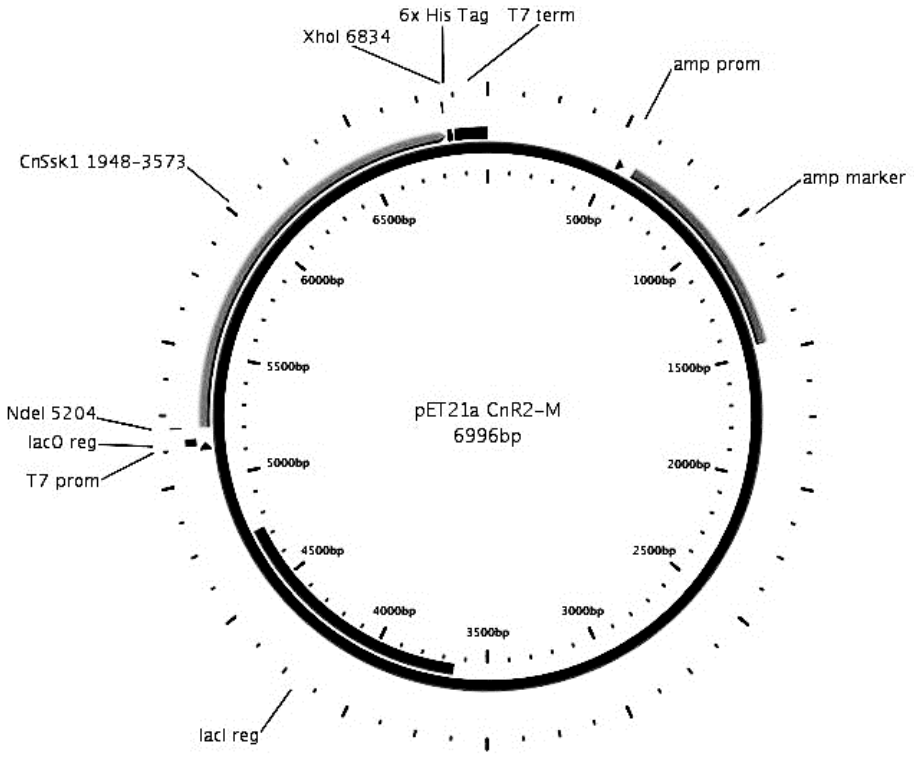

Figure 68. Plasmid map of construct CnR2-M.

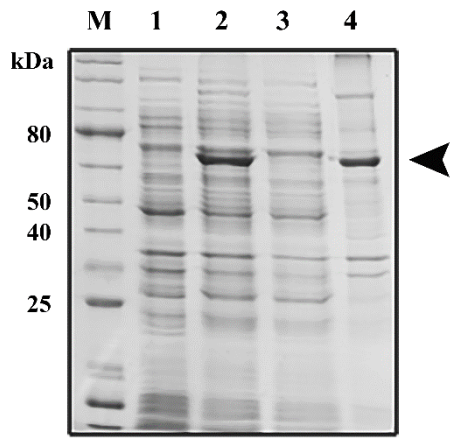

Figure 69. SDS-PAGE gel showing fusion protein CnR2-M.
M- marker, 1- uninduced Rosetta cells, 2- induced Rosetta cells overexpressing CnR2-M (~60 kDa), 3- supernatant of whole cell lysate, 4- pellet of whole cell lysate. CnR2-M was insoluble.

Discussion

In total, 14 attempts to purify CnR2 to crystallization standards were made. Overall, the factors that improved solubility were the presence of the 135-amino acid C-terminal tail, the presence of a His-tag, phosphate buffer, salt, and the combination of glycerol and Triton X-100. The proteins that made it through multiple purification steps, however, were not active in phosphotransfer assays (data not shown). It is likely that the protein's inactivity was due to insolubility or misfolding and should not be interpreted as evidence that CnSsk1 does not receive a phosphoryl group from CnYpd1. It could be that CnR2 is inactive but full length CnSsk1 is the active form of the protein. It is also possible that using yeast or insect cells to express CnSsk1 constructs would be more successful than using *E. coli* as the expression vector.

Experimental Section

Construction of vectors

The construction of CnR2-B consisted of PCR amplification of the desired nucleotides from *C. neoformans* cDNA (5a) followed by TOPO cloning directly into an expression vector. The construction of plasmids CnR2 C-M was carried out by PCR amplification from *C. neoformans* cDNA (5a) followed by TOPO-TA cloning into an intermediate vector, restriction digest, and ligation into an expression vector (Table 7 – Table 8).

Table 7. *C. neoformans* Ssk1-R2 construct oligonucleotides used in PCR
(For more information, see Appendix B)

Oligo	Description		Sequence	
AW727	CnR2-B 5' primer	5'	CACCATGAAGAATGCTAAAGTCG	3'
AW728	CnR2-B 3' primer	5'	ATAGGTCTTTGAGGGCGTAATG	3'
AW729	CnR2-C, D, E 5' primer	5'	GCGCATATGGTCGATGTTGTGGTGCCGCCC	3'
AW730	CnR2-C 3' primer	5'	CTGCCCGGGGGTATCGGAGCTCTTCCATCG	3'
AW731	CnR2-D 3' primer	5'	ATACCCGGGTGGGGGAGGAGCCGGATAG	3'
AW783	CnR2-E 3' primer	5'	CAAAGGATCCTTATGGGGGAGGAGCCGG	3'
AW903	CnR2-F, J, K 5' primer	5'	GTGGTGCATATGATCAACGTGC	3'
AW904	CnR2-F, G 3' primer	5'	CTTCCGCTCGAGCGGTCATG	3'
AW905	CnR2-G, H, I, L, M 5' primer	5'	TCCACCCATATGTTGCGACAGG	3'
AW906	CnR2-H 3' primer	5'	GAAGACCTCGAGTCATGTCTTGTTC	3'
AW907	CnR2-I 3' primer	5'	CAAGCGACTCGAGTCACTGTTGAG	3'
AW908	CnR2-J, L 3'e primer	5'	GACATCCTCGAGTGTCTTGTTCAG	3'
AW909	CnR2-K, M 3' primer	5'	CGACCTCTCGAGCTGTTGAGGG	3'
AW836	CnR2-E D1058A 5' primer	5'	CCATCTGATTCTGATGGCTATCCAATTGCCCGTCA	3'
AW837	CnR2-E D1058A 3' primer	5'	TGACGGGCAATTGGATAGCCATCAGAATCAGATGG	3'
AW869	CnR2-E W1147A 5' primer	5'	GACCAAGCCTGTGTCTTTGAAAGCGTTGGACAAAAAGATT	3'
AW870	CnR2-E W1147A 3' primer	5'	AATCTTTTTGTCCAACGCTTTCAAAGACACAGGCTTGGTC	3'

Table 8. PCR and plasmid construction details

Construct	PCR- DNA polymerase	PCR annealing temp	TOPO-TA intermediate	5' restriction site	3' restriction site	Expression vector	mutants created
B	*Pfx*	51 °C	no	n/a	n/a	pET101/D-TOPO	n/a
C	platinum *Taq*	64 °C	yes	NdeI	SmaI	pET-CYB2	n/a
D	platinum *Taq*	64 °C	yes	NdeI	SmaI	pET-CYB2	n/a
E	platinum *Taq*	64 °C	yes	NdeI	BamHI	pET16b	D1058A, W1147A
F	Emerald *Taq*	50 °C	yes	NdeI	XhoI	pET16b	n/a
G	Emerald *Taq*	50 °C	yes	NdeI	XhoI	pET16b	n/a
H	Emerald *Taq*	50 °C	yes	NdeI	XhoI	pET16b	n/a
I	Emerald *Taq*	50 °C	yes	NdeI	XhoI	pET16b	n/a
J	Emerald *Taq*	50 °C	yes	NdeI	XhoI	pET21a	n/a
K	Emerald *Taq*	50 °C	yes	NdeI	XhoI	pET21a	n/a
L	Emerald *Taq*	50 °C	yes	NdeI	XhoI	pET21a	n/a
M	Emerald *Taq*	50 °C	yes	NdeI	XhoI	pET21a	n/a

Transformation

Transformations were carried out by incubating nanogram quantities of plasmid DNA with competent *E. coli* cells (50-250 µL) on ice for 30 minutes followed by a 30-45 second heat-shock at 42 °C. After cooling cells on ice for 2-5 minutes, LB or SOC was added to the reaction up to 500-1000 µL and cells were incubated for 60 minutes, 200 rpm, 37 °C. Cells were plated on LB + antibiotic and incubated over night at 37 °C.

Expression and solubility

All constructs were initially tested for expression in *E. coli* Rosetta cells at 37 °C. Rosetta cells were chosen because the CnR2 gene contains a total of 30 rare codons[21]. The extra tRNA in Rosetta cells afforded coverage of 77% of the rare codons compared with BL21-RIL cells, which only covered 33%. LB + antibiotic was inoculated with a 1% volume saturated liquid culture and shaken at 200 rpm until OD_{600} ~ 0.6. Cells were induced with 0.1-1 mM IPTG and grown for at least 3 hours. Uninduced and induced cell aliquots were normalized for OD_{600} and run side by side on SDS-PAGE gels to evaluate the presence (or absence) of an overexpressed protein band of the expected size. Expression in SHuffle cells (NEB) was attempted for the intein-CBD-tagged constructs, but this was unsuccessful at 30 °C.

In order to assess solubility, cells were grown in an identical way to expression until induction. After induction, cells were grown at 37 °C (~3 hours), ambient temperature (~8 hours) or 16 °C (~20 hours). Cells were lysed using French Press and cell lysate was separated into supernatant and pellet. Aliquots were run side by side on SDS-PAGE gels to compare the proportion of the overexpressed band in the supernatant (soluble) and pellet (insoluble).

Purification

French press was used as the cell lysis method for all constructs. For intein-CBD-tagged constructs (C-D), the lysis buffer was 50 mM sodium phosphate, pH 8.0, 500 mM NaCl, 0.1 mM EDTA, 0.1% Triton X-100 and 5% glycerol. For His-tagged constructs (E-M), lysis buffer was 20-50 mM sodium phosphate, pH 8.0, 300 mM NaCl, 1 mM βME and 5 mM imidazole. Just prior to lysis, DNase, RNase and 1X protease

inhibitor were added. After lysis, cell lysate was clarified for 1 hour at ~25000 x g, 4 °C.

The first purification step for intein-CBD-tagged constructs (C-D) was chitin affinity chromatography (IMPACT system, NEB). Cell lysate supernatant from 1-L scale up preps was added to a 3-4 mL chitin column pre-equilibrated in lysis buffer. The flow through was discarded and the column was washed with 10 CV of lysis buffer and 10 CV of cleavage buffer (50 mM sodium phosphate pH 8.0, 100 mM NaCl, 0.1 mM EDTA and 5% glycerol). The column was left to incubate overnight in cleavage buffer + 30 mM βME at 4 °C. Cleaved protein was eluted with cleavage buffer and collected in 1 mL fractions.

Nickel or cobalt affinity columns (hand-poured or HP Chelating (GE Healthcare)) were performed as the first purification step for all His-tagged proteins (constructs E-M). After clarification, cell lysate was applied to pre-equilibrated columns. When gravity columns were used, a wash step with lysis buffer + 100 mM imidazole was used before elution with lysis buffer + 600 mM imidazole. When 5-mL HP chelating columns (GE Healthcare) were used with the AKTA prime system, a gradient from 5 mM imidazole to 600 mM imidazole in lysis buffer was used with a flow rate of 1 mL/min.

Size exclusion chromatography was generally attempted as a second purification step. Proteins were concentrated to approximately 1 mL and filtered through 0.45 µm filters before being added to a 100-mL column of Sephacryl-100 resin at 4 °C. Various buffer components were used but in general, the buffer was pH 7-8 and included 100-

150 mM salt along with 1 mM EDTA and 1 mM βME. Other additions were 5-15 mM $MgCl_2$ or 5-10% glycerol.

Occasionally cation exchange was performed as a second purification step. Protein was dialyzed into 50 mM HEPES pH 7.6, 5% glycerol and 1 mM βME. Protein was loaded onto a 5 mL HiTrap SP column (GE Healthcare) and washed with buffer. A gradient of 0-1 M NaCl was applied over 90 mL at 1 mL/min flow rate.

In the case of CnR2-D, a phenyl sepharose column was attempted as a second purification step. Protein (in lysis buffer) was added to a 2-mL pre-equilibrated phenyl sepharose column. The column was washed with lysis buffer and elution fractions were collected as salt was decreased step-wise from 500 mM to 0 mM.

Table 9. Summary of protein purification.

construct	expression	solubility	affinity chromatography	other chromatography	phosphotransfer assay
B	no	n/a	n/a	n/a	n/a
C	yes	yes	chitin	cation exchange, gel-filtration	n/a
D	yes	yes	chitin	cation exchange, phenyl sepharose, gel-filtration	not active with CnYpd1
E	yes	yes	nickel, cobalt	cation exchange, gel-filtration	n/a
F	yes	yes	nickel	n/a	n/a
G	yes	yes	nickel	n/a	n/a
H	n/a	n/a	n/a	n/a	n/a
I	yes	no	n/a	n/a	n/a
J	yes	yes	nickel, cobalt	gel-filtration	not active with CnYpd1
K	yes	no	n/a	n/a	n/a
L	yes	no	n/a	n/a	n/a
M	yes	no	n/a	n/a	n/a

References

[1] Denning, D. W., and Bromley, M. J. (2015) How to bolster the antifungal pipeline, *Science 347*, 1414-1416.

[2] Park, B. J., Wannemuehler, K. A., Marston, B. J., Govender, N., Pappas, P. G., and Chiller, T. M. (2009) Estimation of the current global burden of cryptococcal meningitis among persons living with HIV/AIDS, *Aids 23*, 525-530.

[3] Imwidthaya, P., and Poungvarin, N. (2000) Cryptococcosis in AIDS, *Postgrad Med J 76*, 85-88.

[4] McDonald, T., Wiesner, D. L., and Nielsen, K. (2012) Cryptococcus, *Curr. Biol. 22*, R554-555R555.

[5] Rappleye, C. A., and Goldman, W. E. (2008) Fungal stealth technology, *Trends Immunol. 29*, 18-24.

[6] Kozubowski, L., and Heitman, J. (2012) Profiling a killer, the development of *Cryptococcus neoformans*, *FEMS Microbiol. Rev. 36*, 78-94.

[7] Shor, E., and Chauhan, N. (2015) A case for two-component signaling systems as antifungal drug targets, *PLOS Pathog. 11*, e1004632.

[8] Bahn, Y.-S., Kojima, K., Cox, G. M., and Heitman, J. (2006) A unique fungal two-component system regulates stress responses, drug sensitivity, sexual development, and virulence of *Cryptococcus neoformans*, *Mol. Biol. Cell 17*, 3122-3135.

[9] Bahn, Y.-S., Kojima, K., Cox, G. M., and Heitman, J. (2005) Specialization of the HOG pathway and its impact on differentiation and virulence of *Cryptococcus neoformans*, *Mol Biol Cell 16*, 2285-2300.

[10] Bahn, Y.-S., Geunes-Boyer, S., and Heitman, J. (2007) Ssk2 mitogen-activated protein kinase kinase kinase governs divergent patterns of the stress-activated Hog1 signaling pathway in *Cryptococcus neoformans*, *Euk. Cell 6*, 2278-2289.

[11] Bahn, Y.-S. (2008) Master and commander in fungal pathogens: the two-component system and the HOG signaling pathway, *Euk. Cell 7*, 2017-2036.

[12] Bahn, Y.-S., and Jung, K.-W. (2013) Stress signaling pathways for the pathogenicity of *Cryptococcus*, *Euk. Cell 12*, 1564-1577.

[13] Rice, P., Longden, I., and Bleasby, A. (2000) EMBOSS: the European molecular biology open software suite, *Trends Genet. 16*, 276-277.

[14] Huang, X., and Miller, W. (1991) A time-efficient, linear-space local similarity algorithm, *Adv Appl Math 12*, 337-357.

[15] Waterhouse, A. M., Procter, J. B., Martin, D. M. A., Clamp, M., and Barton, G. J. (2009) Jalview Version 2—a multiple sequence alignment editor and analysis workbench, *Bioinformatics 25*, 1189-1191.

[16] Larkin, M. A., Blackshields, G., Brown, N. P., Chenna, R., McGettigan, P. A., McWilliam, H., Valentin, F., Wallace, I. M., Wilm, A., Lopez, R., Thompson, J. D., Gibson, T. J., and Higgins, D. G. (2007) Clustal W and Clustal X version 2.0, *Bioinformatics 23*, 2947-2948.

[17] Kelley, L. A., Mezulis, S., Yates, C. M., Wass, M. N., and Sternberg, M. J. E. (2015) The Phyre2 web portal for protein modeling, prediction and analysis, *Nat. Protocols 10*, 845-858.

[18] Altschul, S. F., Gish, W., Miller, W., Myers, E. W., and Lipman, D. J. (1990) Basic local alignment search tool, *J Mol Biol 215*, 403-410.

[19] Tung, C. H., Huang, J. W., and Yang, J. M. (2007) Kappa-alpha plot derived structural alphabet and BLOSUM-like substitution matrix for rapid search of protein structure database, *Genome Biol 8*, R31.

[20] Berman, H. M., Battistuz, T., Bhat, T. N., Bluhm, W. F., Bourne, P. E., Burkhardt, K., Feng, Z., Gilliland, G. L., Iype, L., Jain, S., Fagan, P., Marvin, J., Padilla, D., Ravichandran, V., Schneider, B., Thanki, N., Weissig, H., Westbrook, J. D., and Zardecki, C. (2002) The Protein Data Bank, *Acta Cryst. D58*, 899-907.

[21] Ng, E. (2001) Rare Codon Caltor.

Appendix A: Co-crystallization of Ssk1-R2^{W638A} and Ypd1^{G68Q}

Introduction

All HPt proteins with a known structure have a similar fold; at their core is a 4-α-helix bundle[1-4]. This core 4-helix bundle is structurally similar to the α-helical dimerization domain of HKs that contains the phosphorylatable histidine[5]. Histidine kinase and HPt protein domains show a low amino acid sequence homology, but the area surrounding the phospho-accepting histidine is widely conserved. The importance of a small residue at the n+4 position relative to the phosphorylatable histidine in HPt domains is evident from a comprehensive sequence alignment (data not shown) of HPt domains. A glycine or serine is conserved in approximately 99% of sequences in the NCBI database for the HPt Superfamily[6, 7].

A previous study of the *S. cerevisiae* Sln1-Ypd1-Ssk1 signaling pathway *in vitro* led to the elucidation of a common binding surface on Ypd1 for the upstream and downstream response regulators[8, 9]. Mutations of highly conserved residues in Ypd1 were shown to alter phosphotransfer activity[10]. A mutant that contained an n+4 glycine substitution with a glutamine residue (G68Q) showed a steady-state level of phosphorylation of approximately 30% of wild-type Ypd1 while maintaining a phosphorylated half-life comparable to wild-type Ypd1. In addition, this mutant also exhibited reduced phosphotransfer capability to the upstream and downstream response regulator receiver domains, Sln1-R1 and Ssk1-R2[10]. The role of this conserved glycine residue in this position has remained an open question. In order to visualize the impact of the glutamine substitution in the n+4 position, I describe methods that led to the successful co-crystallization of Ssk1-R2-W638A with Ypd1-G68Q.

Co-crystallization of Ssk1-R2^{W638A} and Ypd1^{G68Q}

Diffraction-quality crystals were produced in 1:1 µL hanging drops in a 24-well hanging drop screens around conditions similar to Ssk1-R2-W638A and Ypd1 as described in Chapter 3. In addition, crystals were grown under similar conditions in an attempt to get the BeF_3^- -activated structure (Figure 70). Optimal cryo conditions must be found to obtain high resolution data to solve the crystal structures.

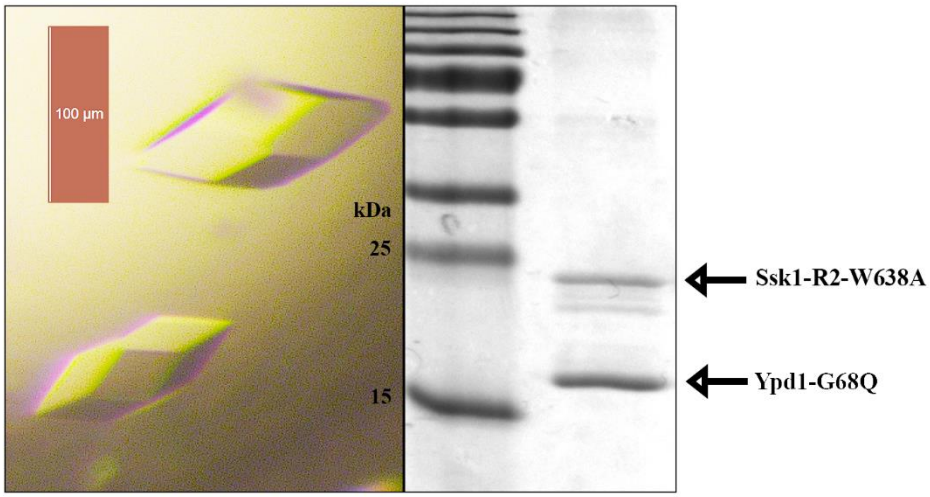

Figure 70. Ssk1-R2^{W638A}/Ypd1^{G68Q} crystal.
Photograph of Ssk1-R2^{W638A}/Ypd1^{G68Q} crystal (left panel) and Coomassie-stained 15% SDS-PAGE gel of a dissolved crystal, verifying that the crystals were composed of both proteins (right panel). Coomassie gel courtesy of Clay Foster.

Experimental Section

Protein Purification

Ypd1-G68Q was purified using an identical protocol to WT Ypd1 by ammonium sulfate precipitation, ion exchange chromatography and size-exclusion chromatography as published in Xu et al.[11] and described in Chapter 3.

Ssk1-R2-W638A was purified using the IMPACT (NEB) system as described in Chapter 2. It was followed by size-exclusion chromatography (Sephadex® G-75, Sephacryl® S-100 or S-200) in 20 mM Tris pH 8, 100 mM NaCl and 1% glycerol.

Crystallization and data collection

To produce apo-crystals, equimolar amounts of Ssk1-R2-W638A and Ypd1-G68Q were combined, co-concentrated to 12 mg/mL in 20 mM Tris pH 8.0, 75-100 mM NaCl and 1% glycerol. Hanging drop vapor diffusion 24-well trays were set up with well solutions of 0.1M CAPS pH 10.5, 1.15-1.2 M NaH_2PO_4, 0.7-0.8 M K_2HPO_4 and 0.2 M $LiSO_4$. To attempt to produce BeF^{3-}-activated crystals, equimolar amounts of Ssk1-R2-W638A and Ypd1-G68Q were combined, co-concentrated to 11.7 mg/mL in 20 mM Tris pH 8.0, 75-100 mM NaCl and 1% glycerol, 15 mM $MgCl_2$, 5 mM $BeCl_2$ and 35 mM NaF. Hanging drop vapor diffusion 24-well trays were set up in an identical way to the apo crystals. Attempts to optimize cryo conditions were unsuccessful, but the most promising results were obtained using 30% or saturated sucrose in mother liquor compared to varying amounts of high salt, glycerol, ethylene glycol, PEG 3350, lithium sulfate, glucose, trehalose, CryoProtX (Molecular Dimensions), Krytox oil, or Al's oil. A room temperature mount collected on our home X-ray source (1.541 Å Cu Kα rotating anode with Pilatus 200K detector (Rigaku)) showed that the crystals diffracted from 3.5-4.0 Å (Figure 71 (pg. 126)).

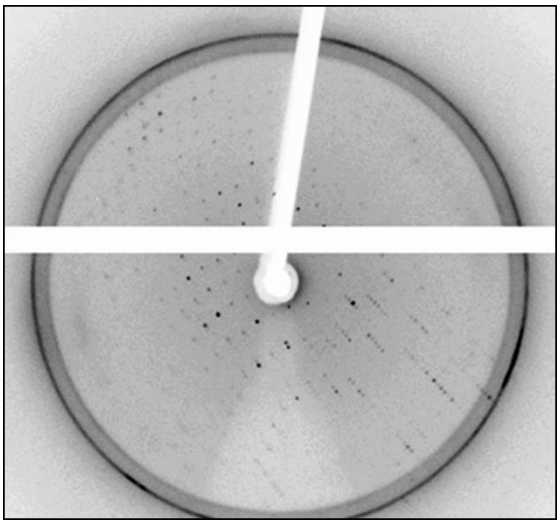

Figure 71. Diffraction to ~3-4 Å of the co-crystal of Ssk1-R2^{W638A}/Ypd1^{G68Q}.

Future Directions

The next steps that need to be taken in this project are to optimize cryo conditions, obtain data to a minimum of 3.0 Å and solve the crystal structure using molecular replacement. The information will elucidate the structural basis for the loss in phosphotransfer efficiency observed between Ypd1 and its cognate response regulators that cannot be explained by preliminary binding data. This project has been conducted in collaboration with, and will be completed by Clay Foster, West Lab.

References

[1] Xu, Q., and West, A. H. (1999) Conservation of structure and function among histidine-containing phosphotransfer (HPt) domains as revealed by the crystal structure of YPD1, *J. Mol. Biol. 292*, 1039-1050.

[2] Sugawara, H., Kawano, Y., Hatakeyama, T., Yamaya, T., Kamiya, N., and Sakakibara, H. (2006) Crystal structure of the histidine-containing phosphotransfer protein ZmHP2 from maize, *Protein Sci. 14*, 202-208.

[3] Song, H. K., Lee, J. Y., Lee, M. G., Min, J. M. K., Yang, J. K., and Suh, S. W. (1999) Insights into eukaryotic multistep phosphorelay signal transduction revealed by the crystal structure of Ypd1p from *Saccharomyces cerevisiae*, *J. Mol. Biol. 293*, 753-761.

[4] Kato, M., Mizuno, T., Shimizu, T., and Hakoshima, T. (1999) Refined structure of the histidine-containing phosphotransfer (HPt) domain of the anaerobic sensor kinase ArcB from *Escherichia coli* at 1.57 Å resolution, *Acta Cryst. D55*, 1842-1849.

[5] Yamada, S., Akiyama, S., Sugimoto, H., Kumita, H., Ito, K., Fujisawa, T., Nakamura, H., and Shiro, Y. (2006) The signaling pathway in histidine kinase and the response regulator complex revealed by X-ray crystallography and solution scattering, *J. Mol. Biol. 362*, 123-139.

[6] Finn, R. D., Mistry, J., Tate, J., Coggill, P., Heger, A., Pollington, J. E., Gavin, O. L., Gunasekaran, P., Ceric, G., Forslund, K., Holm, L., Sonnhammer, E. L. L., Eddy, S. R., and Bateman, A. (2010) The Pfam protein families database, *Nucleic Acids Res. 38*, D211-D222.

[7] Pruitt, K. D., Tatusova, T., Brown, G. R., and Maglott, D. R. (2012) NCBI Reference Sequences (RefSeq): current status, new features and genome annotation policy, *Nucleic Acids Res. 40*, D130-D135.

[8] Porter, S. W., and West, A. H. (2005) A common docking site for response regulators on the yeast phosphorelay protein YPD1, *Biochim. Biophys. Acta 1748*, 138-145.

[9] Porter, S. W., Xu, Q., and West, A. H. (2003) Ssk1p response regulator binding surface on histidine-containing phosphotransfer protein Ypd1p, *Euk. Cell 2*, 27-33.

[10] Janiak-Spens, F., and West, A. H. (2000) Functional roles of conserved amino acid residues surrounding the phosphorylatable histidine of the yeast phosphorelay protein YPD1, *Mol. Microbiol. 37*, 136-144.

[11] Xu, Q., Nguyen, V., and West, A. H. (1999) Purification, crystallization, and preliminary X-ray diffraction analysis of the yeast phosphorelay protein YPD1, *Acta Cryst. D55*, 291-293.

Appendix B: Table of West Lab primers, plasmids and cell strains

organism	protein	oligos	restriction sites	plasmid	storage strain	expression strain(s)
Cn	Ssk1-5' cDNA (2a)	n/a	n/a	pCR2.1 TOPO	OU689-DH5α	n/a
Cn	Ssk1-5' cDNA (2b)	n/a	n/a	pCR2.1 TOPO	OU690-DH5α	n/a
Cn	Ssk1-5' cDNA (5a)	AW902	for mid-DNA seq	pCR2.1 TOPO	n/a	n/a
Cn	Ssk1-3' cDNA (6a)	n/a	n/a	pCR2.1 TOPO	OU691-DH5α	n/a
Cn	Ssk1-3' cDNA (6b)	n/a	n/a	pCR2.1 TOPO	OU692-DH5α	n/a
Cn	Ssk1-R2-B	AW727, AW728	n/a	pl424	OU647-DH5α	OU645-Rosetta
Cn	Ssk1-R2-C	AW729, AW730	NdeI, SmaI	pl425	OU656-DH5α	OU654-Rosetta
Cn	Ssk1-R2-D	AW729, AW731	NdeI, SmaI	pl428	OU661-DH5α	OU662-Rosetta
Cn	Ssk1-R2-E	AW729, AW783	NdeI, BamHI	pl436	OU686-DH5α	OU687-Rosetta
Cn	Ssk1-R2-E-W1147A	AW869, AW870	NdeI, BamHI	pl449	OU721-DH5α	OU722-Rosetta
Cn	Ssk1-R2-F-TOPO	AW903, AW904	NdeI, XhoI	pl462	OU751-DH5α	n/a
Cn	Ssk1-R2-J-TOPO	AW903, AW908	NdeI, XhoI	pl463	OU752-DH5α	n/a
Cn	Ssk1-R2-K-TOPO	AW903, AW909	NdeI, XhoI	pl464	OU753-DH5α	n/a
Cn	Ssk1-R2-L-TOPO	AW905, AW908	NdeI, XhoI	pl465	OU754-TOP10	n/a
Cn	Ssk1-R2-G-TOPO	AW905, AW904	NdeI, XhoI	pl466	OU755-TOP10	n/a
Cn	Ssk1-R2-F	AW903, AW904	NdeI, XhoI	pl467	OU756-DH5α	OU757-Rosetta
Cn	Ssk1-R2-J	AW903, AW908	NdeI, XhoI	pl468	OU758-DH5α	OU759-Rosetta
Cn	Ssk1-R2-K	AW903, AW909	NdeI, XhoI	pl469	OU760-TOP10	OU761-Rosetta
Cn	Ssk1-R2-L	AW905, AW908	NdeI, XhoI	pl470	OU762-TOP10	OU763-Rosetta
Cn	Ssk1-R2-G	AW905, AW904	NdeI, XhoI	pl471	OU764-TOP10	OU765-Rosetta
Cn	Ssk1-R2-I-TOPO	AW905, AW907	NdeI, XhoI	pl472	OU766-TOP10	n/a
Cn	Ssk1-R2-M-TOPO	AW905, AW909	NdeI, XhoI	pl473	OU767-TOP10	n/a
Cn	Ssk1-R2-I	AW905, AW907	NdeI, XhoI	pl474	OU768-DH5α	OU769-Rosetta
Cn	Ssk1-R2-M	AW905, AW909	NdeI, XhoI	pl475	OU770-DH5α	OU771-Rosetta
Cn	Ssk1-R2-H-TOPO	AW905, AW906	NdeI, XhoI	pl520	n/a	n/a

Cn	Ssk1-R2-H	AW905, AW906	NdeI, XhoI	n/a	n/a	n/a
Sc	Ssk1-R2-D554N	AW741, AW742	NdeI, SmaI	pl429	OU663-DH5α	OU735-BL21 Star, OU664-BL21 Gold
Sc	Ssk1-R2-W638A	AW776, AW777	NdeI, SmaI	pl430	OU668-DH5α	OU738-BL21 Star, OU669-BL21 Gold
Sc	Ssk1-R2-Q650L	AW745, AW746	NdeI, SmaI	pl431	OU670-DH5α	OU737-BL21 Star, OU671-BL21 Gold
Sc	Ssk1-R2-G647Q	AW743, AW744	NdeI, SmaI	pl439	OU695-DH5α	OU736-BL21 Star, OU696-BL21 Gold
Sc	Ssk1-R2-V634S	AW786, AW787	NdeI, SmaI	pl445	OU709-DH5α	OU710-BL21 Star
Sc	Ssk1-R2-I518S	AW784, AW785	NdeI, SmaI	pl446	OU711-DH5α	OU712-BL21 Star
Sc	Ssk1-R2-W646A	AW860, AW861	NdeI, SmaI	pl447	OU713-DH5α	OU714-BL21 Star
Sc	Ssk1-R2-E645Q	AW778, AW779	NdeI, SmaI	pl448	OU715-DH5α	OU716-BL21 Star
Sc	Ssk1-R2-D554A	AW856, AW857	NdeI, SmaI	pl455	OU733-DH5α	OU734-BL21 Star
Sc	Ssk1-R2-L639S	AW858, AW859	NdeI, SmaI	pl457	OU741-DH5α	OU742-BL21 Star
Sc	Ssk1-R2-S612A	AW921, AW922	NdeI, SmaI	pl458	OU743-DH5α	OU744-BL21 Star
Sc	Ssk1-R2-T631A	AW923, AW924	NdeI, SmaI	pl459	OU745-DH5α	OU746-BL21 Star
Sc	Ssk1-R2-L636S	AW925, AW926	NdeI, SmaI	pl460	OU747-DH5α	OU748-BL21 Star
Sc	Ssk1-R2-N635A	AW854, AW855	NdeI, SmaI	pl461	OU749-DH5α	OU750-BL21 Star
Sc	Ssk1-R2-Q556A	AW1012, AW1013	NdeI, SmaI	pl483	OU781-DH5α	OU782-BL21 Star
Sc	Ssk1-R2-R524A	AW1014, AW1015	NdeI, SmaI	pl484	OU783-DH5α	OU784-BL21 Star
Sc	Ssk1-R2-H637A	AW984, AW985	NdeI, SmaI	pl485	OU785-DH5α	OU786-BL21 Star
Sc	Ssk1-R2-R524A-H637A	AW1014, AW1015, AW984, AW985	NdeI, SmaI	pl486	OU787-DH5α	OU788-BL21 Star
Sc	Ssk1-R2-K525A	AW1035, AW1036	NdeI, SmaI	pl493	OU798-DH5α	OU799-BL21 Star
Sc	Ssk1-R2-R524A-K525A	AW1014, AW1015, AW1035, AW1036	NdeI, SmaI	pl494	OU800-DH5α	OU801-BL21 Star

Sc	Ssk1-R2-R524A-K525A-H637A	AW1014, AW1015, AW984, AW985, AW1035, AW1036	NdeI, SmaI	pl495	OU804-DH5α	OU805-BL21 Star
Sc	Ssk1-R2-K525A-H637A	AW1035, AW1036, AW984, AW985	NdeI, SmaI	pl496	OU802-DH5α	OU803-BL21 Star

Cn= *C. neoformans*, Sc= *S. cerevisiae*

Appendix C: Discovery of anti-biofilm isocoumarins and isobenzofuranones from a microbial mat fungus

List of Abbreviations

NMR: Nuclear Magnetic Resonance

HRESIMS: High Resolution ElectroSpray Ionization Mass Spectrometry

DBE: Double Bond Equivalents

gCOSY: gradient COrrelation SpectroscopY: a two dimensional NMR experiment showing cross-peaks between neighboring protons

NOESY: Nuclear Overhauser Effect SpectroscopY: an NMR experiment showing correlations between protons within 6 Å from each other in space

HSQC: Heteronuclear Single Quantum Coherence/Correlation: a two-dimensional NMR experiment showing cross-peaks between protons and carbons connected by one bond

gHMBC: gradient Heteronuclear Multiple Bond Correlation: a two-dimensional NMR experiment showing cross-peaks between protons and carbons separated by two to three bonds

Introduction

Isocoumarins are a broad class of secondary metabolites produced by bacteria, plants and fungi. These metabolites and their derivatives have traditionally exhibited an extensive variety of bioactivities ranging from antimicrobial effects to anti-inflammatory to anti-angiogenic properties[1]. Isobenzofuranone natural products have also been shown to have useful bioactive properties[2]. An area currently in need of new bioactive lead compounds is the treatment of systemic fungal infections. Only a limited

selection of therapies exist for combating pathogenic fungal infections, often with severe side effects (host toxicity) and low efficacy (emerging drug resistance)[3]. Over one million people with compromised immune systems die each year from systemic fungal infections[4]. One of the most common human pathogens, *Candida albicans*, is responsible for a large percentage of these deaths. *C. albicans* is able to maintain a relatively benign yeast form under normal conditions, but becomes pathogenic by forming a biofilm within an infected host. Traditional antifungal therapies focus on the elimination of the pathogen itself, but counteracting this biofilm formation is another viable method for treating *C. albicans* infections.

The aim of this study was to evaluate a previously undiscovered Dothideomycete species from an iron-rich microbial mat community and search for antimicrobial secondary metabolites. During the investigation of this fungus, five structurally related secondary metabolites were found (Figure 72 (pg. 134))[5]. Three isobenzofuranones (compound **1**, compound **2a**, compound **2b**) and two isocoumarins (compound **3**, compound **4**) were isolated and structurally elucidated. Compound **1** ($C_{13}H_{16}O_5$ by HRESIMS) and compound **4** ($C_{13}H_{14}O_5$ by HRESIMS) have been previously reported in the literature[6, 7]. Comparison of NMR, optical rotation and circular dichroism (CD) data confirmed that the compounds were compound **1**and compound **4**. This is the first report of the discovery of natural products **2a**, **2b** and **3**. Compound **3** was named clearanol C while compounds **2a** and **2b** were named clearanol D and E, respectively. After evaluation of antimicrobial and anti-biofilm properties, the isocoumarins were found to prevent *C. albicans* biofilm growth through inhibition of hyphae formation[5].

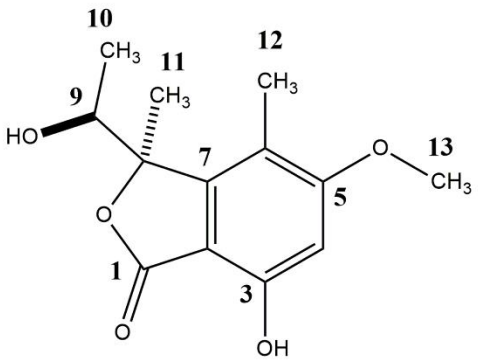

Compound 1

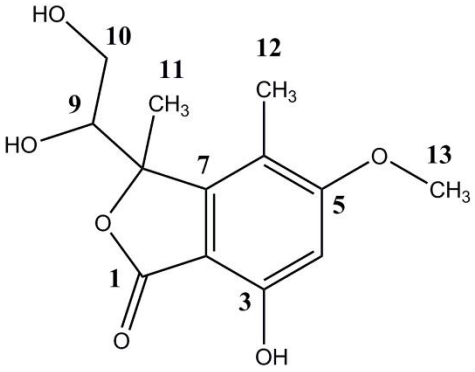

Compounds 2a and 2b
(clearanols D and E)

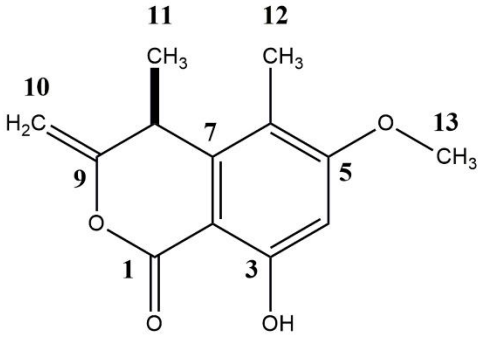

Compound 3
(clearanol C)

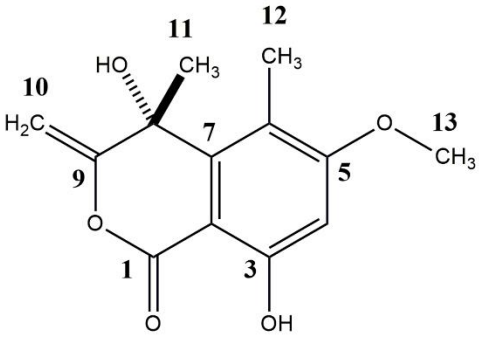

Compound 4

Figure 72. Structures of compounds 1-4.

Structural elucidation of clearanol C

Table 10. Summary of NMR data for clearanol C.

clearanol C					
position	δ_C	type	δ_H	(*J* in Hz)	HMBC
1	166.6	C			
2	99.5	C			
3	164.5	C			
4	98.5	CH	6.46	s	2,3,5,6
5	168.5	C			
6	115.5	C			
7	143.8	C			
8	36.0	CH	3.99	q (7.0)	2,6,7,11
9	159.1	C			
10	96.2	CH_2	4.74, 4.68	s,s	8,9
11	22.7	CH_3	1.34	d (7.0)	7,8,9
12	10.2	CH_3	2.09	s	5,6,7
13	56.6	CH_3	3.88	s	5

Compound **3** (clearanol C) ($C_{13}H_{14}O_4$ by HRESIMS, DBE = 7) is a newly discovered isocoumarin with strong similarity to the known compound **4**. The only difference between the planar structures is the absence of a hydroxyl group attached to C-8 (δ 36.0) in compound **3** that is present in compound **4** (C-8, δ 72.6). Evidence for this conclusion includes the absence of one oxygen atom in the chemical composition of **3** compared to **4**. Furthermore, all carbon chemical shift values are virtually identical between compounds **3** and **4** (average $\Delta\delta$ = 1.1), except C-8 and the methyl group attached to C-8 (C-11, compound **3**: δ 22.7, compound **4**: δ 29.6.) In addition, position C-8 in **3** is protonated (H-8, δ_H 3.99, J = 7.0) and split into a quartet by the methyl protons of C-11, which appear as a doublet (H-11, δ_H 1.34, J = 7.0). Complete data sets of 1D and 2D NMR spectra (^{1}H, ^{13}C, gCOSY, HSQC, gHMBC) were collected for

compound **3** to confirm the structure (Table 10 (pg. 135), Figure 73 - Figure 77 (pg. 137-141)). Carbon chemical shifts of C-2 (δ 99.5), C-3 (δ 164.4), C-4 (δ 98.5), C-5 (δ 168.4), C-6 (δ 115.5) and C-7 (δ 143.8) were consistent with a penta-substituted phenyl ring. Substituents to the ring were assigned based on chemical shifts, HSQC and gHMBC correlations. Firstly, a methyl group was assigned to position C-6 based on a chemical shift value of 115.5, typical for a methyl substitution, and HMBC correlations from the methyl protons (H-12, δ_H 2.09) to C-5, C-6, and C-7. A methoxy group was assigned to position C-5 (δ 168.4) based on an HMBC correlation from H-13 (δ_H 3.88) to C-5 and the chemical shift value of C-5, which is consistent with an oxygen substitution. The sole proton on the ring (H-4, δ_H 6.46) showed HMBC correlations to C-2, C-3, C-5, and C-6, and so was placed *para* to C-7. A hydroxyl group was assigned to position C-3 (δ 164.4) based on a chemical shift value consistent with oxygen connectivity. The quaternary carbon C-7 (δ 143.8) was placed next to C-8 based on an HMBC correlation from H-11 to C-7, C-8, and C-9, which consequently placed C-9 on the other side of C-8. The double bond between C-10 (δ 96.2) and C-9 (δ 159.1) was confirmed by chemical shift values consistent with a terminal methylene group and the HMBC correlations from H-10 (δ_H 4.68, δ_H 4.74) to C-8 and C-9. The lack of an HMBC correlation from H-10 to a third carbon and the high chemical shift of C-9 (δ 159.1) indicated that C-9 was located between C-8 and an oxygen atom. The chemical shift of C-1 (δ 166.6) was consistent with an ester functionality, which indicated the presence of a carbonyl on the opposite side of the oxygen atom; a fusion of this carbon to the quaternary carbon C-2 satisfied the double bond equivalent requirements calculated from the chemical formula.

Compound **3** contains one stereocenter at the C-8 position. To determine absolute configuration, optical rotation and CD data were collected and compared to a similar isocoumarin with an identical stereocenter: (*S*)-(+)-ascochin[8]. Compound **3** showed a positive optical rotation, a negative Cotton effect at 210 nm and a positive Cotton effect at 233 nm, consistent with the experimental CD spectra of (*S*)-ascochin. Therefore, the absolute configuration of the C-8 stereocenter was determined to be *S*.

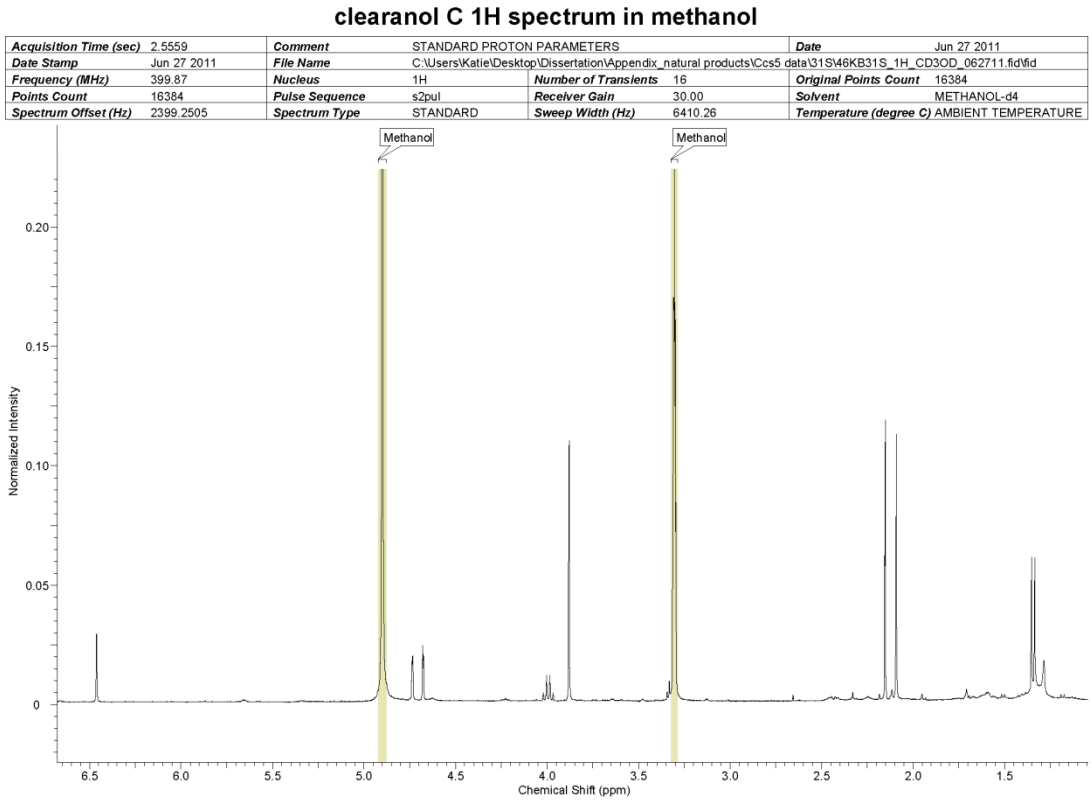

Figure 73. ^{1}H NMR spectrum (400 MHz, methanol-d4) of clearanol C.

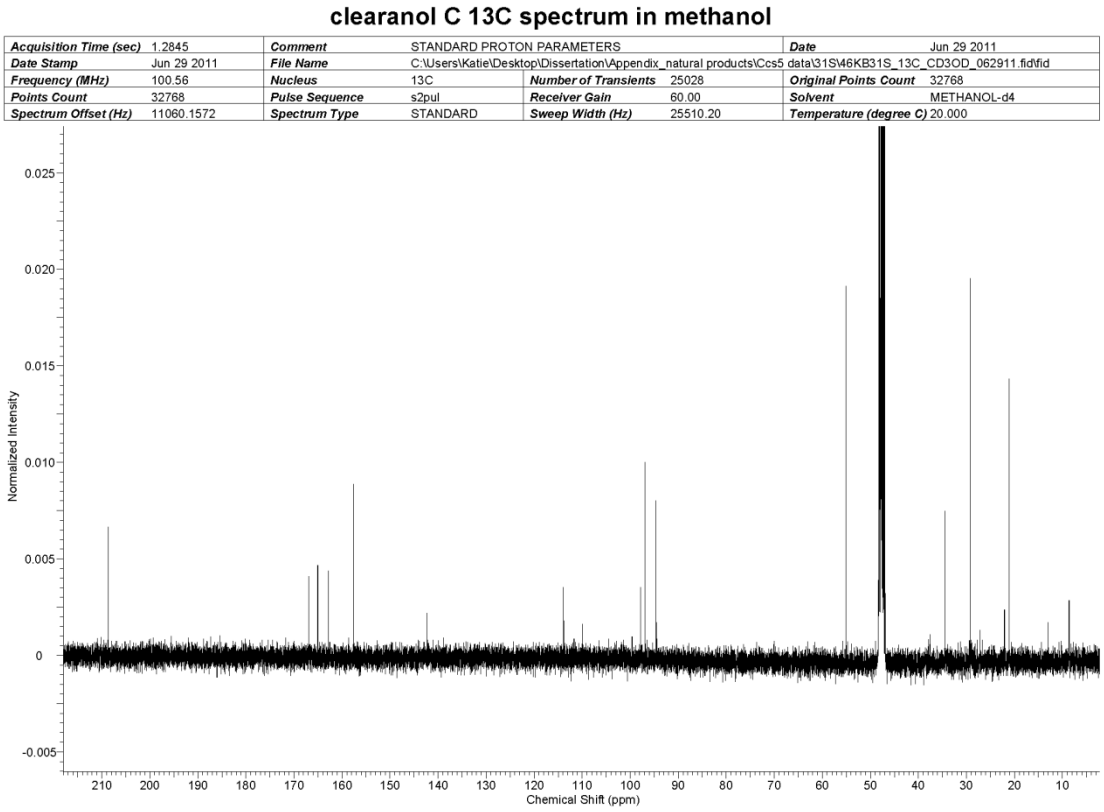

Figure 74. ^{13}C NMR spectrum (100 MHz, methanol-d4) of clearanol C.

Clearanol C gCOSY in methanol

Acquisition Time (sec)	(0.1500, 0.0512)	***Comment***	STANDARD PROTON PARAMETERS
Date	28 Jun 2011 08:09:56	***Date Stamp***	Jun 27 2011
File Name	C:\Users\Katie\Desktop\Dissertation\Appendix_natural products\Ccs5 data\31S\46KB31S_gCOSY_CD3OD_062711.fid\fid		
Frequency (MHz)	(399.87, 399.87)	***Nucleus***	(1H, 1H)
Number of Transients	56	***Original Points Count***	(375, 128)
Points Count	(512, 512)	***Pulse Sequence***	gCOSY
Solvent	cd3od	***Spectrum Type***	COSY
Sweep Width (Hz)	(2495.12, 2495.12)		

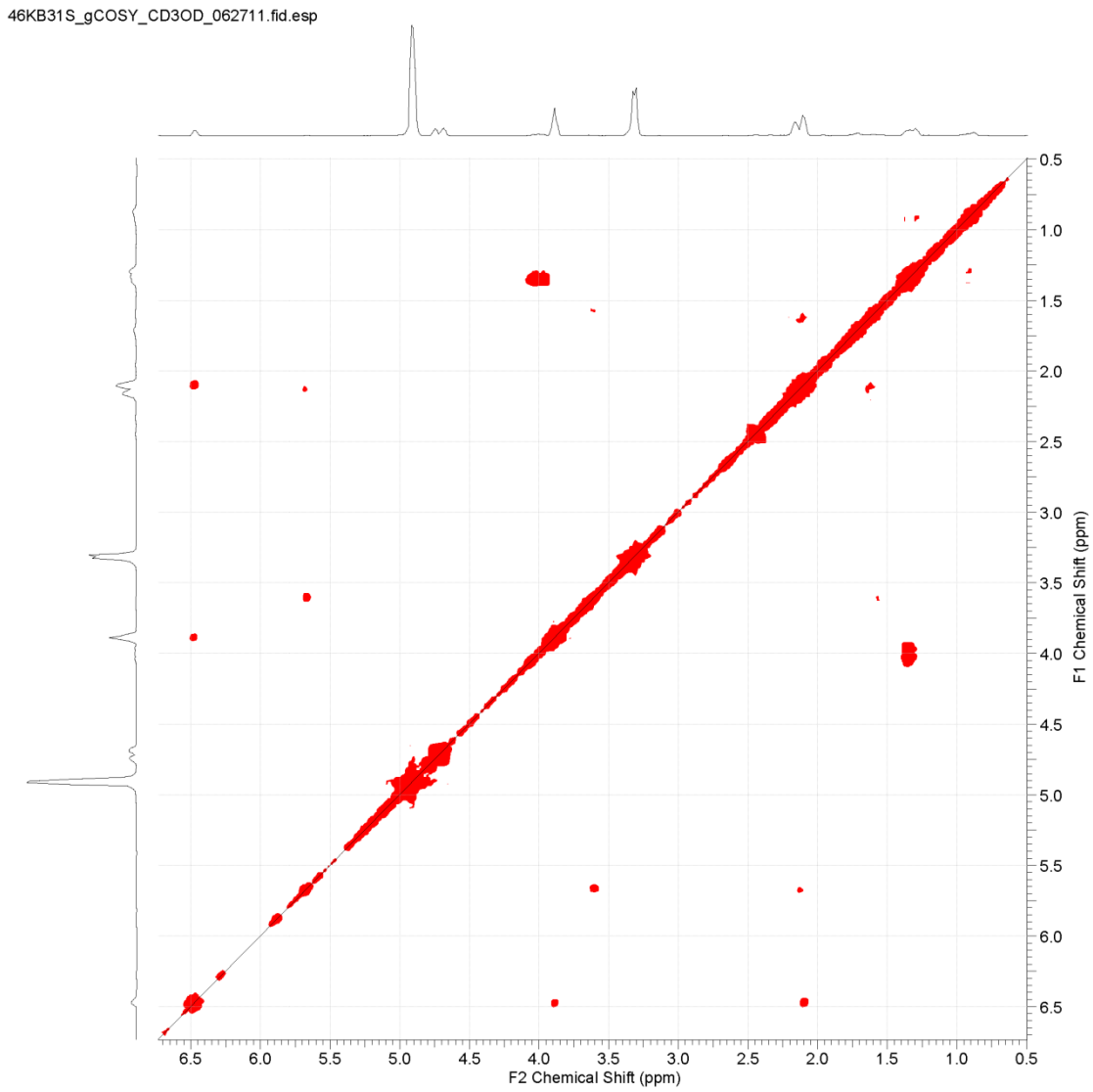

Figure 75. gCOSY NMR spectrum (400 MHz, methanol-d4) of clearanol C.

Clearanol C HSQC in methanol

Acquisition Time (sec)	(0.1500, 0.0075)	***Comment***	STANDARD PROTON PARAMETERS
Date	28 Jun 2011 08:09:42	***Date Stamp***	Jun 27 2011
File Name	C:\Users\Katie\Desktop\Dissertation\Appendix_natural products\Ccs5 data\31S\46KB31S_HSQC_CD3OD_062711.fid\fid		
Frequency (MHz)	(399.87, 100.55)	***Nucleus***	(1H, 13C)
Number of Transients	44	***Original Points Count***	(375, 128)
Points Count	(512, 1024)	***Pulse Sequence***	HSQC
Solvent	cd3od	***Spectrum Type***	HSQC
Sweep Width (Hz)	(2495.12, 17077.32)		

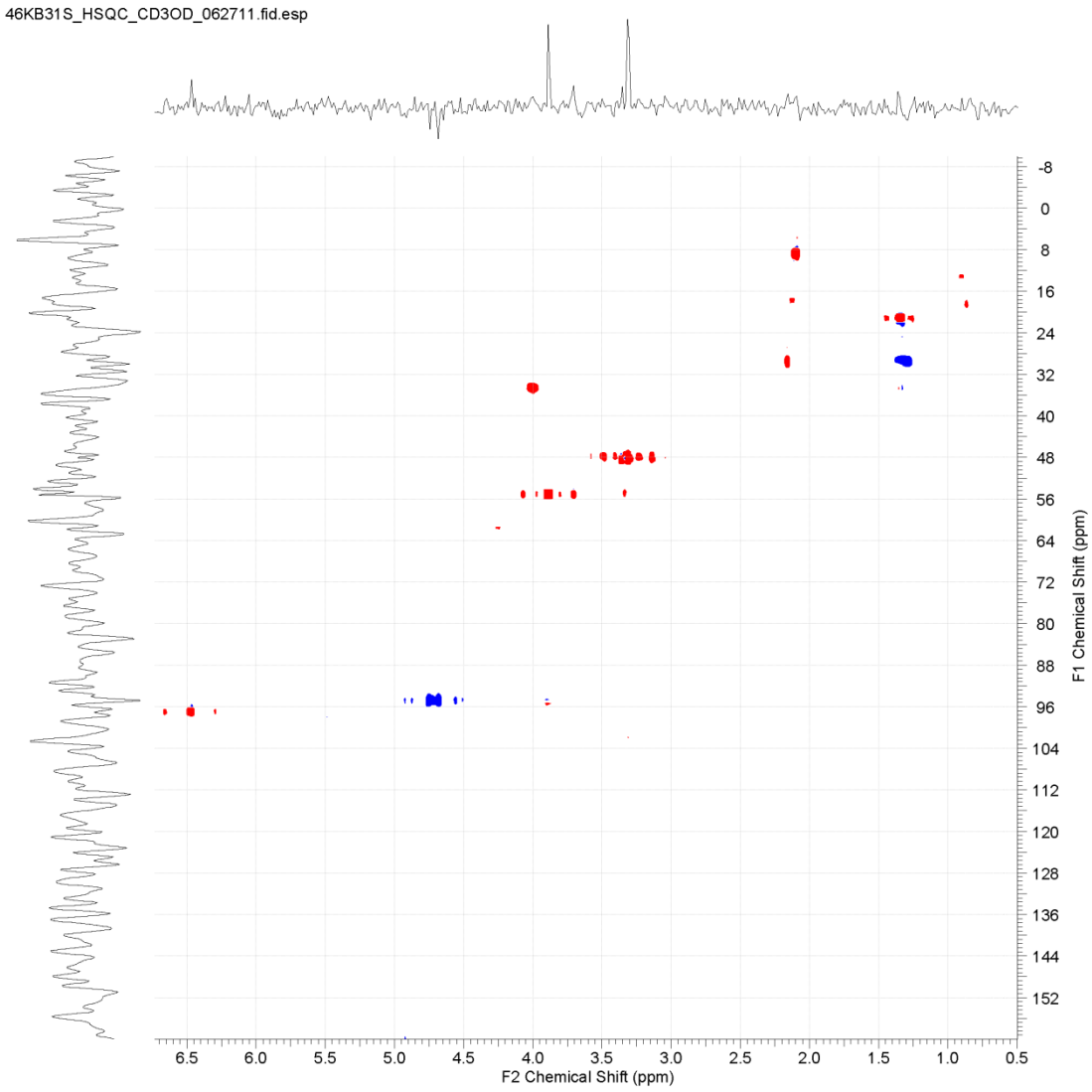

Figure 76. HSQC NMR spectrum (400, 100 MHz, methanol-d4) of clearanol C.

Clearanol C gHMBC in methanol

Acquisition Time (sec)	(0.1500, 0.0083)	***Comment***	STANDARD PROTON PARAMETERS
Date	28 Jun 2011 08:09:26	***Date Stamp***	Jun 27 2011
File Name	C:\Users\Katie\Desktop\Dissertation\Appendix_natural products\Ccs5 data\31S\46KB31S_gHMBC_CD3OD_062711.fid\fid		
Frequency (MHz)	(399.87, 100.55)	***Nucleus***	(1H, 13C)
Number of Transients	48	***Original Points Count***	(375, 200)
Points Count	(512, 2048)	***Pulse Sequence***	gHMBC
Solvent	cd3od	***Spectrum Type***	HMBC
Sweep Width (Hz)	(2495.12, 24120.95)		

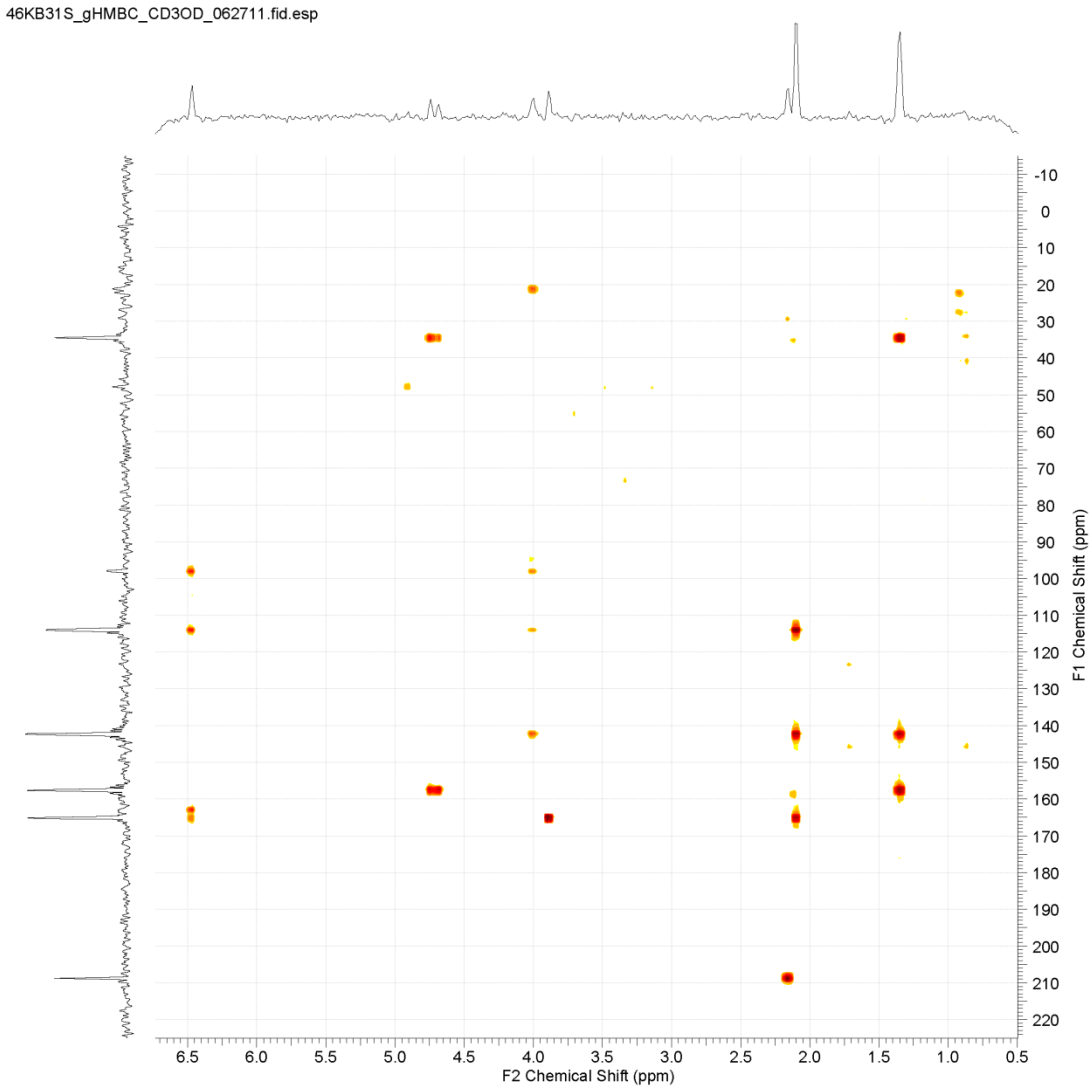

Figure 77. gHMBC NMR spectrum (400, 100 MHz, methanol-d4) of clearanol C.

Structural elucidation of clearanols D and E

Table 11. Summary of NMR data for clearanols D and E.

clearanols D and E									
position	**δ_C**	**type**	**δ_H**	**(*J* in Hz)**	**δ_C**	**type**	**δ_H**	**(*J* in Hz)**	**HMBC**
1	171.9	C			171.5	C			
2	105.4	C			104.6	C			
3	157.8	C			158.3	C			
4	99.5	CH	6.47	s	99.9	CH	6.49	s	1,2,3,5, 6,12
5	166.4	C			166.6	C			
6	113.4	C			113.3	C			
7	153.1	C			152.4	C			
8	90.6	C			90.4	C			
9	75.7	CH	4.13	dd (8.0, 3.7)	76.2	CH	4.11	dd (8.2, 2.7)	10
10	63.9	CH_2	3.83, 3.53	dd (11.3, 3.5), dd (11.3, 8.2)	63.3	CH_2	3.34, 3.14	dd (11.3, 8.6), dd (11.3, 2.7)	8,9
11	22.08	CH_3	1.67	s	22.11	CH_3	1.73	s	7,8,9
12	11.4	CH_3	2.18	s	11.7	CH_3	2.15	s	5,6,7
13	56.9	CH_3	3.87	s	56.9	CH_3	3.88	s	5

Compound **2** (clearanols D and E) ($C_{13}H_{16}O_6$ by HRESIMS, DBE = 6) is a diastereomeric mixture of new isobenzofuranones that are structurally related to the known compound **1**. The major difference between the planar structures is the addition of a hydroxyl group at the C-10 position in compound **2**. In **1**, C-10 (δ 17.4) is a methyl group, while in **2a** (C-10, δ 63.9) and **2b** (C-10, δ 63.3), it is a methylene with a terminal hydroxyl group. All other carbon chemical shift values are identical between compound **1** and compound **2** (average $\Delta\delta = 0.7$). Data sets of 1D and 2D NMR were collected on **1** and **2** (Table 11, Figure 78 - Figure 82 (pg. 144-148)) for full structure elucidation. In addition, variable temperature ^{1}H and 1D NOESY experiments were performed on the compound **2** mixture to determine the separate chemical identities of **2a** and **2b**.

Because the compound **2** mixture was inseparable by semi-preparative HPLC, the ^{1}H and ^{13}C NMR data were "doubled" (Figure 78 - Figure 79 (pg. 44-45)). These data could be interpreted in two ways: compound **2** contained one molecule in a tautomeric "flux" at room temperature, or it contained two different diastereomeric molecules. In order to determine which explanation was correct, variable temperature ^{1}H experiments were performed (4 °C, 20 °C, 50 °C), with the rationale that increasing temperatures would rapidly interconvert any tautomeric forms of the same molecule and the doubled peaks would merge. Instead, a marked separation of ^{1}H peaks between 3.0 and 4.0 ppm was observed at 50 °C (Figure 83 (pg. 149)). This evidence indicated that compound **2** was actually a mixture of diastereomers. The ^{1}H and ^{13}C chemical shifts were distinct enough to be accurately separated into two discrete molecules with identical planar structures: clearanol D (**2a**) and clearanol E (**2b**).

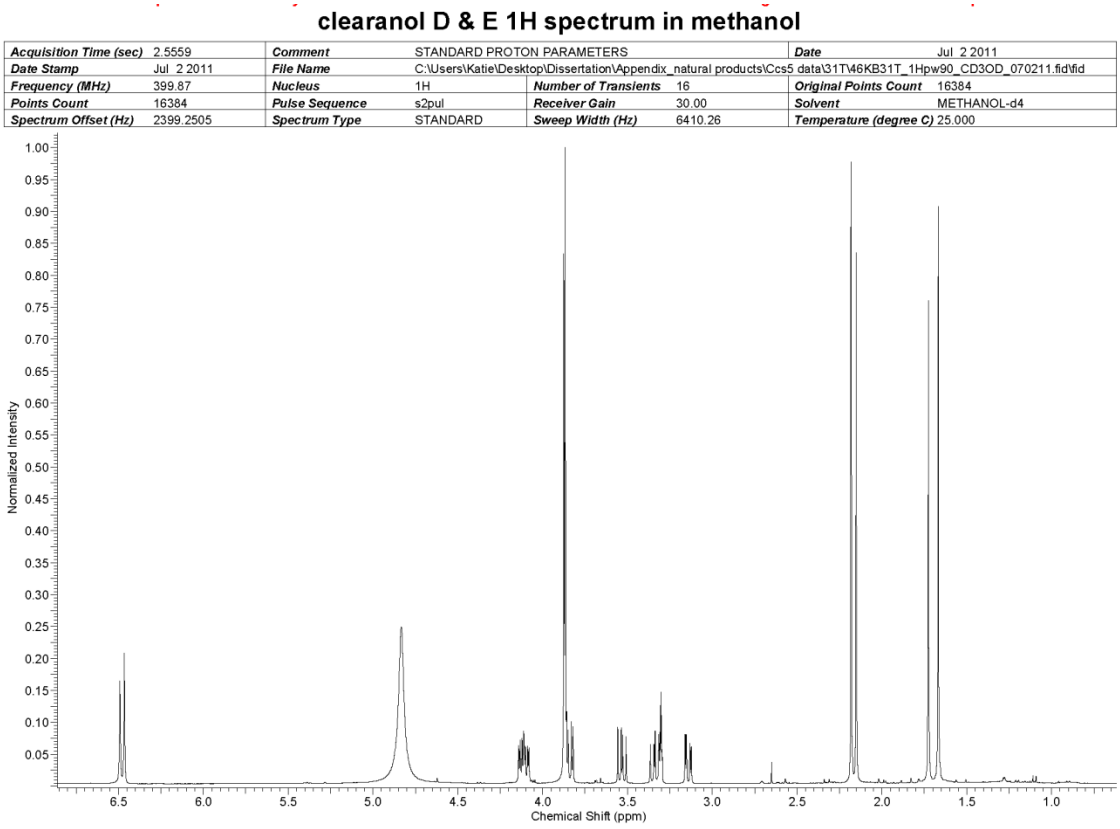

Figure 78. ^{1}H NMR spectrum (400 MHz, methanol-d4) of clearanol D/E.

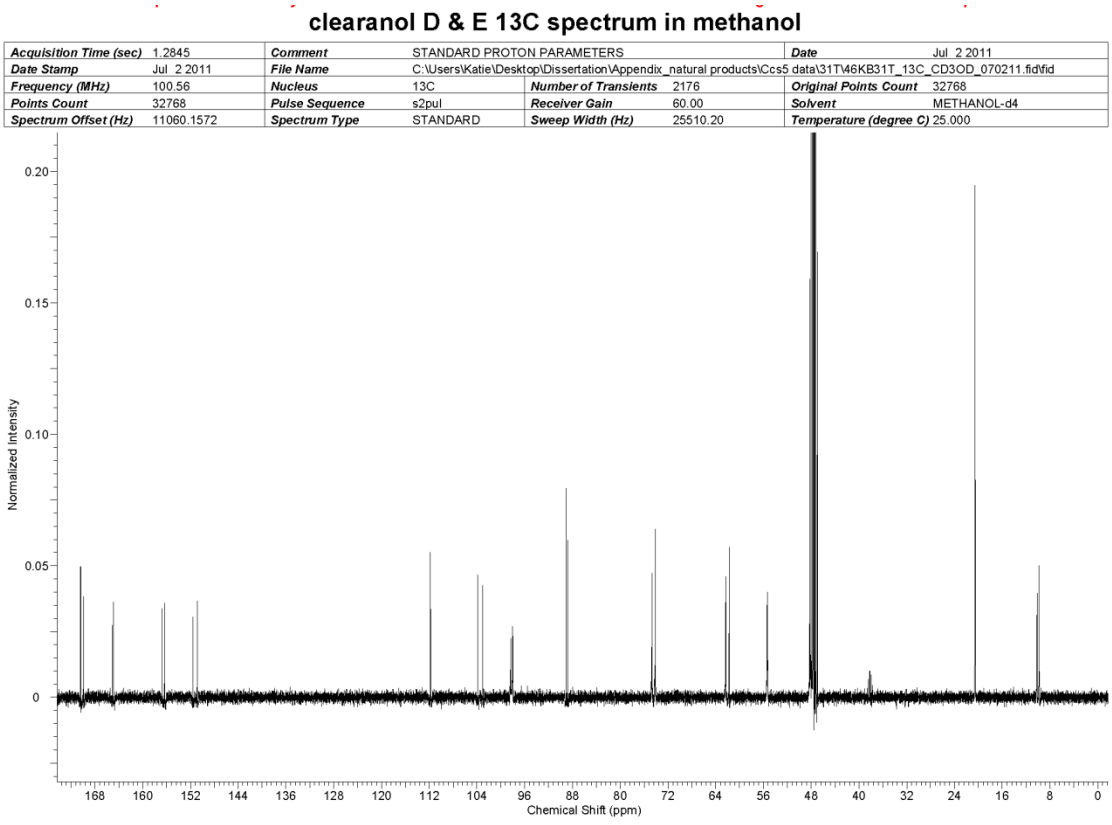

Figure 79. ^{13}C NMR spectrum (100 MHz, methanol-d4) of clearanol D/E.

Clearanol D & E gCOSY in methanol

Acquisition Time (sec)	(0.1500, 0.0520)	***Comment***	STANDARD PROTON PARAMETERS
Date	02 Jul 2011 12:47:52	***Date Stamp***	Jul 2 2011
File Name	C:\Users\Katie\Desktop\Dissertation\Appendix_natural products\Ccs5 data\31T\46KB31T_gCOSY_CD3OD_070211.fid\fid		
Frequency (MHz)	(399.87, 399.87)	***Nucleus***	(1H, 1H)
Number of Transients	1	***Original Points Count***	(369, 128)
Points Count	(512, 512)	***Pulse Sequence***	gCOSY
Solvent	cd3od	***Spectrum Type***	COSY
Sweep Width (Hz)	(2455.82, 2455.82)		

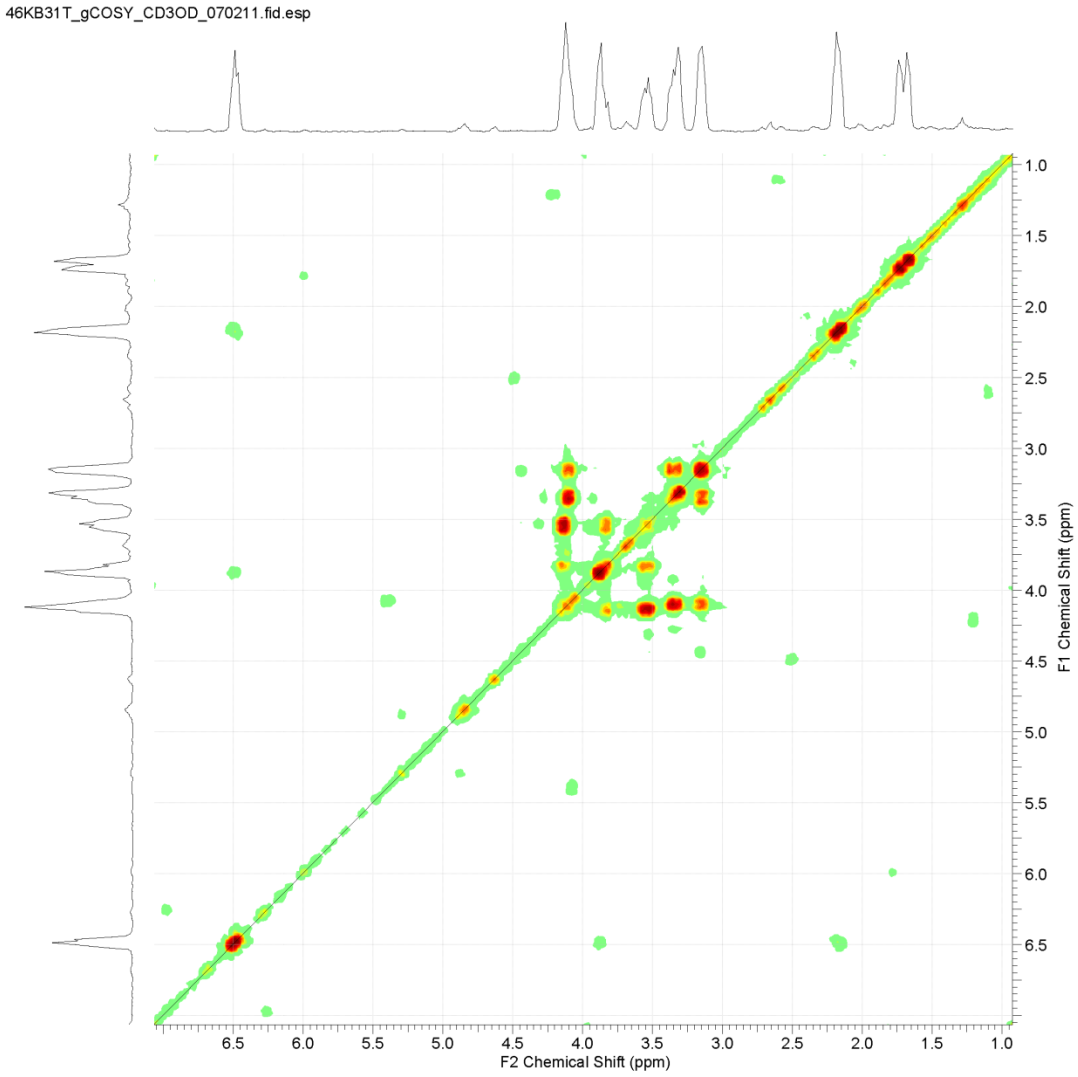

Figure 80. gCOSY NMR spectrum (400 MHz, methanol-d4) of clearanol D/E.

Clearanol D & E HSQC in methanol

Acquisition Time (sec)	(0.1500, 0.0073)	***Comment***	STANDARD PROTON PARAMETERS
Date	02 Jul 2011 14:36:52	***Date Stamp***	Jul 2 2011
File Name	C:\Users\Katie\Desktop\Dissertation\Appendix_natural products\Ccs5 data\31T\46KB31T_HSQC_CD3OD_070211.fid\fid		
Frequency (MHz)	(399.87, 100.55)	***Nucleus***	(1H, 13C)
Number of Transients	56	***Original Points Count***	(369, 128)
Points Count	(512, 1024)	***Pulse Sequence***	HSQC
Solvent	cd3od	***Spectrum Type***	HSQC
Sweep Width (Hz)	(2455.82, 17576.84)		

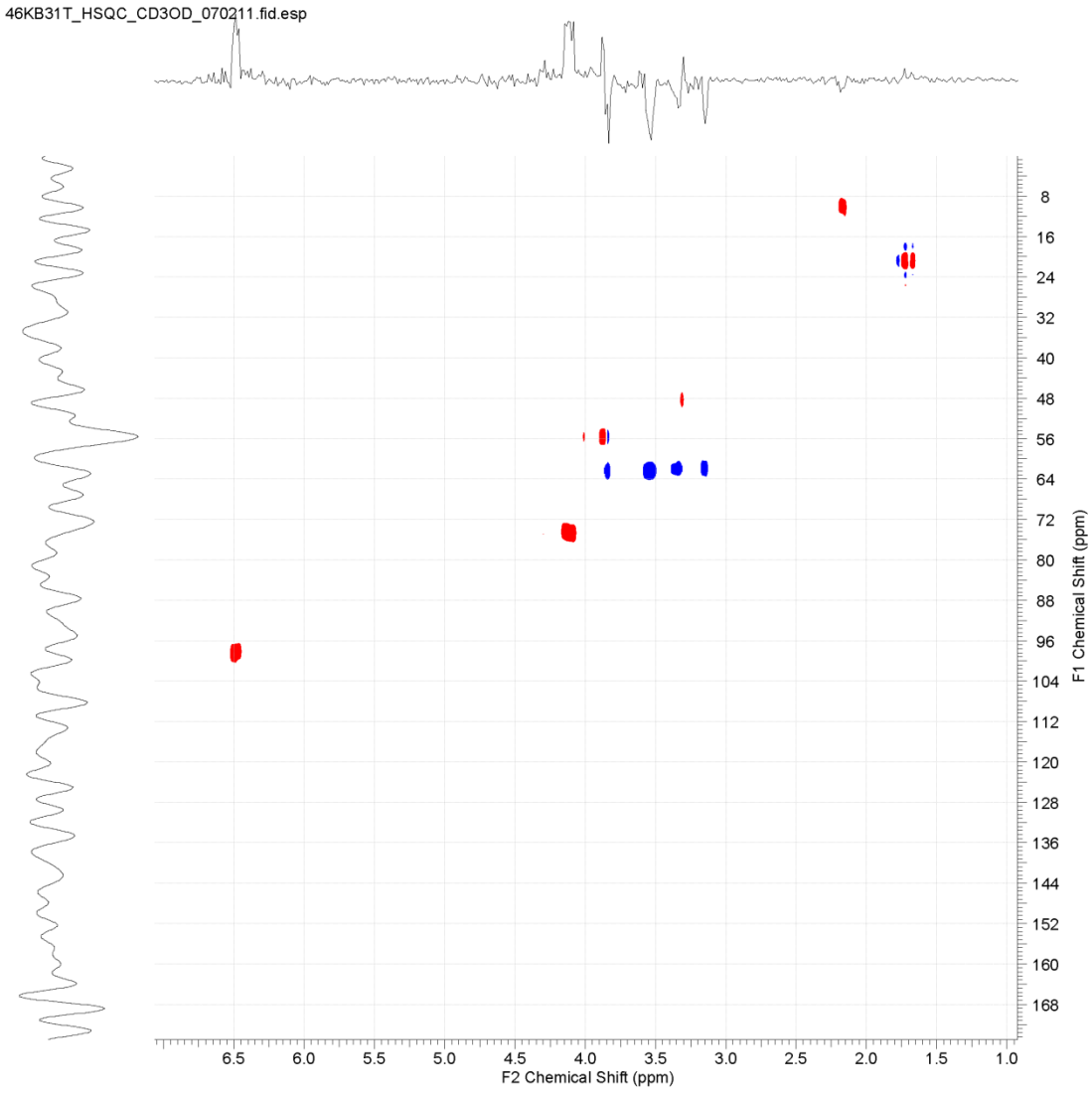

Figure 81. HSQC NMR spectrum (400, 100 MHz, methanol-d4) of clearanol D/E.

Clearanol D & E gHMBC in methanol

Acquisition Time (sec)	(0.1500, 0.0083)	***Comment***	STANDARD PROTON PARAMETERS
Date	02 Jul 2011 18:08:04	***Date Stamp***	Jul 2 2011
File Name	C:\Users\Katie\Desktop\Dissertation\Appendix_natural products\Ccs5 data\31T\46KB31T_gHMBC_CD3OD_070211.fid\fid		
Frequency (MHz)	(399.87, 100.55)	***Nucleus***	(1H, 13C)
Number of Transients	32	***Original Points Count***	(369, 200)
Points Count	(512, 2048)	***Pulse Sequence***	gHMBC
Solvent	cd3od	***Spectrum Type***	HMBC
Sweep Width (Hz)	(2455.82, 24120.95)		

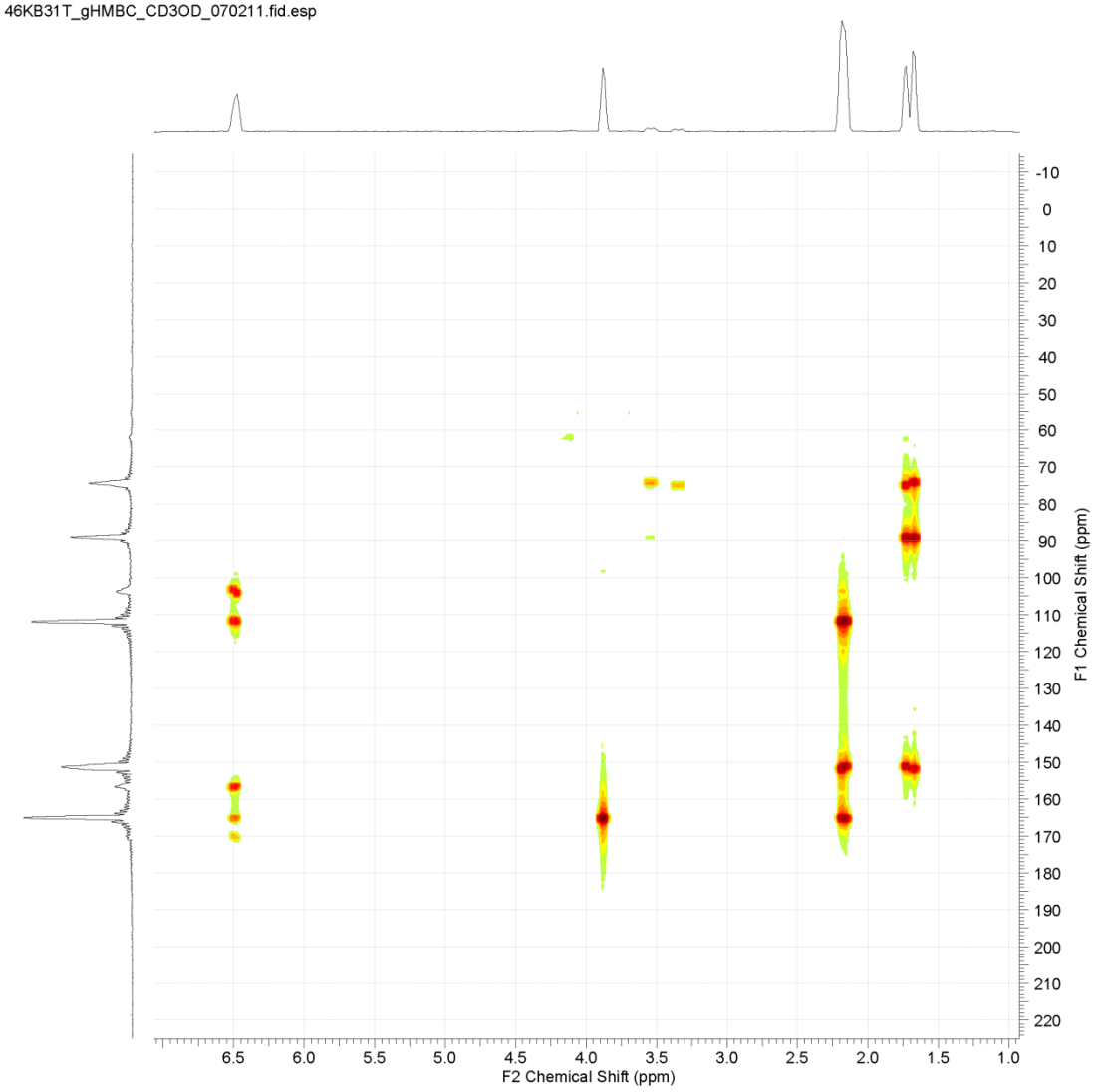

Figure 82. gHMBC NMR spectrum (400, 100 MHz, methanol-d4) clearanol D/E.

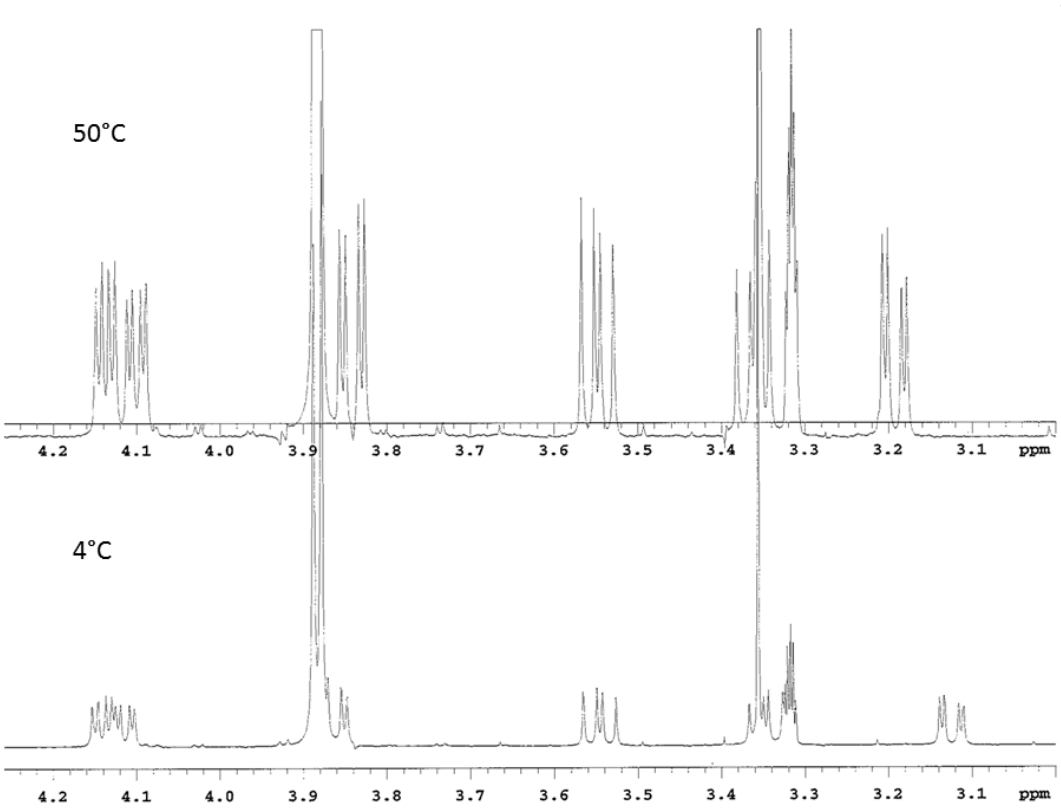

Figure 83. ^{1}H NMR variable temperature experiments for clearanol D/E.

After structural elucidation, Compounds **1-4** were subjected to antibacterial, antifungal and anti-biofilm formation assays. Compounds **1**, **2** and **4** exhibited no antibiotic properties. However, compound **3** showed mild antifungal effects when tested against *Candida albicans* (ATCC 38245) and *Aspergillus fumigatus* (FGSC A1100) at 100 μg/mL by reducing growth 61% and 62%, respectively[5]. The effects of compounds **1-4** on *C. albicans* growth and biofilm formation were evaluated in 96-well polystyrene microplates. *C. albicans* DAY185 cells were treated with various concentrations (6.25–200 μM) of test compounds or DMSO as negative control at 37 ºC for 48 h. Compound 3 and Compound 4 showed moderate biofilm inhibition activity with MIC values of 101 ±3 and 86 ± 3 μM, respectively[5].

Experimental Section

General Experimental Procedures

Optical rotation measurements were taken on a Rudolph Research Analytical Autopol® III polarimeter at 22 °C (solvent: methanol, cell length: 0.5 dm). CD measurements were taken on an AVIV Instruments, Inc. Circular Dichroism Spectrometer, model 202-01 (solvent: methanol with trace amounts of acetonitrile). IR spectra were collected in solution (methanol) between two NaCl plates on a Bio-Rad FT-155 FTIR spectrometer. NMR data were obtained on Varian VNMR spectrometers (300, 400 and 500 MHz for ^{1}H and 75, 100 and 125 MHz for ^{13}C) with 4-nuclei autoswitchable PFG, broad band and triple resonance probes at 20-25 °C. NMR spectra were processed with ACD Labs software. HRESIMS data were obtained by electrospray ionization employing an Agilent 6538 UHD Accurate-Mass Quadrupole TOF mass analyzer. LCMS data were collected on a Finnigan LCQ-Deca equipped

with a Surveyor PDA Plus Detector, autosampler and MS pump. LC conditions consisted of methanol-water (0.1% formic acid) gradients on a 3μm Luna C_{18} column. HPLC separations were performed on preparative and semi-preparative Shimadzu systems equipped with 5μm Gemini or Luna C_{18} columns (250 x 21.20 mm at 10 mL/min flow rate for preparative HPLC and 250 x 10.00 mm at 2 mL/min flow rate for semi-preparative HPLC.)

Fungal Materials

Fungal samples were collected from a microbial mat formed near the intersection of a spring (39° 45' 15.0" North, 105° 13' 39.9" West) and Clear Creek River in north central Colorado. Sequencing of the internal transcribed spacer (ITS) region (Scheme 1) of the organism revealed 98% identity to Uncultured Dothideomycete isolate s_C03_05.ab1. Scale-up fungal cultures were grown statically on ~24 g of Cheerios® cereal in 1L flasks for one month. Twenty-two flasks were prepared by adding ~200 mL (~24 g) of cereal and autoclaving. Then, 120 mL of sterile 3 g/L sucrose water was added along with a slice of fungal material from an agar plate.

Scheme 1. ITS sequence of undescribed Dothideomycete.

NGGCATCCTCCNGATCCGAGGGTCAAAGTGTTAAATAGACTTGGATGGTTG
CAAGCTAATTATTAGCTAGAGTCGCAAATTGTGCTGCGCTTCTATACCAATA
CACTGGCTGCCAATTTCTTTAAGGCGAGTCCAAACGCAAGGGAGAGGACAA
ACACCCAACACCAAGCATAGCTTGAGGGTACAAATGACGCTCGAACAGGCA
TGCCCCATGGAATACCAAGGGGCGCAATGTGCGTTCAAAGATTCGATGATT
CACTGAATTCTGCAATTCACACTACTTATCGCATTTCGCTGCGTTCTTCATCG
ATGCCAGAACCAAGAGATCCGTTGTTGAAAGTTGTAATTATTATAGTTATTC
AGACGCTGATTGAAAATTAAAAAGGTTTTAGAATTGTCCATTCGGCAGGCA
AGCCCACCGAGGAAACATGAGTACGCAAAAGACAAGGGTGCAGACAGGGG
GCTTACTCGTGATCCAGTAATCAAACTGGGACTTTCCACCCCCCCGATCAGT
AGAAATCTACTGTATTTAATGATCCTTCCGCAGGTTCCCCNTACGGAAGANN
NNNNNNN

Extraction and Isolation

Fungal cultures were extracted using 250 mL ethyl acetate per flask three times at room temperature. Crude extract (2.8 g) was subjected to gel-filtration chromatography (Sephadex® LH-20) in 1:1 MeOH:DCM, which afforded 10 fractions. Fractions 6 and 7 were combined and subjected to preparative HPLC (water, 40-100% MeOH gradient). These fractions were further purified using semi-preparative HPLC to yield compound **1** (water, 43% MeCN; 19.5 mg), compounds **2a** and **2b** (water, 32% MeCN; 39.2 mg), compound **3** (water, 63% MeCN; 3.1 mg), and compound **4** (water, 55% MeCN; 5.0 mg).

Compound 1: amorphous solid; $[\alpha]^{22}_{D}$ -33 (*c* 1.3, MeOH); UV (MeOH) λ_{max} (log ε) 218 (4.40), 260 (4.04), 300 (3.75) nm; ^{1}H NMR (400 MHz, METHANOL-d_4) δ = 6.48 (1H, s, H-4), 4.22 (1H, q, *J* = 6.3 Hz, H-9), 3.87 (3H, s, H-13), 2.12 (3H, s, H-12), 1.73 (3H, s, H-11), 0.86 (3H, d, *J* = 6.3 Hz, H-10); ^{13}C NMR (101 MHz, METHANOL-d_4) δ = 172.1 (C, C-1), 166.6 (C, C-5), 158.5 (C, C-3), 153.0 (C, C-7), 112.8 (C, C-6), 105.0 (C, C-2), 99.9 (CH, C-4), 91.6 (C, C-8), 71.3 (CH, C-9), 56.9 (CH_3, C-13), 21.7 (CH_3, C-11), 17.4 (CH_3, C-10), 11.6 (CH_3, C-12); HRESIMS *m/z* 275.0896 $[M+Na]^+$, (calcd for $C_{13}H_{16}O_5Na$, 275.0896).

Compound 2a (clearanol D): amorphous solid (1:1 mixture with clearanol E); $[\alpha]^{22}_{D}$ -15 (*c* 2.1, MeOH); UV (MeOH) λ_{max} (log ε) 218 (4.22), 260 (3.87), 300 (3.59) nm; IR (NaCl) ν_{max} 3596, 3089, 1737, 1651, 1472, 1373, 1319, 1247, 1220, 1153, 1067 cm^{-1}; ^{1}H NMR (400 MHz, METHANOL-d_4) δ = 6.47 (1H, s, H-4), 4.13 (1H, dd, *J* = 8.0 Hz, *J* = 3.7 Hz, H-9), 3.87 (3H, s, H-13), 3.83 (1H, dd, *J* = 11.3 Hz, *J* = 3.5 Hz, H-10a), 3.53 (1H, dd, *J* = 11.3 Hz, *J* = 8.2 Hz, H-10b), 2.18 (3H, s, H-12), 1.67 (3H, s, H-11); ^{13}C

NMR (101 MHz, METHANOL-d_4) δ = 171.9 (C, C-1), 166.4 (C, C-5), 157.8 (C, C-3), 153.1 (C, C-7), 113.4 (C, C-6), 105.4 (C, C-2), 99.5 (CH, C-4), 90.6 (C, C-8), 75.7 (CH, C-9), 63.9 (CH_2, C-10), 56.9 (CH_3, C-13), 22.08 (CH_3, C-11), 11.4 (CH_3, C-12); HRESIMS *m/z* 291.0839 $[M+Na]^+$, (calcd for $C_{13}H_{16}O_6Na$, 291.0845).

Compound 2b (clearanol E): amorphous solid (1:1 mixture with clearanol D); $[\alpha]^{22}_D$ -15 (*c* 2.1, MeOH); UV (MeOH) λ_{max} (log ε) 218 (4.22), 260 (3.87), 300 (3.59) nm; IR (NaCl) ν_{max} 3596, 3089, 1737, 1651, 1472, 1373, 1319, 1247, 1220, 1153, 1067 cm^{-1}; ^1H NMR (400 MHz, METHANOL-d_4) δ = 6.49 (1H, s, H-4), 4.11 (1H, dd, *J* = 8.2 Hz, *J* = 2.7 Hz, H-9), 3.88 (3H, s, H-13), 3.34 (1H, dd, *J* = 11.3 Hz, *J* = 8.6 Hz, H-10a), 3.14 (1H, dd, *J* = 11.3 Hz, *J* = 2.7 Hz, H-10b), 2.15 (3H, s, H-12), 1.73 (3H, s, H-11); ^{13}C NMR (101 MHz, METHANOL-d_4) δ = 171.5 (C, C-1), 166.6 (C, C-5), 158.3 (C, C-3), 152.4 (C, C-7), 113.3 (C, C-6), 104.6 (C, C-2), 99.9 (CH, C-4), 90.4 (C, C-8), 76.2 (CH, C-9), 63.3 (CH_2, C-10), 56.9 (CH_3, C-13), 22.11 (CH_3, C-11), 11.7 (CH_3, C-12); HRESIMS *m/z* 291.0839 $[M+Na]^+$, (calcd for $C_{13}H_{16}O_6Na$, 291.0845).

Compound 3 (clearanol C): amorphous solid; $[\alpha]^{22}_D$ +39 (*c* 0.06, MeOH); UV (MeOH) λ_{max} (log ε) 220 (3.83) 270 (3.47), 312 (3.20) nm; IR (NaCl) ν_{max} 3623, 2949, 2581, 1651, 1018 cm^{-1}; ^1H NMR (400 MHz, METHANOL-d_4) δ = 6.46 (1H, s, H-4), 4.74 (1H, s, H-10a), 4.68 (1H, s, H-10b), 3.99 (1H, q, *J* = 7.0 Hz, H-8), 3.88 (3H, s, H-13), 2.09 (3H, s, H-12), 1.34 (3H, d, *J* = 7.0 Hz, H-11); ^{13}C NMR (101 MHz, METHANOL-d_4) δ = 168.4 (C, C-5), 166.6 (C, C-1), 164.4 (C, C-3), 159.1 (C, C-9), 143.8 (C, C-7), 115.5 (C, C-6), 99.5 (C, C-2), 98.5 (CH, C-4), 96.2 (CH_2, C-10), 56.6 (CH_3, C-13), 36.0 (CH, C-8), 22.7 (CH_3, C-11), 10.2 (CH_3, C-12); HRESIMS *m/z* 233.0815 $[M-H]^-$, (calcd for $C_{13}H_{13}O_4$, 233.0814).

Compound 4: amorphous solid; UV (MeOH) λ_{max} (log ε) 220 (4.15) 270 (3.83), 314 (3.64) nm; ^{1}H NMR (300 MHz, METHANOL-d_4) δ = 6.51 (1H, s, H-4), 5.07 (1H, s, H-10a), 4.87 (1H, s, H-10b), 3.88 (3H, s, H-13), 2.38 (3H, s, H-12), 1.64 (3H, s, H-11); ^{13}C NMR (75 MHz, METHANOL-d_4) δ = 168.2 (C, C-5), 167.4(C, C-1), 164.6 (C, C-3), 163.0 (C, C-9), 144.9 (C, C-7), 117.9 (C, C-6), 99.2 (C, C-2), 99.2 (CH, C-4), 95.6 (CH_2, C-10), 56.7 (CH_3, C-13), 72.6 (C, C-8), 29.6 (CH_3, C-11), 12.4 (CH_3, C-12); HRESIMS *m/z* 249.0766 $[M-H]^-$, (calcd for $C_{13}H_{13}O_5$, 249.0763).

References

[1] Pal, S., Chatare, V., and Pal, M. (2011) Isocoumarin and its derivatives: An overview on their synthesis and applications, *Curr Org Chem 15*, 782-800.

[2] Huang, X.-Z., , Y. Z., , X.-L. G., , K. T., , J.-M. G., , H.-B. W., and Fu, a. G.-M. (2012) A novel antioxidant isobenzofuranone derivative from fungus *Cephalosporium* sp. AL031, *Molecules 17*, 4219-4224.

[3] Xie, J. L., Polvi, E. J., Shekhar-Guturja, T., and Cowen, L. E. (2014) Elucidating drug resistance in human fungal pathogens, *Future Microbiol 9*, 523-542.

[4] Brown, G. D., Denning, D. W., Gow, N. A. R., Levitz, S. M., Netea, M. G., and White, T. C. (2012) Hidden killers: Human fungal infections, *Sci Transl Med. 4*, 165rv113.

[5] Gerea, A. L., Branscum, K. M., King, J. B., You, J., Powell, D. R., Miller, A. N., Spear, J. R., and Cichewicz, R. H. (2012) Secondary metabolites produced by fungi derived from a microbial mat encountered in an iron-rich natural spring, *Tetrahedron Lett. 53*, 4202-4205.

[6] Tayone, W. C., Honma, M., Kanamaru, S., Noguchi, S., Tanaka, K., Nehira, T., and Hashimoto, M. (2011) Stereochemical investigations of isochromenones and isobenzofuranones isolated from *Leptosphaeria* sp. KTC 727, *J. Nat. Prod. 74*, 425-429.

[7] Chinworrungsee, M., Kittakoop, P., Isaka, M., Chanphen, R., Tanticharoen, M., and Thebtaranonth, Y. (2002) Halorosellins A and B, unique isocoumarin glucosides from the marine fungus *Halorosellinia oceanica*, *J. Chem. Soc., Perkin Trans. 1*, 2473-2476.

[8] Krohn, K., Kock, I., Elsässer, B., Flörke, U., Schulz, B., Draeger, S., Pescitelli, G., Antus, S., and Kurtán, T. (2007) Bioactive natural products from the endophytic fungus *Ascochyta* sp. from *Meliotus dentatus* – Configurational assignment by solid-state CD and TDDFT calculations, *Eur. J. Org. Chem. 2007*, 1123-1129.